



### 저작자표시-비영리-동일조건변경허락 2.0 대한민국

이용자는 아래의 조건을 따르는 경우에 한하여 자유롭게

- 이 저작물을 복제, 배포, 전송, 전시, 공연 및 방송할 수 있습니다.
- 이차적 저작물을 작성할 수 있습니다.

다음과 같은 조건을 따라야 합니다:



저작자표시. 귀하는 원저작자를 표시하여야 합니다.



비영리. 귀하는 이 저작물을 영리 목적으로 이용할 수 없습니다.



동일조건변경허락. 귀하가 이 저작물을 개작, 변형 또는 가공했을 경우에는, 이 저작물과 동일한 이용허락조건하에서만 배포할 수 있습니다.

- 귀하는, 이 저작물의 재이용이나 배포의 경우, 이 저작물에 적용된 이용허락조건을 명확하게 나타내어야 합니다.
- 저작권자로부터 별도의 허가를 받으면 이러한 조건들은 적용되지 않습니다.

저작권법에 따른 이용자의 권리는 위의 내용에 의하여 영향을 받지 않습니다.

이것은 [이용허락규약\(Legal Code\)](#)을 이해하기 쉽게 요약한 것입니다.

[Disclaimer](#)

공학박사학위논문

가스센서 및 리튬이차전지용 산화주석  
및 실리콘 나노구조의 제조와 특성 평가

**Fabrication and Characterization  
of Tin Oxide and Silicon Based Nanostructures  
for Gas Sensor and Li-ion Battery**

2013 년 2월

서울대학교 대학원

재료공학부

김 원 식

가스센서 및 리튬이차전지용  
산화주석 및 실리콘 나노구조의 제조와 특성 평가

Fabrication and Characterization  
of Tin Oxide and Silicon Based Nanostructures  
for Gas Sensor and Li-ion Battery

지도교수 홍 성 현

이 논문을 공학박사 학위논문으로 제출함

2013 년 2 월

서울대학교 대학원

재료공학부

김 원 식

김원식의 박사학위논문을 인준함

2012년 12월

위 원 장	황 농 문	(인)
부 위 원 장	홍 성 현	(인)
위 원	강 기 석	(인)
위 원	박 재 관	(인)
위 원	최 현 진	(인)

## **Abstract**

---

Nanomaterials have been attracted due to their peculiar and fascinating properties, and applications superior to bulk materials. Various synthesis techniques for nanomaterials have been investigated and it is proven that the nanomaterials show the enhanced physical and chemical properties in various fields such as catalyst, sensors, and energy application.

In this research, the three main topics will be discussed: 1) synthesis of SnO<sub>2</sub> based hollow sphere and their electrochemical properties, 2) synthesis of one-dimensional SnO<sub>2</sub> nanostructures and control growth, 3) preparation of silicon nanostructure by magnesiothermic reduction for Li-ion battery application.

In the first chapter, design and synthesis of zero-dimensional SnO<sub>2</sub> based nanostructures for anode material of Li ion battery is studied. The demand for high energy and power density lithium ion batteries (LIBs) has increased in hybrid electric vehicles (HEVs) as well as light-weight and portable electronic devices. In commercial LIBs, graphite-based materials are widely used as an anode, but the theoretical capacity is only 372 mAhg. Therefore, intensive researches have been focused on the high capacity electrode materials such as Si, Ge, Sn, and SnO<sub>2</sub>. Among various candidates, SnO<sub>2</sub> is one of the promising materials for anode electrode in LIBs due to its high theoretical capacity (782 mAh g<sup>-1</sup>). However, a

large and uneven volume change, about 300%, occurs upon lithium insertion/extraction, which causes a pulverization and electrical connectivity loss. Hollow sphere is the most promising structure because the interior hollow space can accommodate the volume change during lithiation and delithiation. So, the electrochemical properties of SnO<sub>2</sub>-based hollow structures have been intensively investigated, and these structures showed an enhanced cycling performance compared to the solid SnO<sub>2</sub> nanoparticles. However, most of the studies have focused on the fabrication of unique nanostructures, and their size was limited to 100~200 nm. While the size of hollow spheres appears to be a crucial factor, the synthesis of size-controlled hollow spheres and the size dependence of the electrochemical properties have not been explored. In this study, the size-controlled SnO<sub>2</sub> hollow sphere is synthesized by simple sol-gel process at relatively low temperature and the SnO<sub>2</sub> hollow sphere electrodes showed the size dependent electrochemical properties, and the smallest SnO<sub>2</sub> (25 nm) hollow sphere exhibited a high reversible capacity of 750 mAh/g as well as excellent cyclability. Further improvement of reversible capacity is achieved by adding a Co<sub>3</sub>O<sub>4</sub> on the SnO<sub>2</sub> hollow sphere. The SnO<sub>2</sub>@Co<sub>3</sub>O<sub>4</sub> hollow sphere electrode shows a high reversible capacity of 963 mAh/g after 100 cycles and good rate capability.

In the second chapter, synthesis and control growth of one-dimensional

SnO<sub>2</sub> nanostructures are investigated. Metal oxide nanostructured sensors are the most promising devices among the solid state chemical sensors, because they have many advantages such as a large surface to volume ratio, a Debye length comparable to dimension of nanostructure, and low power consumption. SnO<sub>2</sub> is widely applied to semiconductor gas sensor, as well as anode for Li-ion battery. Especially, one-dimensional SnO<sub>2</sub> nanostructures, such as nanotube and nanowire, have very thin wall-thickness or diameter so it is favorable to detect a low concentration of gas. A novel method is developed to fabricate a SnO<sub>2</sub> nanotube network by utilizing electrospinning and atomic layer deposition (ALD), and the network sensor is proven to exhibit excellent sensitivity to ethanol owing to its hollow, nanostructured character. The electrospun polyacrylonitrile (PAN) nanofibers of 100–200 nm diameter are used as a template after stabilization at 250 °C. An uniform and conformal SnO<sub>2</sub> coating on the nanofiber template is achieved by ALD using dibutyltin diacetate (DBTDA) as the Sn source at 100 °C and the wall thickness is precisely controlled by adjusting the number of ALD cycles. The calcination at 700 °C transforms the amorphous nanofibers into SnO<sub>2</sub> nanotubes composed of several nanometer-sized crystallites. The SnO<sub>2</sub> nanotube network sensor responds to ethanol, H<sub>2</sub>, CO, NH<sub>3</sub> and NO<sub>2</sub> gases, but it exhibited an extremely high gas response to ethanol with a short response time (<5 s). Furthermore, single crystalline SnO<sub>2</sub> nanowire has been intensively investigated, as well. However, growth control of nanowire is important for fabrication of

reliable device and it required that understating the growth behavior of material. However, the growth behavior of SnO<sub>2</sub> nanowire is not well-investigated. Generally, aligned nanowire could be induce by understanding of (hetero)-epitaxial relationship between nanowire and substrate. In this study, SnO<sub>2</sub> nanowires were synthesized using a thermal evaporation and the epitaxial grown SnO<sub>2</sub> nanowires were well-aligned on the r-cut sapphire substrate. Two-types of growth mode, vertical and horizontal growth, are observed on the r-cut sapphire. At first, the vertically aligned SnO<sub>2</sub> nanowire shows three growth directions with specific growth angle and it is investigated that this growth behavior is resulted from rutile-tetragonal structure of SnO<sub>2</sub>. And horizontal growth is induced by control the distance of metal catalyst. The horizontally grown SnO<sub>2</sub> nanowire is self-aligned along the one direction and the width of laterally grown nanowire was well-controlled by catalyst size.

Most of all, silicon based systems are definitely attractive candidates since silicon has a large theoretical specific capacity at room temperature (Li<sub>15</sub>Si<sub>4</sub> : 3600 mAh g<sup>-1</sup>) and low operating voltage (around 0.1 V vs. Li/Li<sup>+</sup>). However, large volume change is occurred during the cycling and it leads to a poor rate capability. To overcome these problems, silicon nanostructures have been applied to anode materials of Li-ion battery and the enhanced electrochemical properties is achieved. But, synthesis of nanostructured silicon is required complicated route

with toxic precursor or high cost technique, such as CVD (chemical vapor deposition). Recently, magnesiothermic reduction is suggested as new method for synthesis of pure silicon from  $\text{SiO}_2$ . This is a low energy consumption process due to low processing temperature and short-term heat treatment.

In this study, a synthesis of silicon nanosheet is presented by magnesiothermic reduction and commercial sand is used as template and silicon source. As currently-known, the reduced Si is composed of a few nanometers sized silicon grain but the synthesized silicon nanosheet has large sized silicon grain, at least 20 nm. The synthesized silicon nanosheet show relatively better electrochemical performance than commercial nano-silicon powder. And the reversible capacity and cyclability is improved by applying the graphene wrapping on the silicon nanosheet. But the formation of large sized silicon grain is not explained by current reduction mechanism. So, the reduction mechanism is investigated, additionally. It is revealed that  $\text{Mg}_2\text{Si}$  is formed as intermediate phase in the initial stage of reduction at  $450 \sim 500$  °C, and silicon is generated by consumption of  $\text{Mg}_2\text{Si}$ . Furthermore, inverse opal liked silicon nanostructure is prepared on the concept of newly suggested reduction mechanism and the formation mechanism of inverse opal structure is investigated.

**Keywords:** Nanostructure, Hollow sphere, Core-shell, Sol-gel, Coating, Nanotube, ALD (atomic layer deposition), Nanowire, Thermal evaporation, Magnesiothermic reduction, Li-ion battery, Anode, SnO<sub>2</sub>, Co<sub>3</sub>O<sub>4</sub>, silicon.

**Student Number : 2006-20831**

## Table of Contents

---

<b>Abstract</b> .....	i
<b>Contents</b> .....	vii
<b>List of tables</b> .....	ix
<b>List of figures</b> .....	x
<b>Chapter 1. General Background</b> .....	1
1.1 Wet chemical method for synthesis of nanostructure .....	2
1.1.1. Homogeneous and heterogeneous nucleation and growth .....	2
1.1.2. Sol-gel method .....	5
1.2. Synthesis of one-dimensional nanostructure .....	7
1.2.1. Synthesis of nanowire by VLS (vapor-liquid-solid) process .....	7
1.2.2. Hetero/epitaxial growth of nanowire .....	12
1.3. Preparation of silicon by reduction process .....	15
1.3.1. Reduction of SiO <sub>2</sub> to Si .....	15
1.3.2. Magensiothermic reduction for silicon nanostructure .....	17
1.4. Reference .....	23
<b>Chapter 2. Synthesis of Zero-dimensional SnO<sub>2</sub> Nanostructures for     Li-ion Battery</b> .....	28
2.1. Synthesis of SnO <sub>2</sub> hollow sphere with size-control for Li-ion battery application .....	29
2.2. Transition metal oxide coated SnO <sub>2</sub> hollow sphere and their extraordinary electrochemical properties .....	45

2.3. References .....	66
<b>Chapter 3. Preparation of one-dimensional SnO<sub>2</sub> Nanostructures for Gas Sensing Application .....</b>	<b>71</b>
3.1. Synthesis of SnO <sub>2</sub> nanotube for gas sensing application .....	72
3.2. Vertically grown SnO <sub>2</sub> nanowire on r-cut sapphire .....	93
3.3. Horizontal growth of SnO <sub>2</sub> nanowire with one-directional Alignment .....	113
3.4. References and Notes .....	130
<b>Chapter 4. Magnesiothermic reduced Silicon nanostructure for Li ion Battery Application .....</b>	<b>141</b>
4.1. Synthesis of reduced graphene oxide wrapped silicon nanosheet from natural sand and their electrochemical properties.....	142
4.2. Understanding of magnesiothermic reduction .....	159
- Reduction mechanism of silicon nanoparticle .....	162
- Formation mechanism of inverse opal-liked silicon nanostructure ....	171
4.3 Conclusion .....	184
4.4. References .....	185
<b>Abstract (Korean) .....</b>	<b>187</b>

## List of Table

---

**Table 2.1.1.** Experimental conditions for synthesis of SiO<sub>2</sub> colloids.

**Table 2.1.2.** Experimental condition for SnO<sub>2</sub> coating process.

**Table 4.1.1.** (a)-(c) HCl treated products, (d) Schematic illustration of the synthesis of silicon nanosheet.

**Table 4.2.1.** The phase evolution of magnesiothermic reduction with different temperature.

## List of Figures

---

### Chapter 1

**Figure 1.1.1.** The reduction of the overall Gibbs free energy of a supersaturated solution by forming a solid phase.

**Figure 1.1.2.** The excess free energy of solid clusters for homogeneous and heterogeneous nucleation.

**Figure 1.2.1** (a) The stages of (I) alloying, (II) nucleation and (III) growth of nanowire synthesis according to the VLS growth mechanism. (b) Pseudobinary phase diagram of a semiconductor (SC)-gold system. The arrows indicate the subsequent phases when a gold droplet absorbs semiconductor material at a constant temperature.

**Figure 1.2.2.** (a) Schematic illustrating size-controlled synthesis of Si NWs from Au nanoparticles, (b) Histograms of Si NW diameters grown from 5, 10, 20, and 30 nm diameter of Au nanoparticles, (c) HRTEM images of 6.7-nm, 10.7 nm, and 20.6 nm diameter NWs grown from 5, 10, and 20 nm catalysts, respectively. The scale bars are 2, 5, and 10 nm, respectively. The black lines indicate the crystalline Si core.

**Figure 1.2.3.** (a) Langmuir-Blodgett compression, (b) Electric field assembly, (c) Fluidic flow assembly, (d) Surface-programmed assembly (e) Direct contact

printing.

**Figure 1.2.4.** Graphoepitaxial effect on the guided VLS growth of horizontal nanowires. (A) Graphoepitaxial effect on C-plane sapphire (schematic). (B) Corresponding scanning electron microscope (SEM) images. (C) Graphoepitaxial effect on M-plane sapphire (schematic). (D) Corresponding SEM images.

**Figure 1.3.1.** Principal parts of a modern silicon plant.

**Figure 1.3.2.** Phase diagram of Mg-Si.

**Figure 1.3.3.** Gibbs free energy of the reactions as a function of temperature.

**Figure 1.3.4.** (a)-(c) as reduced Si-MgO composite, (d)-(f) Acid treated mesoporous silicon nanostructure.

**Figure 1.3.5.** Silicon nanostructures, prepared by magnesiothermic reduction: (a) nanosheet, (b) hollow sphere, (c) nanotube, (d) silicon-carbon composite, (e) silicon-CNT composite, (d) silicon-graphene composite.

## Chapter 2

**Figure 2.1.1.** (a, b) Low and high magnification TEM images of as-coated SiO<sub>2</sub>-SnO<sub>2</sub> core-shells; (c, d) 25 nm sized SnO<sub>2</sub> hollow spheres after annealing and removal of SiO<sub>2</sub>; (e) SAED patterns of as-coated SnO<sub>2</sub>-SiO<sub>2</sub> core-shells (upper) and SnO<sub>2</sub> hollow spheres (bottom); (f) XRD patterns of SiO<sub>2</sub>-SnO<sub>2</sub> core-shells and SnO<sub>2</sub> hollow spheres.

**Figure 2.1.2.** As prepared SiO<sub>2</sub>-SnO<sub>2</sub> core-shells at different synthesis

temperature: (a) 40, (b) 60, (c) 80, and (d) 100 °C.

**Figure 2.1.3.** TEM and HRTEM images of size controlled SnO<sub>2</sub> hollow sphere: (a, b) 50 nm; (c, d) 100 nm.

**Figure 2.1.4.** (a) Charge/discharge voltage profile of 25 nm sized SnO<sub>2</sub> hollow sphere between 0.01 and 2.5 V at 100 mA g<sup>-1</sup>; (b) rate capability test of 25 nm sized SnO<sub>2</sub> hollow sphere; (c) cyclability of SnO<sub>2</sub> hollow spheres with different size and commercial SnO<sub>2</sub> nanopowder at 100 mAh g<sup>-1</sup>.

**Figure 2.1.5.** Charge/discharge voltage profiles of SnO<sub>2</sub> hollow spheres between 0.0 and 2.5 V at 100 mAh g<sup>-1</sup> : (a) 50 nm, (b) 100 nm, and (c) commercial SnO<sub>2</sub> nanopowder, (d) columbic efficiency.

**Figure 2.1.6.** TEM images of SnO<sub>2</sub> electrode: a) pristine and b) after 20 cycles; c) HRTEM image of b). d) SEM images of SnO<sub>2</sub> hollow sphere after 50 cycles.

**Figure 2.2.1.** SEM images of (a) SnO<sub>2</sub> hollow sphere and (b) SnO<sub>2</sub>@cobalt oxide hollow sphere.

**Figure 2.2.2.** (a) XRD of SnO<sub>2</sub> hollow sphere and SnO<sub>2</sub>@cobalt oxide hollow sphere, (b) Co2p XPS of SnO<sub>2</sub>@cobalt oxide hollow sphere.

**Figure 2.2.3.** TEM images of SnO<sub>2</sub>@cobalt oxide hollow sphere (a) low- and (b) high- magnification.

**Figure 2.2.4.** (a) STEM images of SnO<sub>2</sub>@cobalt oxide hollow sphere and EDX

mapping of (b) cobalt and (c) Tin. (d) and (e) line scan profile of Co and Tin elements.

**Figure 2.2.5.** Voltage profiles of (a) SnO<sub>2</sub> and (b) SnO<sub>2</sub>@Co<sub>3</sub>O<sub>4</sub> multi-layered hollow sphere between 0.01 and 2.5 V at 100 mA g<sup>-1</sup>, rate capabilities of (c) SnO<sub>2</sub> and (d) SnO<sub>2</sub>@Co<sub>3</sub>O<sub>4</sub> multi-layered hollow sphere.

**Figure 2.2.6.** (a) cycling performance of SnO<sub>2</sub> and SnO<sub>2</sub>@Co<sub>3</sub>O<sub>4</sub> multi-layered hollow sphere at 100 mA g<sup>-1</sup>, (b) cycling performance of SnO<sub>2</sub>@Co<sub>3</sub>O<sub>4</sub> multi-layered hollow sphere at 100, 500, and 900 mA g<sup>-1</sup>.

**Figure 2.2.7.** (a) and (b) TEM images of SnO<sub>2</sub>@Co<sub>3</sub>O<sub>4</sub> hollow sphere after 50 cycles at 100 mA g<sup>-1</sup>.

**Figure 2.2.8.** (a) DCP (differential capacity plot) of SnO<sub>2</sub>@cobalt oxide hollow sphere at 1<sup>st</sup> and 2<sup>nd</sup> cycles, (b) ex-situ XRD analysis.

**Figure 2.2.9.** Ex-situ TEM images with SAED patterns of the SnO<sub>2</sub>@Co<sub>3</sub>O<sub>4</sub> hollow sphere electrode. Discharge process: (a) 1.20 V, (b) 0.68 V, (c) 0.00V.

**Figure 2.2.10.** Ex-situ TEM images with SAED patterns of the SnO<sub>2</sub>@Co<sub>3</sub>O<sub>4</sub> hollow sphere electrode. Charge process: (a) 0.90 V, (b) 2.50 V.

## Chapter 3

**Figure 3.1.1.** FESEM images of (a) as-electrospun PAN nanofibers, (b) as-stabilized PAN nanofibers at 250 °C, (c) SnO<sub>2</sub> coated PAN nanofibers by ALD (300 cycles at 100 °C), and (d) SnO<sub>2</sub> nanotubes after calcination at 700 °C. The inset clearly showed the tubular morphology of nanofibers.

**Figure 3.2.2.** FESEM images of non-stabilized PAN nanofibers (a) after SnO<sub>2</sub> coating by ALD at 100 °C, (b) after calcining of (a) at 700 °C, (c) after SnO<sub>2</sub> coating by ALD at 200 °C, and (d) after calcining of (c) at 700 °C.

**Figure 3.1.3.** XRD patterns of (a) as-electrospun PAN nanofibers, (b) as-stabilized PAN nanofibers at 250 °C, (c) SnO<sub>2</sub> coated PAN nanofibers by ALD (300 cycles at 100 °C), and (d) SnO<sub>2</sub> nanotubes after calcination at 700 °C.

**Figure 3.1.4.** (a) Low magnification and (b), (c) high resolution TEM images of SnO<sub>2</sub> nanotubes (100 cycles at 100 °C) after calcination at 700 °C. The inset in (b) is the SAED pattern of SnO<sub>2</sub> nanotubes.

**Figure 3.1.5.** Low magnification TEM images of SnO<sub>2</sub> nanotubes after calcination at 700 °C; (a) 100 (b) 300 (c) 500 ALD cycles, and (d) Wall thickness of SnO<sub>2</sub> nanotubes as a function of ALD cycles measured by TEM.

**Figure 3.1.6.** (a) Optical and (b) SEM micrographs of SnO<sub>2</sub> nanotube network sensor placed on Pt patterned SiO<sub>2</sub>/Si substrate.

**Figure 3.1.7.** Typical response transient of SnO<sub>2</sub> nanotube network sensor toward 100 ppm ethanol

**Figure 3.1.8.** (a) Magnitude of gas response and (b) response time of SnO<sub>2</sub> nanotube network sensors toward 100 ppm ethanol as a function of sensing temperature.

**Figure 3.1.9.** (a) Ethanol concentration dependence of gas response (b) concentration dependence of gas response at 450 °C, and (c) selectivity of SnO<sub>2</sub> nanotube network sensor toward ethanol against H<sub>2</sub>, CO, NH<sub>3</sub>, and NO<sub>2</sub> gases. In (a), the resistance in sample gas was normalized by the resistance in air for clarity.

**Figure. 3.2.1.** (a) Tilted FESEM image of aligned SnO<sub>2</sub> nanowires grown on r-cut sapphire. The inset is the cross-sectional view of individual nanowire. (b)  $\theta$ - $2\theta$  X-ray diffraction of SnO<sub>2</sub> nanowires.

**Figure 3.2.2.** (a) {001} pole figure of (012) sapphire substrate. (b) {101} pole figure of SnO<sub>2</sub> nanowires at 33.89 ° Bragg angle. Stereographic projection of (c) (012) sapphire and (d) (101) SnO<sub>2</sub>.

**Figure 3.2.3.** Cross-sectional FESEM images of aligned SnO<sub>2</sub> nanowires grown on r-cut sapphire; (a) viewed along the [100] direction and (b) viewed along the [12 $\bar{1}$ ] direction of r-cut sapphire.

**Figure 3.2.4.** (a) Crystal structure of rutile SnO<sub>2</sub>. The <101> family directions of SnO<sub>2</sub> viewed along the (a) [010] and (b) [100] direction.

**Figure 3.2.5.** (a) Cross-sectional TEM image of (101) SnO<sub>2</sub> nanowires grown on sapphire ([101] growth direction). (b) HRTEM image of a SnO<sub>2</sub> nanowire on sapphire. Incident beam is in the [100] direction of sapphire. (c), (d), and (e) FFT patterns of SnO<sub>2</sub> nanowire, interface, and sapphire substrate marked by the boxes in panel (b), respectively. (f) high-magnification image of SnO<sub>2</sub>/sapphire interface. (g) Fourier filtered image of (f).

**Figure 3.2.6.** (a) Cross-sectional TEM image of (101) SnO<sub>2</sub> nanowire on sapphire ([011] growth direction). (b), (c), and (d) FFT patterns of SnO<sub>2</sub> nanowire, interface, and sapphire, respectively.

**Figure 3.2.7.** (a) HRTEM image of Au catalyst at the tip of SnO<sub>2</sub> nanowire. (b) and (c) FFT patterns of Au catalyst and SnO<sub>2</sub> nanowire, respectively. (d) high magnification image of Au/SnO<sub>2</sub> interface.

**Figure 3.2.8.** EDS spectra of Au catalyst and SnO<sub>2</sub> nanowire.

**Figure 3.2.9.** (a) and (b) TEM images of branched SnO<sub>2</sub> nanowires. (c)-(f) FFT patterns of nanowires marked by the boxes in panel (b). (g) HRTEM image of nanowire junction. (h) and (i) TEM images of branched SnO<sub>2</sub> nanowires with Au catalyst.

**Figure. 3.3.1.** SEM images of horizontally grown SnO<sub>2</sub> nanowire.

**Figure 3.3.2.** (a) {001} pole figure of (012) sapphire substrate. (b) {101} pole figure of SnO<sub>2</sub> nanowires at 33.89 ° Bragg angle. Crystal structure of (c) (012)

sapphire and (d) (101) SnO<sub>2</sub>.

**Figure 3.3.3.** The growth of horizontal SnO<sub>2</sub> nanowire with different direction of gas injection.

**Figure 3.3.4.** Cross-sectional TEM image with [010] zone axis of SnO<sub>2</sub>.

**Figure 3.3.5.** Cross-sectional TEM image with [ $\bar{1}01$ ] zone axis of SnO<sub>2</sub>.

**Figure 3.3.6.** The horizontally grown SnO<sub>2</sub> nanowire with different catalyst size, (a) and (b) : 5 nm, (c) and (d) : 20 nm, (e) and (f) 80 nm.

**Figure 3.3.7.** Ultra-long, horizontally grown SnO<sub>2</sub> nanowire from patterned Au thin-film.

**Figure 3.3.8.** Transformation of growth behavior of SnO<sub>2</sub> nanowire from horizontal to vertical growth.

## Chapter 4

**Figure 4.1.1.** XRD patterns of (a) ball-milled sand, (b) as reduced silicon, (c) HCl and (d) HF acid treated silicon nanosheet.

**Figure 4.1.2.** SEM image of (a) commercial sand, (b) ball-milled sand, (c) and (d) synthesized silicon nanosheet.

**Figure 4.1.3.** (a) low magnification TEM image of silicon nanosheet, (b) SAEP of silicon nanosheet, (c) and (d) HRTEM image of silicon nanosheet.

**Figure 4.1.4.** Nitrogen adsorption–desorption isotherms of (a) commercial silicon nanoparticle, (b) synthesized silicon nanosheet.

**Figure 4.1.5.** (a)-(c) HCl treated products, (d) Schematic illustration of the synthesis of silicon nanosheet.

**Figure 4.1.6.** TEM and SAEP image of graphene wrapped silicon nanosheet.

**Figure 4.1.7.** (a) Voltage profiles of silicon nanosheet and graphene encapsulated silicon nanosheet electrodes after 1, 2, 10, 30, 50 cycles at 200 mA g<sup>-1</sup> between 0 and 2.0 V. (b) Cyclability of commercial nano-silicon powder, silicon nanosheet and graphene wrapped silicon nanosheet, (c) rate capability of graphene wrapped silicon nanosheet.

**Figure 4.2.1.** (a) Effect of magnesium/silica ratio and temperature on (a) Si yield and (b) Mg<sub>2</sub>Si amount.

**Figure 4.2.2.** XRD pattern of reduced SiO<sub>2</sub> with different processing temperature.

**Figure 4.2.3.** (a) 500 °C for 0, 1, 4, 8 h, (b) 600 °C for 0, 1, 2h, (c) 700 °C for 0, 1h.

**Figure 4.2.4.** HCl treated reduced SiO<sub>2</sub>, (a)-(c) 500 °C for 1h, (d)-(g) 500 °C for 8h.

**Figure 4.2.5.** Schematic illustration of magnesiothermic reduction.

**Figure 4.2.6.** SEM image of (a) SiO<sub>2</sub> nanopowder, (b)-(d) inverse opal liked silicon nanostructure.

**Figure 4.2.7.** XRD pattern of (a) as reduced SiO<sub>2</sub>, at 700 °C for 1hr, and (d) HCl treated sample.

**Figure 4.2.8.** (a),(c),(d) TEM image of invers opal liked silicon structure and (b) SAED. (e) HR-TEM image of silicon and (f) inverse FFT image of (e).

**Figure 4.2.9.** XRD pattern of different reduction temperature (without holding time).

**Figure 4.2.10.** Different shape of silicon nanostructure with different processing schedule, (a) inverse opal liked silicon and (b) silicon nanoparticle.

**Figure 4.2.11.** Schematic illustration of formation mechanism (inverse opal liked silicon).

# **Chapter 1.**

## **General Background**

## 1.1 Wet chemical method for synthesis of nanostructure

### 1.1.1. Homogeneous and heterogeneous nucleation and growth

In the wet-chemical process, the precipitation (or nucleation) is generally occurred by concentration of a solute or decreasing temperature. In case of homogeneous nucleation of a solid phase from a supersaturated solution, the solution with solute exceeding the solubility or supersaturated possesses a high Gibbs free energy; the overall energy of the system would be reduced by segregating solute from the solution. Figure 1.1.1 is a schematic showing the reduction of the overall Gibbs free energy of a supersaturated solution by forming a solid phase and maintaining an equilibrium concentration in the solution.

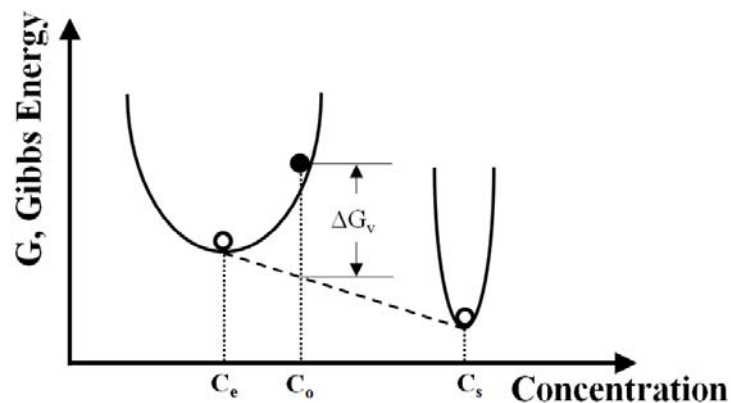


**Figure 1.1.1.** The reduction of the overall Gibbs free energy of a supersaturated solution by forming a solid phase.

This reduction of Gibbs free energy is the driving force for both nucleation

and growth. The change of Gibbs free energy per unit volume of the solid phase,  $\Delta G_v$ , is dependent on the concentration of the solute:

$$\Delta G_v = -\frac{kT}{\Omega} \ln\left(\frac{C}{C_0}\right) = -\frac{kT}{\Omega} \ln(1 + \sigma)$$

where  $C$  is the concentration of the solute,  $C_0$  is the equilibrium concentration or solubility,  $\Omega$  is the atomic volume, and  $\sigma$  is the supersaturation defined by  $(C - C_0)/C_0$ . Without supersaturation (i.e.,  $\sigma = 0$ ),  $\Delta G_v$  is zero, and no nucleation would occur.

When  $C > C_0$ ,  $\Delta G_v$  is negative and nucleation occurs spontaneously. Assuming a spherical nucleus with a radius of  $r$  is formed, the change of Gibbs free energy or volume energy,  $\Delta\mu_v$ , can be described by:

$$\Delta\mu_v = \frac{4}{3}\pi r^3 \Delta G_v$$

However, this energy reduction is counter balanced by the introduction of surface energy, which accompanied with the formation of new phase. This results in an increase in the surface energy,  $\Delta\mu_s$ , of the system:  $\Delta\mu_s = 4\pi r^2 \gamma$ , where  $\gamma$  is the surface energy per unit area. The total change of chemical potential for the formation of the nucleus,  $\Delta G_{\text{homo}}$ , is given by:

$$\Delta G_{\text{homo}} = \Delta\mu_v + \Delta\mu_s = \frac{4}{3}\pi r^3 \Delta\Delta G_v + 4\pi r^2 \gamma, (\Delta G_v < 0)$$

Figure 1.1.2 schematically shows  $\Delta G_{\text{homo}}$ . From this figure, one can easily see that the newly formed nucleus is stable only when its radius exceeds a critical size,  $r^*$ . A nucleus smaller than  $r^*$  will dissolve into the solution to reduce the overall free energy, whereas a nucleus larger than  $r^*$  is stable and continues to grow bigger. At the critical size  $r = r^*$ ,  $d\Delta G/dr = 0$  and the critical size,  $r^*$ , and critical energy,  $\Delta G^*_{\text{homo}}$ , are defined by:

$$r^*_{\text{homo}} = -\frac{2\gamma}{(\Delta G_v)}, \text{ and } \Delta G^*_{\text{homo}} = \frac{16\pi\gamma^3}{3(\Delta G_v)^2}$$

$\Delta G^*_{\text{homo}}$  is the energy barrier that a nucleation process must overcome and  $r^*_{\text{homo}}$  represents the minimum size of a stable spherical nucleus. The above discussion was based on a supersaturated solution; however, all the concepts can be generalized for a supersaturated vapor and a supercooled vapor or liquid.

In the heterogeneous nucleation, the  $\Delta G_{\text{het}}$ ,  $r^*_{\text{het}}$  and  $\Delta G^*_{\text{het}}$  are defined by:

$$\Delta G_{\text{het}} = \left\{ \frac{4}{3}\pi r^3 \Delta G_v + 4\pi r^2 \gamma \right\} S(\theta), (\Delta G_v < 0)$$

$$r^*_{\text{het}} = -\frac{2\gamma}{(\Delta G_v)} \text{ and } \Delta G^*_{\text{het}} = \frac{16\pi\gamma^3}{3(\Delta G_v)^2} S(\theta)$$

$$\text{where, } S(\theta) = \frac{(2 + \cos \theta)(1 - \cos \theta)^2}{4}$$

$S(\theta)$  has a numerical value  $\leq 1$ , therefore the activation energy barrier against heterogeneous nucleation is smaller than that of homogeneous nucleation. But, the nucleus radius ( $r^*$ ) is not changed.

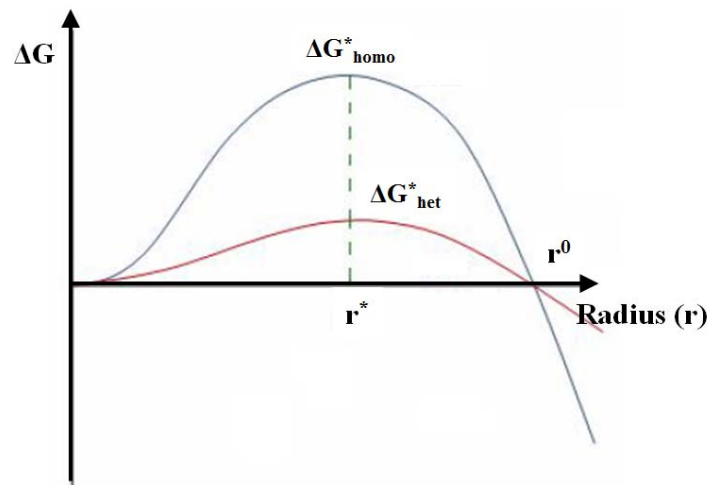


**Figure 1.1.2.** The excess free energy of solid clusters for homogeneous and heterogeneous nucleation.

\* Note: This chapter is summarized from “Phase Transformations in Metals and Alloys”, D.A. Potter and K. E. Eastering.

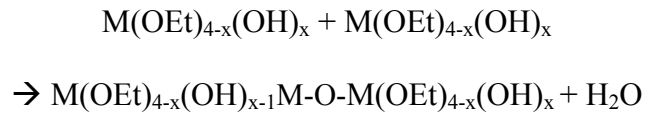
### 1.1.2. Sol-gel method

Sol-gel processing is a wet chemical route for the synthesis of colloidal dispersions of inorganic and organic-inorganic hybrid materials, particularly oxides, hydroxide and oxide-based hybrids. From such colloidal dispersions, powders, fibers, and thin films can be readily prepared and core-shell, hollow structure can be synthesized, as well. Furthermore, size of colloid particle is relatively controllable, so it is simply prepared bulk materials as well as nanomaterials. Although the fabrication of different forms of final products requires some specific considerations, fundamentals and general approaches in the synthesis of colloidal dispersions are the same. Sol-gel processing offers many advantages, including low processing temperature and molecular level homogeneity. Sol-gel processing is particularly useful in making complex metal oxides, temperature sensitive organic-inorganic hybrid materials, and thermodynamically unfavorable or metastable materials. Typical sol-gel processing consists of hydrolysis and condensation of precursors. Precursors can be either metal alkoxides or inorganic and organic salts. Organic or aqueous solvents may be used to dissolve precursors, and catalysts are often added to promote hydrolysis and condensation reactions:

1)Hydrolysis:



2) Condensation:



A synthesis of SiO<sub>2</sub> is well-known sol-gel process. It is studied that the reaction rate and particle size were strongly dependent on solvents, precursors, amount of water, and ammonia.[1,2] For the different alcoholic solvents, reaction rates were fastest with methanol, slowest with n-butanol. Likewise, final particle sizes obtained under comparable conditions were smallest in methanol and biggest in n-butanol. However, there was a tendency toward wide size distributions with the higher alcohols. Similar relationship with regard to reaction rates and particle sizes was found when comparing results with different ligand sizes in the precursors. Smaller ligand resulted in faster reaction rate and smaller particle size, whereas larger ligands led to slower reaction rate and large particle size. Ammonia was found necessary for the formation of spherical silica particles, since condensation reaction under a basic condition yields three dimensional structure instead of a linear polymeric chain which occurs under an acidic condition.

## **1.2. Synthesis of one-dimensional nanostructure**

### **1.2.1. Synthesis of nanowire by VLS (vapor-liquid-solid) process**

Semiconductors or metal oxide are at the core of the most advanced technologies in electronic and optical devices, but defects induced by stress during

growth often degrade the electronic and optical properties. The vapor-liquid-solid (VLS) growth method, first described in 1964 [3], has attracted overwhelming renewed attention during the past decade, as a means of producing stress-free single-crystal semiconductor nanowires with unparalleled electronic and optical properties suitable for ultraminiaturized electronics [4], optoelectronics [5], Li-ion battery [6], solar cell [7,8], and chemical and biological sensing [9].

Nanowires are commonly grown using vapor, solution or (template directed) electrodeposition methods. High temperature growth from the vapor phase is often preferred due to the high crystal quality that can be obtained and the ability to grow large quantities of wires at once. So nanowires, grown by VLS mechanism, have been intensively attracted. The VLS mechanism consists of three stages which are illustrated in Figure 1.2.1(a) First, a metal particle (usually, gold) absorbs semiconductor material and forms an alloy. In this step the volume of the particle increases and the particle often transitions from a solid to a liquid state. Second, the alloy particle absorbs more semiconductor material until it is saturated. The saturated alloy droplet becomes in equilibrium with the solid phase of the semiconductor and nucleation occurs (i.e solute/solid phase transition). During the final phase, a steady state is formed in which a semiconductor crystal grows at the solid/liquid interface. The precipitated semiconductor material grows as a wire because it is energetically more favorable than extension of the

solid/liquid interface.

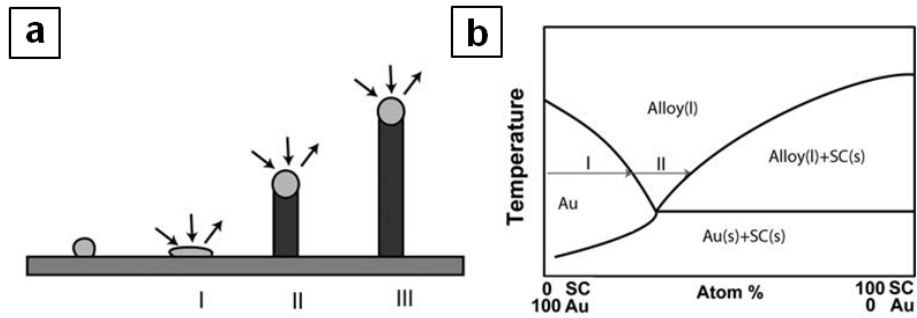


**Figure 1.2.1** (a) The stages of (I) alloying, (II) nucleation and (III) growth of nanowire synthesis according to the VLS growth mechanism. (b) Pseudobinary phase diagram of a semiconductor (SC)-gold system. The arrows indicate the subsequent phases when a gold droplet absorbs semiconductor material at a constant temperature.

In the VLS mechanism, the diameter of nanowire could be controlled by catalyst size.[10] The diameter of nanowire is determined by the diameter of metal catalyst or alloy particle. However, there are limitations for downsizing of nanowire. Thermodynamically, the minimum radius of a liquid metal droplet is given as [11]

$$r_l^{min} = \frac{2V_l\sigma_{l-v}}{RT \ln(s)}$$

where  $V_l$  is the molar volume of the droplet,  $\sigma_{l-v}$  is the liquid–vapor surface energy, and  $s$  is the degree of supersaturation of the vapor. According to this equation, using a smaller catalyst requires a higher degree of supersaturation. However, the chemical potential of the component in the metal–alloy catalyst becomes high as the size of the catalyst decreases due to the Gibbs–Thompson effect:

$$\Delta\mu = \frac{2\gamma}{r}$$

Here,  $\Delta\mu$  is the chemical potential difference of the component species in the liquid droplet,  $\gamma$  is the surface energy, and  $r$  is the radius of curvature of the droplet. Therefore, dissolving a vapor component into a liquid alloy becomes increasingly difficult as the size decreases, making it difficult to reach supersaturation states that sufficiently induce the growth of nanowires. Indeed, it is known that the growth of 1D structure with diameters of several tenths of nm is feasible; however, ensuring a smaller diameter is difficult due to the thermodynamic limitations associated with the use of a nanocatalyst. Additionally, the deformation or evaporation of metal catalyst is also problem for diameter decreasing of nanowire. Usually, metal catalysts are applied in the shape of nano-colloid or thin film. In case of nano-colloid, the agglomeration is occurred by strong van der Waals attractive forces and it disturbs the exact size control and the

downsizing. Moreover, the small sized metal catalyst is easily melted and evaporated, it is getting sever with size decreasing of metal catalyst. In case of thin film, thin film is changed to nanoparticle on the substrate during heating up to processing temperature. Uniform size control of metal catalyst from thin film is very difficult due to Ostwald ripening. Larger metal particles are more energetically favorable, so synthesis of smaller diameter of nanowire is limited, as well.[12]

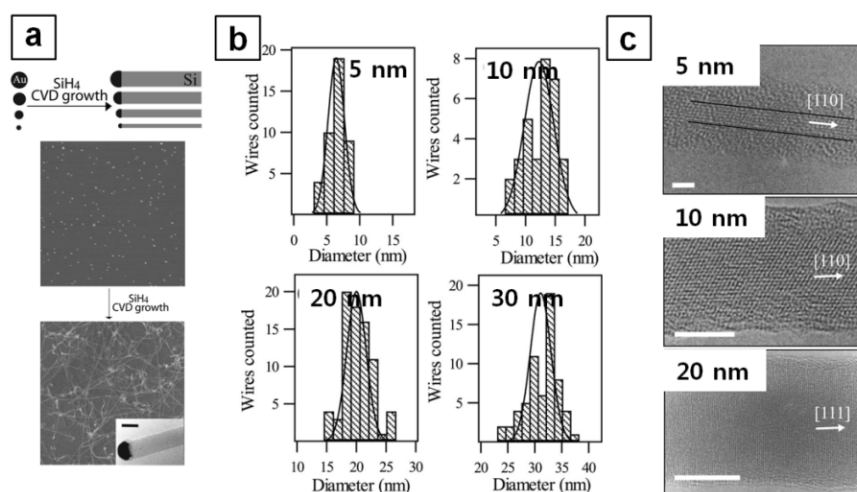


**Figure 1.2.2.** (a) Schematic illustrating size-controlled synthesis of Si NWs from Au nanoparticles, (b) Histograms of Si NW diameters grown from 5, 10, 20, and 30 nm diameter of Au nanoparticles, (c) HRTEM images of 6.7-nm, 10.7 nm, and 20.6 nm diameter NWs grown from 5, 10, and 20 nm catalysts, respectively. The scale bars are 2, 5, and 10 nm, respectively. The black lines indicate the crystalline Si core.[10]

### **1.2.2. Hetero/epitaxial growth of nanowire**

With increasing the attraction for nanowire and nanowire based devices, the well-grown, selectively-grown and well-aligned nanowires have been investigated. Recently, well-defined nanowires are applied toward various applications. Liber's group show the nano-sized memory using selectively grown nanowire [13] and Yang et al investigated nano-laser by using vertically aligned ZnO nanowires [14]. Wang's group developed the nanogenerator by using piezoelectric properties of well-aligned ZnO nanowire [15] and the Field-Effect Transistor is designed by vertically aligned nanowire [16]. Moreover, well-aligned nanowire is recently applied to solar cell and dye-sensitized solar cell [8].

The most effective approach for synthesis of well-aligned nanowire is using epitaxial (or hetero-epitaxial) relationship between nanowire and substrate. The (hetero)-epitaxial relationship of nanowire is exactly same to that of thin film. Especially, the strain energy due to lattice mismatch between nanowire and substrate releases during growth of nanowire, so generation of structural defect, such as dislocation, is restricted. Vertically well-aligned nanowires have been successfully synthesized using hetero-epitaxial growth by various techniques in a variety of systems including Si, Ge, InAs, GaAs, In<sub>2</sub>O<sub>3</sub>, Ga<sub>2</sub>O<sub>3</sub>, and ITO.[17-23]

The large-scale assembly of horizontal nanowires with controlled orientation on surfaces remains a challenge toward their integration into practical

devices. For the fabrication of nanowire based devices, several assembly processes have been devised, including the use of Langmuir-Blodgett compression,[24] electric fields,[25] Fluidic flow assembly,[26] surface programmed assembly [27] and etc.[28] Although these post growth assembly methods yield relatively well-aligned arrays on a variety of surfaces on a wafer-scale size, their alignment is subject to thermal and dynamic fluctuations. The assembled nanowires are usually not much longer, and there is no control over their crystallographic orientation. Moreover, these ex-situ alignment techniques are mostly complicated and nanowires might be contaminated by solvents during these process. So, in-situ alignment of nanowire during growth is a one of key technique for desirable nanowire-based device. Recently, horizontal (or lateral) growth behavior of nanowire toward various materials has been attracted because the horizontally grown nanowire is able to be aligned to one-direction by controlling of orientation or morphology of substrate without further assembly treatment. [29-33].

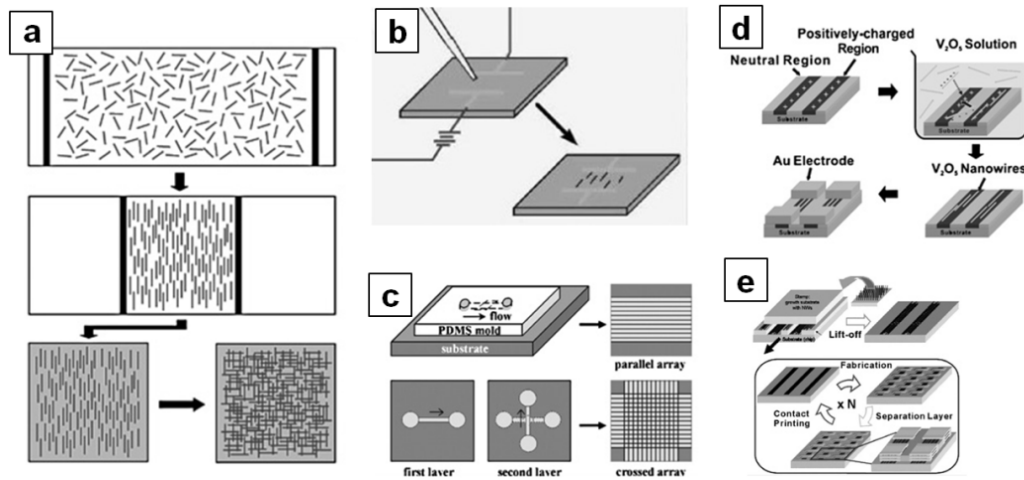


**Figure 1.2.3.** (a) Langmuir-Blodgett compression, (b) Electric field assembly, (c) Fluidic flow assembly, (d) Surface-programmed assembly (e) Direct contact printing.

For example, horizontally grown GaN nanowires are shown in Figure 1.2.4. The horizontal GaN nanowires were controlled crystallographic orientations on different planes of sapphire. The growth directions, crystallographic orientation, and faceting of the nanowires vary with each surface orientation, as determined by their epitaxial relationship with the substrate, as well as by a graphoepitaxial effect that guides their growth along surface steps and grooves.

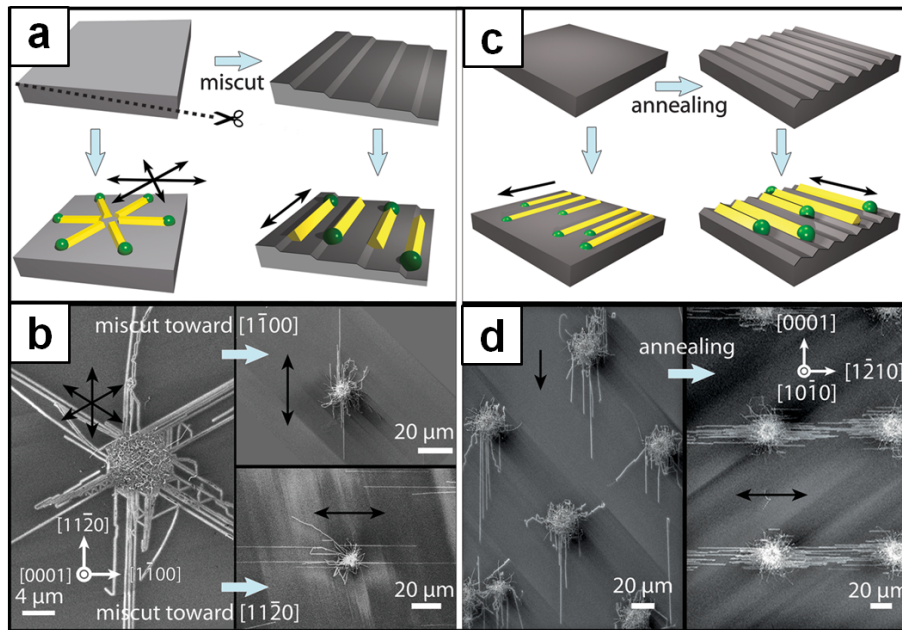


**Figure 1.2.4.** Graphoepitaxial effect on the guided VLS growth of horizontal nanowires. (A) Graphoepitaxial effect on C-plane sapphire (schematic). (B) Corresponding scanning electron microscope (SEM) images. (C) Graphoepitaxial effect on M-plane sapphire (schematic). (D) Corresponding SEM images.[29]

### 1.3. Preparation of silicon by Reduction process

#### 1.3.1. Reduction of $\text{SiO}_2$ to Si (Carbothermic Reduction)

The most economically feasible way to produce silicon metal as a commodity material of high purity (>99%) is still by carbothermic reduction in an electric submerged arc furnace. Carbon from charcoal, wood chips, coal and coke is used as reduction agent in the silicon process to release the silicon from quartz.

At present, silicon (metallurgical grade silicon) is being produced using electric arc furnace based on carbothermic reaction. Fig. 1.3.1 shows the modern silicon plant for production of metallurgical grade silicon.[34]

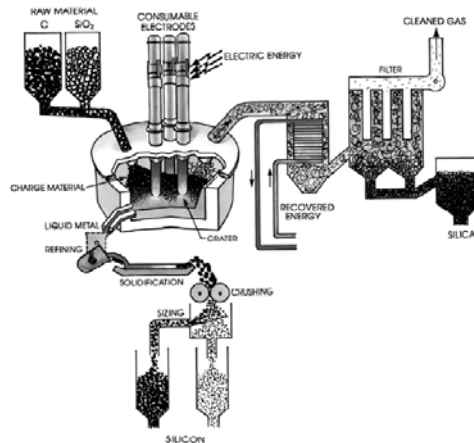
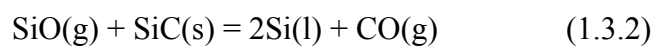
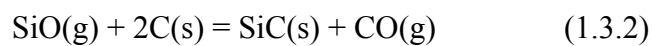
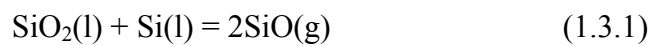


**Figure 1.3.1.** Principal parts of a modern silicon plant.

In this process, quartz rock and various reducing agents such as coke, coal and wood chips are charged to the furnace and the temperature raised up to 2400K (2127 °C) by electric arc. Silica is reduced by the reaction with carbon.

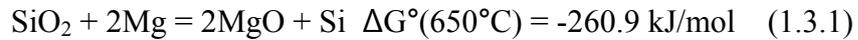
The following intermediate reactions occur to complete the reduction process,[35]



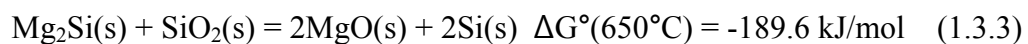
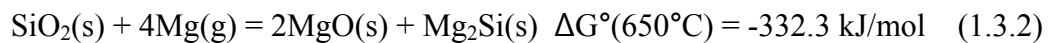
In this process the reductant mixture consisting of lignite, petroleum-coke, charcoal and wood chips are the major source of various contaminants in the end product, and hence the purity level (99.88%).

### 1.3.2. Magnesiothermic reduction for silicon nanostructure

Sandhage's group reported conversion of diatom frustules ( $\text{SiO}_2$ ) to porous nanocrystalline silicon using Mg vapor at  $650^\circ\text{C}$  (melting point of magnesium).[36] The reduction of  $\text{SiO}_2$ , by magnesium, is conducted through the following reaction:



The above reaction is generally accepted for the magnesiothermic reduction but it is also suggested that above reaction may involve formation of  $\text{Mg}_2\text{Si}$  in the early stages, followed by reduction of  $\text{SiO}_2$  by  $\text{Mg}_2\text{Si}$  through the following chemical reactions:



The  $\text{Mg}_2\text{Si}$ , intermetallic compound between Si and Mg, is quietly stable and formed from low temperature (Figure 1.3.2). The  $\Delta G$  of these two reaction is negative from room temperature, and  $\Delta G$  of equation (1.3.3) is more negative (Figure 1.3.3). This indicates that these possible reactions are thermodynamically more favorable than equation (1.3.1). But, these reactions are not proven experimentally because the magnesiothermic reduction is usually conducted at high temperature, over 650 °C. So, the kinetic during reduction is too fast to investigate the evolution states.

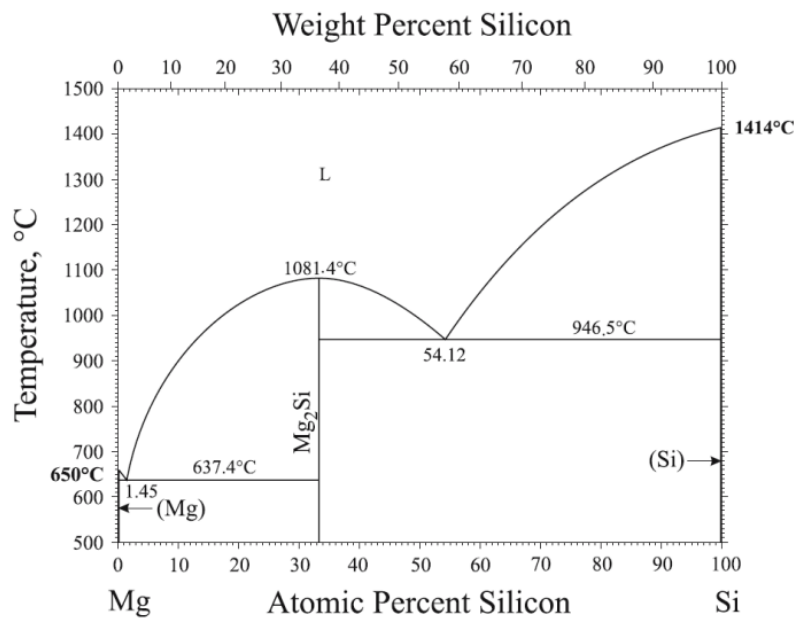


**Figure 1.3.2.** Phase diagram of Mg-Si.

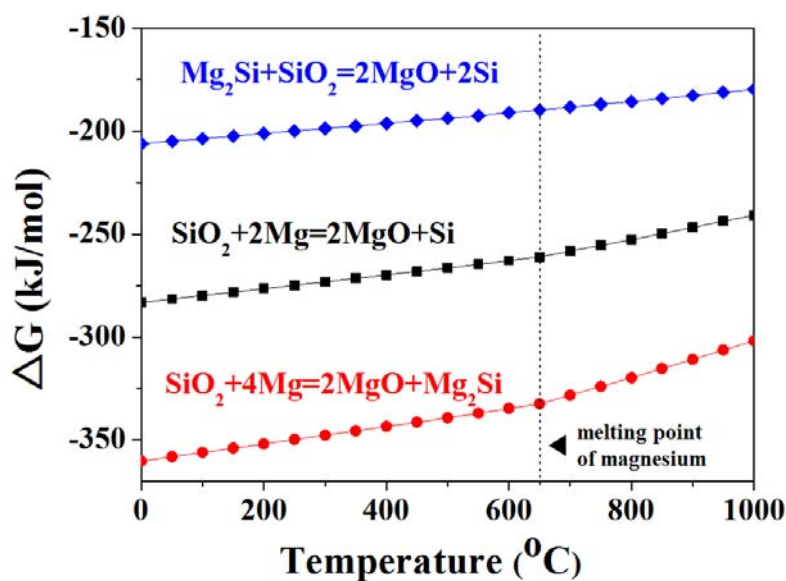
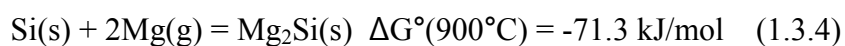


**Figure 1.3.3.** Gibbs free energy of the reactions as a function of temperature.

The  $\text{Mg}_2\text{Si}$  phase is also formed by applying excess Mg for magnesiothermic reduction:



Even though  $\text{Mg}_2\text{Si}$  phase is easily leached out at HCl solution, it is problem to form the silicon nanostructure. The  $\text{Mg}_2\text{Si}$  contained reduced Si nanostructure might be collapsed by leaching of  $\text{Mg}_2\text{Si}$ . So control of  $\text{Mg}_2\text{Si}$  is very important for synthesis of silicon nanostructure. Recently, magnesiothermic reduction has been intensive attention due to low temperature process, but the exact reaction

mechanism and effect of reduction conditions have not been well established.

The interior structure of silicon, prepared by magnesiothermic reduction, is composed of a few nano-sized silicon grains. Figure 1.3.3 shows the typical micro-structure of silicon, reduced by magnesiothermic reduction. During heating up to 650 °C, the SiO<sub>2</sub> is reduced by magnesium and the MgO is generated and the MgO is located around silicon nano-grain (Figure 1.3.3 (c)). The MgO is easily leached out by HCl treatment and the porous silicon could be obtained. The figure 1.3.2 (d)-(f) is TEM image of reduced silicon nanostructure and the MgO site became pore. This porous structure is suitable to apply for anode of Li-ion battery because the porous structures more effectively accommodate a volume expansion during lithiation and delithiation.

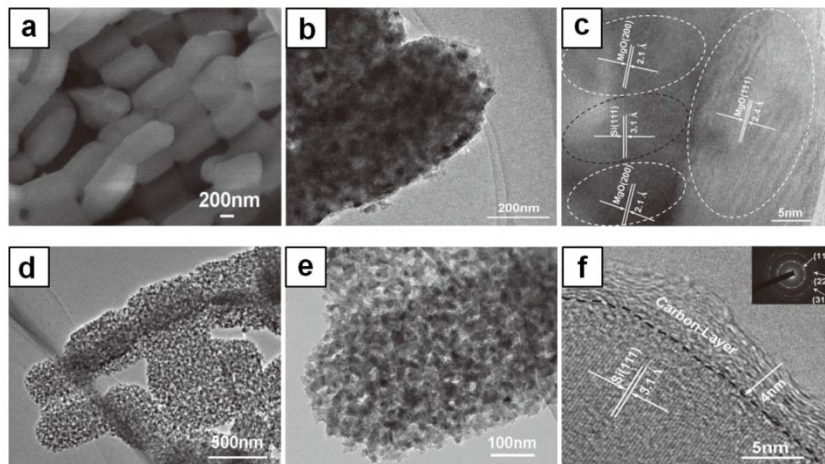


**Figure 1.3.4.** (a)-(c) as reduced Si-MgO composite, (d)-(f) Acid treated mesoporous silicon nanostructure. [37]

Currently, graphite is used as anode electrode for Li-ion battery for industry due to excellent capacity retention during the cycling. Nevertheless, graphite electrode has a low specific capacity ( $372 \text{ mAh g}^{-1}$ ) and shows a poor rate capability.[38-40] Since the demand for safe Li-ion batteries exhibiting high power, large capacity, and high rate capability is ever increasing, new electrode materials is required to replace graphite of low capacity. Most of all, silicon based systems are definitely attractive candidates since silicon has a large theoretical specific capacity at room temperature ( $\text{Li}_{15}\text{Si}_4$  :  $3600 \text{ mAh g}^{-1}$ ) and low operating voltage (around  $0.1 \text{ V}$  vs.  $\text{Li/Li}^+$ ).[41, 42] However, silicon based electrodes undergo a large volume Change during the cycling and it leads to a poor rate capability.[43,44] It is well-known that the nano-sized silicon show good cycle retention and high reversible capacity, but the synthesis of silicon nanostructure is still required the high cost technique or toxic precursor, such as  $\text{SiCl}_4$  or  $\text{SiH}_4$ . Recently, synthesis of silicon nanostructure by magnesiothermic reduction has been intensively attracted. Silicon nanostructures, such as nanoparticle, thin film (or plate), hollow sphere, and nanotube, were successfully synthesized by magnesiothermic reduction and show high electrochemical performance for Li-ion battery.[45-50]

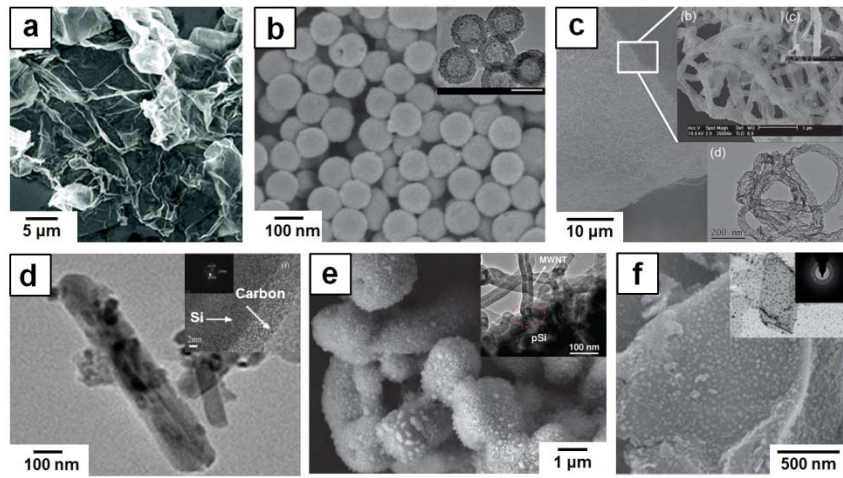


**Figure 1.3.5.** Silicon nanostructures, prepared by magnesiothermic reduction: (a) nanosheet,[45] (b) hollow sphere,[46] (c) nanotube,[47] (d) silicon-carbon composite, [48] (e) silicon-CNT composite, [49] (d) silicon-graphene composite. [50]

## 1.4. Reference

- (1) W. Stöber, A. Fink, E. J. Bohn, *Colloid Interface Sci.* 1968, 26, 62.
- (2) J. Kim, L. Kim, C. Kim, *Biomacromolecules* 2007, 8, 215.
- (3) R. S. Wagner and W. C. Ellis, VLS mechanism, *Appl. Phys. Lett.* 1964 (4), 89-91.
- (4) A. B. Greytak, L. J. Lauhon, M. S. Gudiksen, C. M. Lieber, *Appl. Phys. Lett.* 2004 (84), 4176
- (5) M. H. Huang, S. Mao, H. Feick, H. Yan, Y. Wu, H. Kind, E. Weber, R. Russo, Peidong Yang, *Science*, 2001 (8), 1897-1899.
- (6) C. K. Chan, H. Peng, G. Liu, K. McIlwrath, X. F. Zhang, R. A. Huggins, Y. Cui, *Nature Nanotechnology*, 2008 (3), 31 – 35.
- (7) L. Tsakalacos, J. Balch, J. Fronheiser, B. A. Korevaar, O. Sulima, J. Rand, *Appl. Phys. Lett.* 2007 (91) 233117.
- (8) X. Feng, K. Shankar, O. K. Varghese, . Paulose, . J. Latempa, C. A. Grimes, *Nano Lett.*, 2008, 8 (11), 3781–3786.
- (9) G. Zheng, F. Patolsky, Y. Cui, W. U. Wang, C. M. Lieber, *Nature Biotechnology* 2005 (23), 1294 – 1301.

- (10) Y. Cui, L. J. Lauhon, M. S. Gudiksen, J. Wang, C. M. Lieber, *Appl. Phys. Lett.* 2001 (78), 2214.
- (11) H. J. Choi, *Semiconductor Nanostructures for Optoelectronic Devices NanoScience and Technology* 2012, 1-36.
- (12) S.-S. Yim, M.-S. Lee, K.-S. Kim, K.-B. Kim, *Appl. Phys. Lett.* 2006 (89), 093115.
- (13) X. Duan, Y. Huang, C. M. Lieber, *Nano Lett.*, 2002(2), 487-490.
- (14) D. J. Gargas , M. E. Toimil-Molares, P. Yang, *J. Am. Chem. Soc.*, 2009, 131 (6), 2125–2127.
- (15) Xudong , Xudong , J. Zhou, Jinhui , J. Liu, N. Xu, Z. L. Wang, *Nano Lett.*, 2006 (6), 2768–2772.
- (16) Hou T. Ng, J. Han, T. Yamada, P. Nguyen, Y. P. Chen, M. Meyyappan, *Nano Letters*, 2004 (4), 1247–1252.
- (17) A. Lugstein, A. M. Steinmair, Y. J. Hyun, G. Hauer, P. Pongratz, E. Bertagnolli, *Nano Lett.* 2008 (8), 2310-2314.
- (18) H. Jagannathan, M. Deal, Y. Nishi, J. Woodruff, C. Chidsey, P. C. McIntyre, J. *Appl. Phys.* 2006 (100), 024318.
- (19) K. Tomioka, J. Motohisa, S. Hara, T. Fukui, *Nano Lett.* 2008, 8, 3475-3480.
- (20) S.-G. Ihn, J.-I. Song, T.-W. Kim, D.-S. Leem, T. Lee, T. S.-G. Lee, E. K. Koh, K. Song, K. *Nano Lett.* **2007**, 7, 39-44.

- (21) P. Nguyen, H. T. Ng, T. Yamada, M. K. Li, J. Smith, J. Han, M. Meyyappan, *Nano Lett.* **2004** (4) 651-657.
- (22) K.-W. Chang, J.-J. Wu, *Adv. Mater.* **2004**(16), 545-549.
- (23) Q. Wan, M. Wei, D. Zhi, J. L. MacManus-Driscoll, M. G. Blamire, *Adv. Mater.* **2006**(18) 234-238.
- (24) D. Whang, S. Jin and C. M. Lieber, *Nano Lett.*, 2003, 3, 951.
- (25) P. A. Smith, C. D. Nordquist, T. N. Jackson, T. S. Mayer, B. R. Martin, J. Mbindyo, T. E. Mallouk, *Appl. Phys. Lett.*, 2000, 77, 1399.
- (26) Y. Huang, X. F. Duan, Q. Q. Wei and C. M. Lieber, *Science*, 2001(291) 630.
- (27) S. Myung, M. Lee, G. T. Kim, J. S. Ha and S. Hong, *Adv. Mater.*, 2005, 17, 2361.
- (28) A. Javey, S. Nam, R. S. Friedman, H. Yan and C. M. Lieber, *Nano Lett.*, 2007, 7, 773.
- (29) D. Tsivion, M. Schwartzman, R. Popovitz-Biro, P. v. Huth, E. Joselevich, *Science*, 2011 (333), 1003.
- (30) C. L. Hsin, J. H. He, C. Y. Lee, W. W. Wu, P. H. Yeh, L. J. Chen, Z. L. Wang, *Nano Lett.*, 2007 ( 7), 1799-1803.
- (31) S. A. Fortuna, J. Wen, I. S. Chun, X. Li, *Nano Lett.*, 2008 ( 8), 4421-4427
- (32) Y. Yoo, I. Yoon, H. Lee, J. Ahn, J.-P. Ahn, B. Kim, *ACS nano*, 2010(4),

- 2919-2927.
- (33) B. Nikoobakht, C. A. Michaels, S. J. Stranicka, M. D. Vaudin, *Appl. Phys. Lett.*, 2004 (85), 3244.
- (34) E.H. Myrhaug, J.K. Tuset, H. Tveit, 2004, *Proceedings: Tenth International Ferroalloys Congress, 2004*, 1-4.
- (35) D. Lynch, *JOM*, 2009, 61 (11), 41-48.
- (36) Z. Bao, M. R. Weatherspoon, S. Shian, Y. Cai, P. D. Graham, S. M. Allan, G. Ahmad, M. B. Dickerson, B. C. Church, Z. Kang, H. W. Abernathy, C. J. Summers, M. Liu, Ke. H. Sandhage, *Nature* 2007 (446), 172-175,
- (37) H. Jia, P. Gao, J. Yang, J. Wang, Y. Nuli, Z. Yang, *Adv. Energy Mater.*, 2011, 1, 1036–1039.
- (38) J. R. Dahn, T. Zheng, Y. Liu, J. S. Xue, *Science* **270** (1995) 590.
- (39) M. Winter, J. O. Besenhard, M. E. Spahr, P. Novak, *Adv. Mater.* **10** (1998) 725.
- (40) X. Y. Song, K. Kinoshita, *J. Electrochem. Soc.* **145** (1996) L120.
- (41) M. N. Obrovac, L. Christensen, *Electrochem. Solid State Lett.*, 2004, 7, A93.
- (42) J. Li, J. R. Dahn, *J. Electrochem. Soc.* **154** (2007) A156.
- (43) C. M. Park, K. H. Kim, H. Kim, H.-J. Sohn, *Chem. Soc. Rev.* **39** (2010) 3115.
- (44) G. Jung, Y. U. Kim, H. Kim, Y. J. Kim, H.-J. Sohn, *Energy Environ. Sci.* **4** (2011) 1986.

- (45) Z. Lu, J. Zhu, D. Sim, W. Zhou, W. Shi, H. H. Hng, Q. Yan, *Chem. Mater.*, 2011, 23, 5293-5295.
- (46) D. Chen, X. Mei, G. Ji, M. Lu, J. Xie, J. Lu, J. Y. Lee, *Angew. Chem.*, 2012, 124, 1-6.
- (47) J.-K. Yoo, J. Kim, Y. S. Jung, K. Kang, *Adv. Mater.*, 2012, 24, 5452-5456.
- (48) H.-C. Tao, L.-Z. Fan, X. Qu, *Electrochimica Acta*, 2012, 71, 194-200.
- (49) P. Gao, H. Jia, J. Yang, Y. Nuli, J. Wang, J. Chen, *Phys. Chem. Chem. Phys.*, 2011, 13, 20108–20111.
- (50) X. Xin, X. Zhou, F. Wang, X. Yao, X. Xu, Y. Zhu, Z. Liu, *J. Mater. Chem.*, 2012, **22**, 7724-7730.

## **Chapter 2.**

### **Synthesis of Zero-dimensional SnO<sub>2</sub> Nanostructures for Li-ion Battery**

## **2.1. Synthesis of SnO<sub>2</sub> hollow sphere with size-control for Li-ion battery application**

### **2.1.1. Introduction**

The demand for high energy and power density lithium ion batteries (LIBs) has increased in hybrid electric vehicles (HEVs) as well as light-weight and portable electronic devices.[1-3] In commercial LIBs, graphite-based materials are widely used as an anode, but the theoretical capacity is only 372 mAhg<sup>-1</sup>. [4] Therefore, intensive researches have been focused on the high capacity electrode materials such as Si, Ge, Sn, and SnO<sub>2</sub>. [5-7] Among various candidates, SnO<sub>2</sub> has been attracted as a promising anode material due to its high capacity and low reactivity with electrolyte. [8,9] However, a large and uneven volume change, about 300 %, occurs upon lithium insertion/extraction, which causes a pulverization and electrical connectivity loss. As a result, SnO<sub>2</sub> electrode shows a fast capacity fading.

To relieve this problem, various nanostructures have been applied to LIB anode including nanoparticles, [10,11] nanotubes, [12,13] nanowires, [14-17] and porous structure. [18-20] Among them, hollow spheres are the most promising structure for anode electrode of LIBs due to a low density, high surface to volume

ratio, structural stability, etc.[21-23] Recently, the electrochemical properties of SnO<sub>2</sub>-based hollow structures have been intensively investigated, and these structures showed the enhanced cycling performance compared to the solid SnO<sub>2</sub> nanoparticles.[24-31] However, most of studies have been focused on the fabrication of the unique nanostructures, and their size was limited to 100~200 nm. The size of hollow spheres appears to be a crucial factor, but the synthesis of size controlled hollow sphere and the size dependence of the electrochemical properties have not been explored.

In this study, the size effect of SnO<sub>2</sub> hollow spheres is investigated for LIB anode application. The nano-sized SnO<sub>2</sub> hollow spheres are fabricated by SiO<sub>2</sub> template-based synthesis and the size of the hollow spheres is controlled by using different-sized templates.

### **2.1.2. Experimental procedure**

*1) Preparation of SiO<sub>2</sub> Colloids:* SiO<sub>2</sub> colloids with different sizes were prepared by the modified Stöbber method. The size of silica nanoparticles was controlled by varying the amount of catalysts (28% ammonium hydroxide). The contents of reactants, solvent, catalyst, and pH value are shown in Table 2.1.1. For the synthesis, 75 mL methanol, 10 mL deionized water, and required amount of ammonium hydroxide were first mixed, and then, 2 mL of tetraethylorthosilicate

(TEOS, 98+%, Sigma Aldrich) was added. The reaction was conducted at room temperature for 2 h. After that, the prepared SiO<sub>2</sub> colloid solution was dried with adding water, repeatedly, until pH reached about 8. The final volume of each SiO<sub>2</sub> colloid solution was 50 mL .

**Table 2.1.1.** Experimental conditions for synthesis of SiO<sub>2</sub> colloids.

Solvent	NH <sub>3</sub> ·H <sub>2</sub> O	pH	TEOS	Size of SiO <sub>2</sub>
10 mL D.I. Water	2.7 mL	11.41	2 mL	~ 15 nm
+ 75 mL , Methanol	4.5 mL	11.56	2 mL	~ 36 nm
	8 mL	11.75	2 mL	~ 92 nm

**2) Synthesis of SnO<sub>2</sub> Hollow Spheres:** The SnO<sub>2</sub> hollow spheres were prepared by using SiO<sub>2</sub> colloid solution. In a typical experiment (25 nm SnO<sub>2</sub> hollow sphere), 0.8 g of potassium stannate trihydrate (K<sub>2</sub>SnO<sub>3</sub>·3H<sub>2</sub>O, Sigma Aldrich,) was dissolved into 45 mL deionized water and 5 mL of prepared SiO<sub>2</sub> colloid solution was added. And then, 25 mL of absolute ethanol was added into above solution. The solution was heated to 60 °C for 1 h with a mild stirring. The white product was collected by centrifuge and washed with deionized water three times, dried at 100 °C, and annealed at 600 °C for 1 h. The annealed powder was treated with 2 M NaOH solution at 50 °C for 1 h. After that, the SnO<sub>2</sub> hollow sphere was obtained.

**Table 2.1.2.** Experimental condition for SnO<sub>2</sub> coating process

SiO <sub>2</sub> template	SiO <sub>2</sub> colloid	Solvent (D.I. water / Ethanol)	K <sub>2</sub> SnO <sub>3</sub> ·3H <sub>2</sub> O	pH	NaOH treatment
15 nm	5 mL		0.8 g	12.5	90 °C for 1 h
36 nm	5 mL	45 mL / 25 mL	0.5 g	12.38	90 °C for 2 h
92 nm	5 mL		0.35 g	12.21	90 °C for 8 h

**Electrochemical Test:** For electrochemical measurements, the test electrodes consisted of active powder material (0.2 g), carbon black (Ketchen Black, 0.06 g) as a conducting agent and poly amide imide (PAI, 0.029 g) dissolved in N-methyl pyrrolidinone (NMP) at 60 °C as a binder. Each component was well mixed to form a slurry using a magnetic stirrer. The slurry was coated on a copper foil substrate, pressed, and dried at 200 °C for 4 h under a vacuum. A coin-type electrochemical cell was used with Li foil as the counter and reference electrodes, and 1 M LiPF<sub>6</sub> in ethylene carbonate (EC)/diethylene carbonate (DEC) (5:5 (v/v), PANAX) was used as the electrolyte. The amount of active material loading on each copper foil was 1 mg and the mass of Li foil was 70 mg. The cell assembly and all electrochemical tests were carried out in an Ar-filled glove box. The cycling experiments were galvanostatically performed using a Maccor automated tester at a constant current density of 100 mA g<sup>-1</sup> for the active material within a voltage range between 0.0 and 2.5 V (vs. Li/Li<sup>+</sup>). The rate capability test was

conducted in the following sequence of current density: 100, 300, 500, 1000, 1500, and 100 mA g<sup>-1</sup>. For reference, commercial SnO<sub>2</sub> nanopowder (<100 nm, Sigma Aldrich) was also examined.

### **2.1.3. Results and discussion**

#### *Synthesis of nano-sized SnO<sub>2</sub> hollow sphere*

The low magnification TEM image (Figure 2.1.1(a)) reveals the core-shell structure with bright center (SiO<sub>2</sub> template) and dark shell (SnO<sub>2</sub> layer). The shell thickness is quite uniform. The SnO<sub>2</sub> layer is almost amorphous, but nanocrystallites are occasionally observed (Figure 2.1.1(b)). After annealing at 600 °C and removing SiO<sub>2</sub> in NaOH, the SnO<sub>2</sub> hollow structure is maintained (Figure 2.1.1(c)). The average size of the SnO<sub>2</sub> hollow sphere was about 25 nm and the individual hollow sphere was agglomerated. The high magnification TEM image reveals that the hollow spheres are composed of interconnected nanocrystallites of ~3 nm size (Figure 2.1.1(d)). The lattice fringes are clearly discerned and the interplanar spacings are determined to be 0.335 and 0.264 nm, which are in good agreement with the (110) and (101) planes of SnO<sub>2</sub>, respectively. The shell thickness was less than 5 nm, which indicates that the hollow sphere shell consists of a maximum of one or two nanocrystallites. The selected area electron diffraction (SAED) patterns of SiO<sub>2</sub>-SnO<sub>2</sub> core-shells

(upper) and SnO<sub>2</sub> hollow spheres (bottom) are shown in Figure 2.1.1(e). In SiO<sub>2</sub>-SnO<sub>2</sub> core-shells, a clear diffraction pattern is not observed, whereas the ring patterns are evident in the SnO<sub>2</sub> hollow spheres, which are completely indexed to rutile SnO<sub>2</sub>. The crystal structure of the samples is further investigated by X-ray diffraction (XRD) (Figure 2.1.1(f)). The diffraction peaks for as-coated SiO<sub>2</sub>-SnO<sub>2</sub> core-shells are broad with a very weak intensity because the SnO<sub>2</sub> shells are not completely crystallized during the coating process. After annealing at 600 °C and removing SiO<sub>2</sub>, the SnO<sub>2</sub> hollow spheres are crystallized into a single phase rutile SnO<sub>2</sub>. All the peaks are broadened due to the nanocrystalline nature of the SnO<sub>2</sub> particles. This result agrees well with the TEM image. To determine the specific surface area, Brunauer-Emmett-Teller (BET) nitrogen absorption/desorption analysis is performed. The BET surface area of annealed SiO<sub>2</sub>-SnO<sub>2</sub> core-shells is 41.0 m<sup>2</sup> g<sup>-1</sup> and that of SnO<sub>2</sub> hollow spheres is around 117.9 m<sup>2</sup> g<sup>-1</sup>. This increase is attributed to the hollow nature and nanoporous shell.

The synthesis temperature of the SnO<sub>2</sub> shell layer is varied from 40 to 100 °C, but no specific morphology change is observed (Figure 2.1.2). Hydrothermal method is commonly employed for SnO<sub>2</sub> coating, which requires a relatively high temperature (> 160 °C) and a long processing time.[31] The Sn precursor (K<sub>2</sub>SnO<sub>3</sub>·3H<sub>2</sub>O) and solvent (ethanol-water) adopted in this study are similar to those used in the hydrothermal process, but the nanosized SnO<sub>2</sub> coating is

successfully synthesized at a low temperature for a short time.

The size of the hollow spheres is simply controlled by using different-sized templates, and the shell thickness is fixed at about 5 nm (Figure 2.1.3). The larger sized SnO<sub>2</sub> hollow spheres require a small amount of SnO<sub>2</sub> precursor to achieve the constant shell thickness due to the decrease of surface area, i.e. the amount of K<sub>2</sub>SnO<sub>3</sub>·3H<sub>2</sub>O is reduced. Three kinds of hollow SnO<sub>2</sub> spheres are fabricated in this study, and their average sizes are 25, 54, and 103 nm. Irrespective of the size, the hollow spheres are composed of interconnected nanoparticles of about 3 nm, and the SAED patterns confirmed the formation of rutile SnO<sub>2</sub>. For convenience, each sample is named the 25, 50, and 100 nm-sized SnO<sub>2</sub> hollow spheres.

The discharge/charge voltage profile of the 25 nm sized SnO<sub>2</sub> hollow sphere electrode is shown in Figure 2.1.4(a), and the shape of the voltage profile is similar to that of the typical SnO<sub>2</sub>. [13, 24, 29] The initial discharge and charge capacities are 2105 and 1029 mAh g<sup>-1</sup>, respectively, which are higher than the theoretical value. The high discharge capacity is explained by formation of Li<sub>2</sub>O and SEI, and additional reaction from conducting agent. In case of charge procedure, the reversible polymerization of electrolytes might be affected to the high discharge capacity. [37, 38] The SnO<sub>2</sub> hollow spheres of the other sizes show

similar voltage profiles (Figure 2.1.5). The low 1st cycle efficiency (about 48.9 %) might be caused by the irreversible reduction of SnO<sub>2</sub> to Sn and the formation of Li<sub>2</sub>O and solid electrolyte interphase on the surface of the active material,[8] which is expected to be improved by the addition of conducting materials (CNT, graphene) or transition metal oxides.[39,40] The rate capability test of the SnO<sub>2</sub> (25 nm) electrode (Figure 2.1.4(b)) shows that the reversible capacity at a current density of 200 mA g<sup>-1</sup> is about 700 mAh g<sup>-1</sup> and it is about 530 mAh g<sup>-1</sup> at 500 mA g<sup>-1</sup>. This good rate capability is due to the nano-sized SnO<sub>2</sub> hollow sphere and thin shell thickness. To demonstrate the size effects, the cyclability of each hollow SnO<sub>2</sub> is compared at a current density of 100 mA g<sup>-1</sup> (Figure 2.1.4(c)). All samples show good cyclability, but the reversible capacity of each electrode differs. The capacity is strongly dependent on the hollow size and increases with a decrease in the size of the hollow sphere. The capacity of the 100 nm sized SnO<sub>2</sub> hollow sphere is 547 mAh g<sup>-1</sup> after 50 cycles, which is close to the previous result.[24] As the size of the SnO<sub>2</sub> hollow spheres is reduced, the electrodes show higher reversible capacities. The reversible capacity of the SnO<sub>2</sub> (25 nm) electrode is about 750 mAh g<sup>-1</sup> after 50 cycles and this value is close to the theoretical capacity of SnO<sub>2</sub>. To investigate the effect of the hollow structure on the electrochemical properties, the result of cycle test for the commercial SnO<sub>2</sub> nanopowder (9.55 m<sup>2</sup> g<sup>-1</sup> of BET surface area) is included. The SnO<sub>2</sub> hollow sphere electrode shows better electrochemical properties than the SnO<sub>2</sub>

nanopowder electrode. The cyclic capacity of the nanopowder continuously decreased, and the capacity was only 250 mAh g<sup>-1</sup> after 50 cycles. After 50 cycles, the reversible capacity of the SnO<sub>2</sub> nanopowder is only 33 % of the theoretical value. It is reported that the nanocrystalline CdS in spherical shell geometry is capable of withstanding extreme stresses,[41] and the maximum tensile stress in a hollow Si sphere is ~5 times lower than that in a solid sphere with an equal volume of Si during lithiation.[21] The larger size SnO<sub>2</sub> hollow sphere is more fragile and it is inferred that the smaller sized hollow sphere is mechanically strong and more effectively endures the large volume change without a pulverization of electrical pathways.

To confirm the retention of the hollow structure after cycling, the TEM and SEM analyses are conducted on the SnO<sub>2</sub> hollow spheres (Figure 2.1.6). Compared to the pristine SnO<sub>2</sub> hollow spheres, some deformation (from a circular to an elliptical shape) is observed, but the entire hollow structure is maintained and each hollow sphere is interconnected. The HRTEM image indicates that the shells are composed of nanocrystallites and the shell thickness slightly increases, but a severe grain growth or agglomeration is not observed. The drastic grain growth of SnO<sub>2</sub> or Sn-based material during charge/discharge is the main reason for poor cycle retention, but the current observation indicates that the grain growth is noticeably restricted. Thus, we infer that the hollow nature of the SnO<sub>2</sub>

with nano-sized crystallites effectively reduces the grain growth, which results in a high reversible capacity and good cycle retention.

#### **2.1.4. Conclusion**

In summary, a robust and simple process to fabricate the nano-sized SnO<sub>2</sub> hollow spheres is suggested. The size of SnO<sub>2</sub> hollow spheres is varied from 25 to 100 nm with a constant shell thickness of ~5 nm. Moreover, the size effect of the hollow spheres on the electrochemical properties is demonstrated. The hollow spheres show the stable cycling performance, and the capacity dramatically increases with decreasing the size. The capacity of the smallest SnO<sub>2</sub> hollow sphere is about 750 mAh g<sup>-1</sup> after 50 cycles and this value approaches the theoretical value of SnO<sub>2</sub>. Therefore, it can be concluded that the nano-sized hollow sphere is an ideal structure for the anode material.

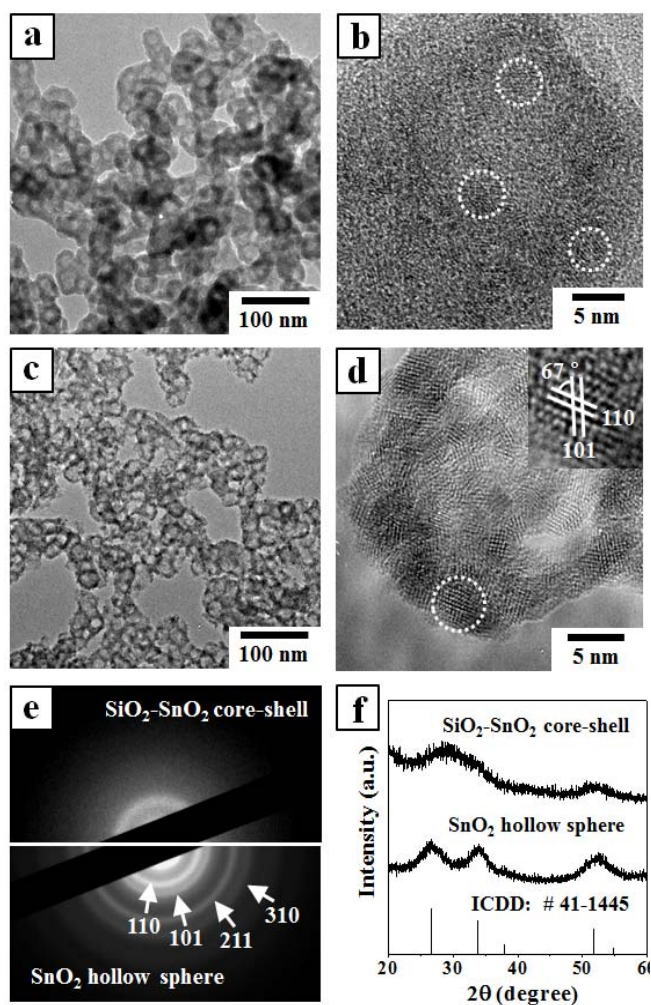


**Figure 2.1.1.** (a, b) Low and high magnification TEM images of as-coated SiO<sub>2</sub>-SnO<sub>2</sub> core-shells; (c, d) 25 nm sized SnO<sub>2</sub> hollow spheres after annealing and removal of SiO<sub>2</sub>; (e) SAED patterns of as-coated SiO<sub>2</sub>-SnO<sub>2</sub> core-shells (upper) and SnO<sub>2</sub> hollow spheres (bottom); (f) XRD patterns of SiO<sub>2</sub>-SnO<sub>2</sub> core-shells and SnO<sub>2</sub> hollow spheres.

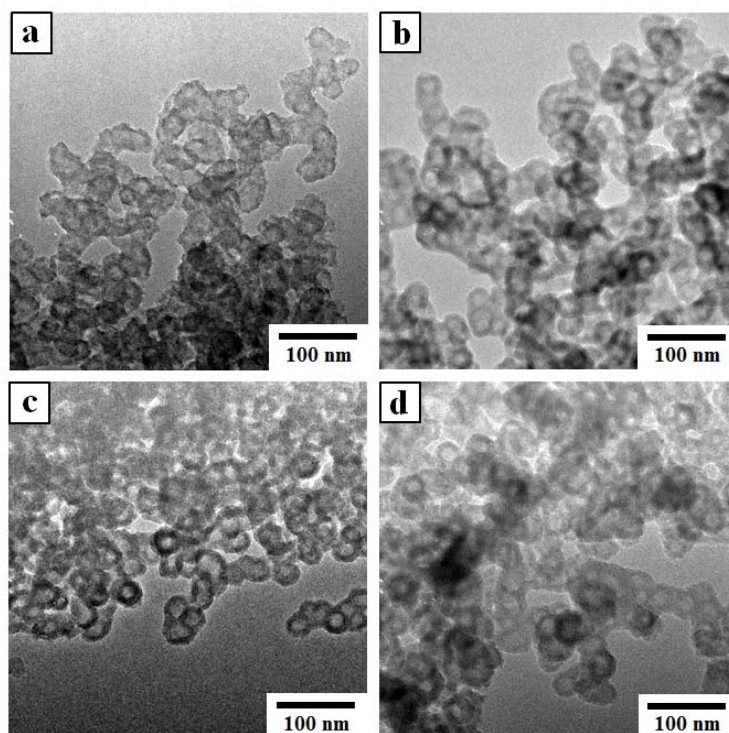


**Figure 2.1.2.** As prepared  $\text{SiO}_2\text{-SnO}_2$  core-shells at different synthesis temperature: (a) 40, (b) 60, (c) 80, and (d) 100 °C.

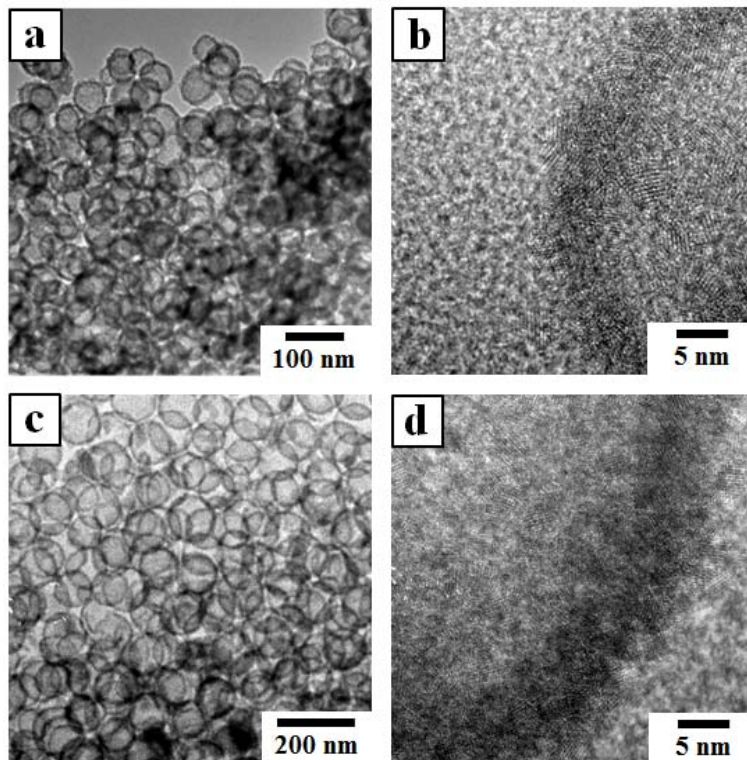


**Figure 2.1.3.** TEM and HRTEM images of size controlled SnO<sub>2</sub> hollow sphere: (a, b) 50 nm; (c, d) 100 nm.

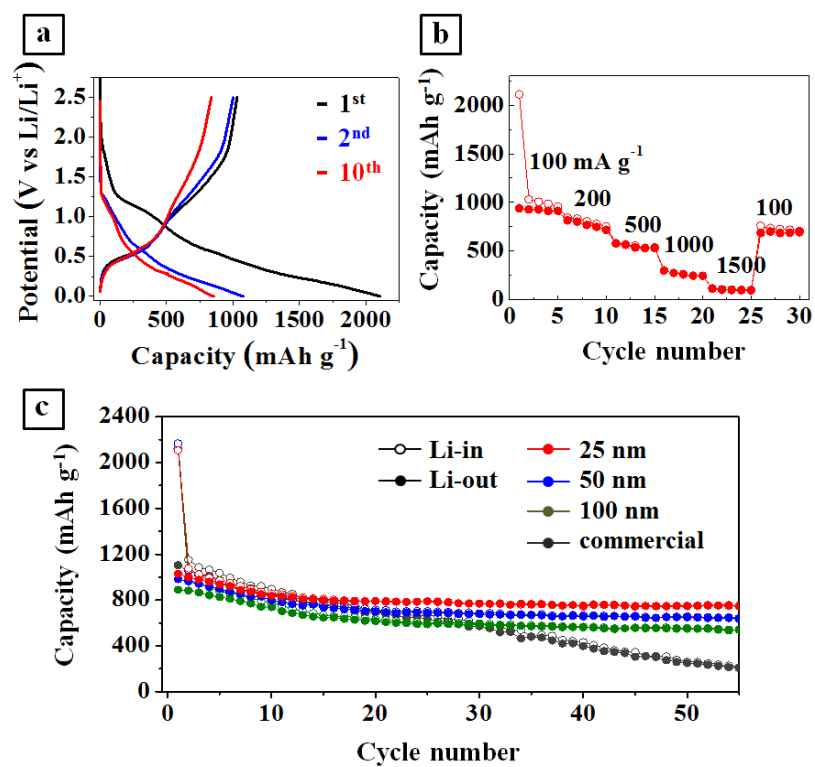


**Figure 2.1.4.** (a) Charge/discharge voltage profile of 25 nm sized SnO<sub>2</sub> hollow sphere between 0.01 and 2.5 V at 100 mA g<sup>-1</sup>; (b) rate capability test of 25 nm sized SnO<sub>2</sub> hollow sphere; (c) cyclability of SnO<sub>2</sub> hollow spheres with different size and commercial SnO<sub>2</sub> nanopowder at 100 mAh g<sup>-1</sup>.

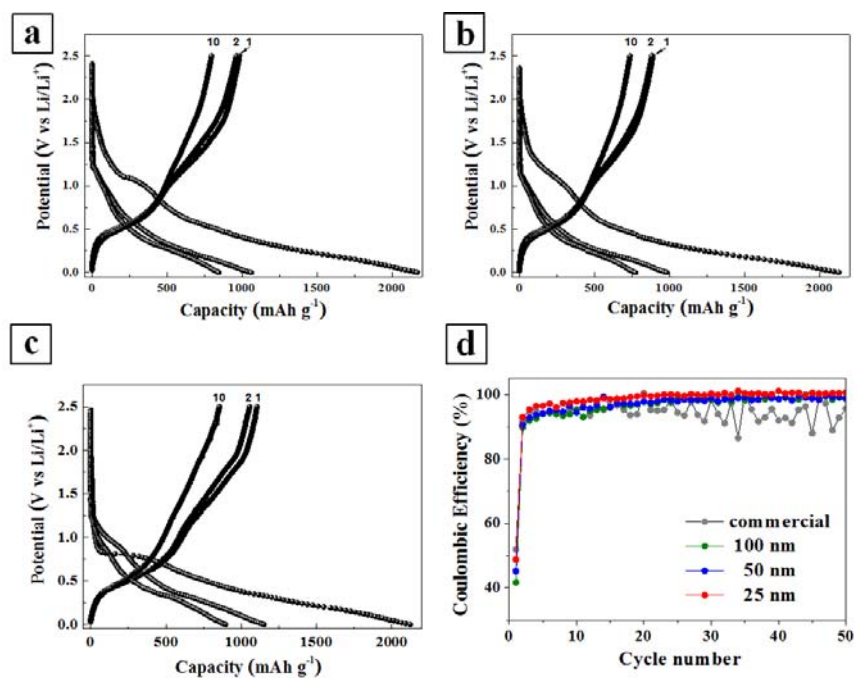


**Figure 2.1.5.** Charge/discharge voltage profiles of SnO<sub>2</sub> hollow spheres between 0.0 and 2.5 V at 100 mAh g<sup>-1</sup> : (a) 50 nm, (b) 100 nm, and (c) commercial SnO<sub>2</sub> nanopowder, (d) columbic efficiency.

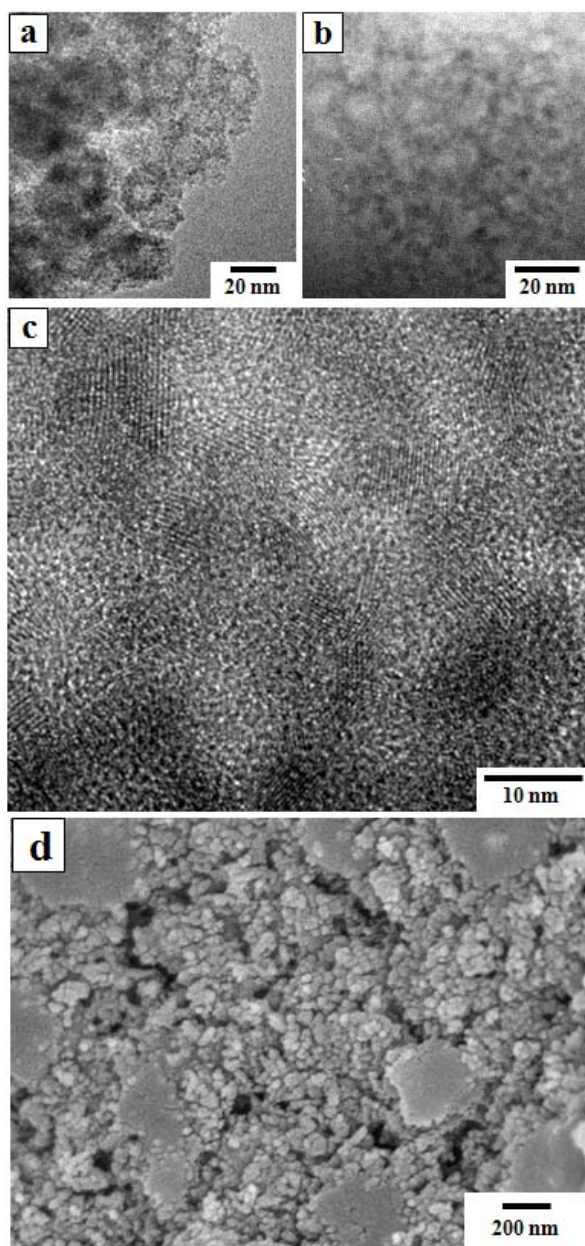


**Figure 2.1.6.** TEM images of SnO<sub>2</sub> electrode: a) pristine and b) after 20 cycles; c) HRTEM image of b). d) SEM images of SnO<sub>2</sub> hollow sphere after 50 cycles.

## **2.2. Transition metal oxide coated SnO<sub>2</sub> hollow sphere and their extraordinary electrochemical properties**

### **2.2.1. Introduction**

Recently, various hetero-structured metal oxides, such as core-shell, branch and hierarchical structure, have been intensively applied to anode electrode of Li-ion battery. Among various hetero-structures, one of noble strategy is a formation of composite between transition metal oxide and SnO<sub>2</sub>. The strategy of structural design in this works is follow: SnO<sub>2</sub> hollow sphere is applied to a core material for SnO<sub>2</sub>-Co<sub>3</sub>O<sub>4</sub> composite structure. The hollow sphere shows the good cyclability and rate capability because hollow nature could accommodate the large volume expansion without a pulverization of electrical pathway and the short diffusion path of Li<sup>+</sup> within thin-shell layer is significant advantage for an enhanced rate capability. And, the transition metal oxide (Co<sub>3</sub>O<sub>4</sub>) is formed as outer layer, because the presence of Co nanoparticle leads a polymer/gel-like film, of 150 mAh g<sup>-1</sup> capacity, on the surface of electrode.[42] Moreover, the Co nanoparticle, located at the interface between SnO<sub>2</sub> and Co<sub>3</sub>O<sub>4</sub>, might increase the reversibility of the reduction reaction of Li<sub>2</sub>O.[43] So, additional reversible capacity could be induced by structural design of composite nanostructure. Based on the strategy, the synthesized SnO<sub>2</sub>@Co<sub>3</sub>O<sub>4</sub> hollow sphere

showed impressive electrochemical performances with extraordinary reversible capacity ( $1083 \text{ mAh g}^{-1}$  after 50 cycles at  $100 \text{ mA g}^{-1}$ ), good cyclability, and high rate capability.

### **2.2.2. Experimental procedure**

***Cobalt oxide coating on SnO<sub>2</sub> hollow sphere:*** 0.1 g of SnO<sub>2</sub> hollow sphere was dispersed in D. I. water and 0.18g Co(NO<sub>3</sub>)<sub>2</sub>·6H<sub>2</sub>O, 1 g of PVP (Polyvinylpyrrolidone), 2.4 g of urea was added. And then, the solution was heated at 80 °C for 10 h with mild stirring.

***Electrochemical Test:*** For electrochemical measurements, the test electrodes consisted of active powder material (0.2 g), carbon black (Ketchen Black, 0.06 g) as a conducting agent and poly amide imide (PAI, 0.029 g) dissolved in N-methyl pyrrolidinone (NMP) at 60 °C as a binder. Each component was well mixed to form a slurry using a magnetic stirrer. The slurry was coated on a copper foil substrate, pressed, and dried at 200 °C for 4 h under a vacuum. A coin-type electrochemical cell was used with Li foil as the counter and reference electrodes, and 1 M LiPF<sub>6</sub> in ethylene carbonate (EC)/diethylene carbonate (DEC) (5:5 (v/v), PANAX) was used as the electrolyte. The amount of active material loading on each copper foil was 1 mg and the mass of Li foil was 70 mg. The cell assembly

and all electrochemical tests were carried out in an Ar-filled glove box. The cycling experiments were galvanostatically performed using a Maccor automated tester at a constant current density of  $100 \text{ mA g}^{-1}$  for the active material within a voltage range between 0.0 and 2.5 V (vs. Li/Li+). The rate capability test was conducted in the following sequence of current density: 100, 300, 500, 1000, 1500, and  $100 \text{ mA g}^{-1}$ . For reference, commercial  $\text{SnO}_2$  nanopowder (<100 nm, Sigma Aldrich) was also examined.

### **2.2.3. Results and discussion**

#### ***Synthesis of $\text{SnO}_2@Co_3O_4$ hollow sphere***

For the coating of Cobalt oxide, urea was used as catalyst for hydrolysis of  $\text{Co}(\text{OH})_2$ . Generally, sodium hydroxide (NaOH), sodium acetate (NaAc), ammonia ( $\text{NH}_3 \cdot \text{H}_2\text{O}$ ) has been used for synthesis of metal hydroxide nanostructure.[44-46] However, these catalyst leads to fast hydrolysis for metal hydroxide, so metal hydroxide nanostructure is formed by homogeneous nucleation. In contrast, urea is slowly decomposed and hydrolysis of metal is occurred with follow reactions, so control of heterogeneous nucleation (coating) is relatively favorable.[47-49]

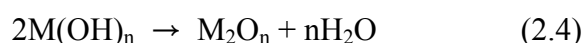
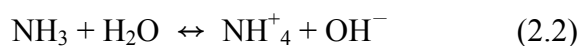


Figure 2.2.1(a) and (b) show a field-emission scanning electron microscopy (FE-SEM) image of SnO<sub>2</sub> hollow sphere and SnO<sub>2</sub>@cobalt oxide hollow sphere. SnO<sub>2</sub> hollow sphere has quietly uniform size and the size of hollow sphere is not severely changed after cobalt oxide coating but the surface morphology of SnO<sub>2</sub>@ cobalt oxide hollow sphere became rough than that of SnO<sub>2</sub> hollow sphere.

The crystal structures of the hollow spheres were investigated by X-ray diffraction (XRD) (Figure 2.2.2). The diffraction peaks for SnO<sub>2</sub> hollow sphere are crystallized into a single phase rutile SnO<sub>2</sub> (ICDD # 41-1445). All the peaks are broadened due to the nanocrystalline nature of SnO<sub>2</sub> particles. However, the any peak of Co oxide, such as CoO or Co<sub>3</sub>O<sub>4</sub>, is not observed and SnO<sub>2</sub> peaks became weak and broad in SnO<sub>2</sub>@Coblat oxide multi-layered hollow sphere,. To reveal oxidation status of Co-oxide shell layer, the XPS analysis was conducted

(Figure 2.2.2(b)). The binding energies obtained in the XPS analysis were corrected for specimen charging by referencing the C 1s peak to 284.60 eV. The 2p XPS spectra show two major peaks with binding energy values at 780.5 and 796.2 eV, corresponding to the Co 2p<sub>3/2</sub> and Co 2p<sub>1/2</sub> spin-orbit peaks, respectively. These results are well-matched to the binding energy of Co<sub>3</sub>O<sub>4</sub>. [49, 50]

Figure 2.2.3 show the TEM image of SnO<sub>2</sub> hollow sphere and SnO<sub>2</sub>@Co<sub>3</sub>O<sub>4</sub> hollow sphere. The low magnification TEM image reveals SnO<sub>2</sub>@Co<sub>3</sub>O<sub>4</sub> hollow sphere with bright center (cavity) and dark shell (SnO<sub>2</sub>@Co<sub>3</sub>O<sub>4</sub> layer). The average size of SnO<sub>2</sub>@Co<sub>3</sub>O<sub>4</sub> hollow sphere is about 50 nm with wall thickness of less than 10 nm. The wall thickness of SnO<sub>2</sub>@Co<sub>3</sub>O<sub>4</sub> hollow sphere is not noticeably different from SnO<sub>2</sub> hollow sphere and severe grain growth of Co<sub>3</sub>O<sub>4</sub> is not observed after annealing. [51, 52]

To confirm the layered cobalt oxide on SnO<sub>2</sub> hollow sphere, SnO<sub>2</sub>@Co<sub>3</sub>O<sub>4</sub> hollow sphere was investigated by scanning transmission electron microscope (STEM) and Energy dispersive x-ray spectroscopy (EDS). Sn element is almost corresponded STEM image and Co element is uniformly dispersed on SnO<sub>2</sub> hollow sphere, even though cobalt oxide phase is not detected in the XRD and TEM analysis (Figure 2.2.4). A STEM-EDS line scan through the center of

hollow sphere demonstrates that Sn and Co are present over the entire region, and the line profiles indicate the hollow nature (Figure 2.2.4(e)). Moreover, Sn and Co almost overlap, so Co shell layer is not distinguished from inner SnO<sub>2</sub> hollow structure. This profile means small amount Co is coated as very thin layer or particle liked structure. It might be the reason that X-ray and electron diffraction of cobalt oxide are not observed from SnO<sub>2</sub>@Co<sub>3</sub>O<sub>4</sub> hollow sphere.

### ***Electrochemical Properties***

Figure 2.2.5 shows the results of electrochemical cell tests for SnO<sub>2</sub> hollow sphere and SnO<sub>2</sub>@Co<sub>3</sub>O<sub>4</sub> hollow sphere electrode. The discharge/charge voltage profile of the two electrodes are shown in Figure 2.2.5(a) and (b), the initial discharge and charge capacities of SnO<sub>2</sub> hollow sphere are 2167 and 981 mAh g<sup>-1</sup>, respectively. And the low 1st cycle efficiency, about 45.3 %, might be caused by irreversible reduction of SnO<sub>2</sub> to Sn and formation of Li<sub>2</sub>O and solid electrolyte interphase on the surface of active material. In case of SnO<sub>2</sub>@Co<sub>3</sub>O<sub>4</sub> hollow sphere electrode, the initial discharge and charge capacities of SnO<sub>2</sub> hollow sphere are 2208 and 1280 mAh g<sup>-1</sup>, and the 1st cycle efficiency, 58%, is higher than that of SnO<sub>2</sub> hollow sphere. The both electrodes show the good rate capability, as shown in Figure 2.2.5(c) and (d). Especially, the SnO<sub>2</sub>@Co<sub>3</sub>O<sub>4</sub> hollow sphere electrode show higher reversible capacity than SnO<sub>2</sub> hollow sphere electrode at all current density. The reversible capacity at rates of 200, 300, 500,

900 mA g<sup>-1</sup> is about 982, 907, 822, 746 mAh g<sup>-1</sup>, respectively, and finally back to 961 mAh g<sup>-1</sup> at 100 mA g<sup>-1</sup>. The short diffusion path of Li<sup>+</sup> within thin-shell layer is significant advantage to get an enhanced rate capability at even higher rates. The extraordinary reversible capacity of SnO<sub>2</sub>@Co<sub>3</sub>O<sub>4</sub> hollow sphere electrode could not be explained with traditional theory of mixture electrode. According to traditional theory, the theoretical capacity of SnO<sub>2</sub> and Co<sub>3</sub>O<sub>4</sub> is 782 and 890 mAh g<sup>-1</sup>, respectively, so the reversible capacity of SnO<sub>2</sub>@Co<sub>3</sub>O<sub>4</sub> hollow sphere electrode could not be over the theoretical capacity of Co<sub>3</sub>O<sub>4</sub>. Recently, Xue et al reported that the extra reaction is occurred in the SnO<sub>2</sub>-MoO<sub>3</sub> system. From this study, they suggested that Li<sub>2</sub>O, generated from SnO<sub>2</sub>, is reacted to electrochemically reduced Mo metal and this reaction might contribute to increasing the reversible capacity of SnO<sub>2</sub>-transition metal oxide composite.[32] In this study, we intentionally designed double shelled hollow structure to maximize this reaction even though the reaction mechanism for extraordinary capacity has not been well-established. And the reversible capacity of SnO<sub>2</sub>@Co<sub>3</sub>O<sub>4</sub> hollow sphere is successfully improved. The increasing of 1st cycle columbic efficiency might be resulted from this reaction, and further possibility for this phenomenon will be discussed in last paragraph.

The both of SnO<sub>2</sub>@Co<sub>3</sub>O<sub>4</sub> hollow sphere and SnO<sub>2</sub> hollow sphere electrodes show the good cyclability due to their hollow nature (Figure 2.2.6). The

reversible capacity of SnO<sub>2</sub>@Co<sub>3</sub>O<sub>4</sub> hollow sphere is about 963 mAh g<sup>-1</sup> after 100 cycles while that of SnO<sub>2</sub> hollow sphere is about 580 mAh g<sup>-1</sup>. And the good cyclability of SnO<sub>2</sub>@Co<sub>3</sub>O<sub>4</sub> hollow sphere electrode is well maintained at even higher current density at 500, 900 mA g<sup>-1</sup>.

TEM image of SnO<sub>2</sub>@Co<sub>3</sub>O<sub>4</sub> hollow sphere electrode after 50 cycles show the retention of the hollow structure (Figure 2.2.7). Compared to the pristine SnO<sub>2</sub>@Co<sub>3</sub>O<sub>4</sub> hollow sphere electrode, the entire hollow sphere is well-maintained. The weak and broad ring pattern is observed from SAED pattern and it is index only Sn phase. The significant grain growth is usually occurred Sn based material during discharge and charge process. But the very weak and broad ring pattern indicates that aggregation of Sn is not occurred and those components is still existed as nanocrystalline. However, cobalt oxide related phase is not observed.

Figure 2.2.8(a) is the differential capacity plot (DCP) of the nano-SnO<sub>2</sub>@Co<sub>3</sub>O<sub>4</sub> hollow sphere electrode when the electrode was cycled between 2.5 V and 0.0 V (vs. Li/Li<sup>+</sup>) for the first and second cycle. Ex situ XRD and HRTEM analyses were conducted to establish the reaction mechanism of the SnO<sub>2</sub>@Co<sub>3</sub>O<sub>4</sub> hollow sphere electrode at selected potentials as indicated in DCP. The ex-situ XRD was performed but any peak was not obtained from

pristine, lithiated and delithiated electrodes due to their nano-sized hollow nature.

Figure 2.2.9 and 2.2.10 show the TEM images and selected area electron diffraction (SAED) patterns of the  $\text{SnO}_2@\text{Co}_3\text{O}_4$  hollow sphere electrode. The interplanar spacings (d-values) corresponding to the marked regions and their comparison with the reported values of  $\text{Li}_x\text{Co}_3\text{O}_4$ ,  $\text{SnO}_2$ , Sn, Co and  $\text{Co}_3\text{O}_4$  from the JCPDS files are shown.[53] The SAED pattern comprises diffuse set of rings/diffuse bright spots indicating the very small size of crystallites and it seems that some of the planes are overlapped and appearing as the diffuse bright rings and spots. Those d-values, derived from the Figure 2.2.9 and 2.2.10, are also shown in Table and show pretty good agreement with the reported values. When the potential was lowered to 1.20 V,  $\text{Li}_x\text{Co}_3\text{O}_4$  ( $\text{Li}_{1.47}\text{Co}_3\text{O}_4$ ) and  $\text{SnO}_2$  patterns were observed. And, when the potential was reached to 0.0V, patterns of  $\text{Li}_{122}\text{Sn}_5$  and Co were observed. These results, about  $\text{SnO}_2$  and  $\text{Co}_3\text{O}_4$  reaction with Li, were agreed with other individual reports.[54, 55] During the charging process, Li-Sn binary phase was decompose to Sn at 0.49 V and some SnO phase was observed when the electrode was charged to 2.50 V. In case of  $\text{Co}_3\text{O}_4$  layer, Co is fully oxidized to  $\text{Co}_3\text{O}_4$  when the electrode was charged to 2.50 V even though Co phase is not clearly observed at 0.90 V. Indeed, the oxidation from Sn to  $\text{SnO}_2$  is still controversial; Lian et al and Mohamedi et al suggested that the partial

recombination is occurred at near 1.2 V after dealloying process of Li-Sn binary phase.[56,57] The high reversible capacity of  $\text{SnO}_2@\text{Co}_3\text{O}_4$  is suggested with follow reasons. First, reduced Co nanoparticles on the surface of  $\text{SnO}_2$  hollow sphere leads to the formation of stable polymer/gel like film. Tarascon et al studied that the highly reactive metallic nanoparticle promotes the growth of a conducting polymeric film, which show the reversible capacity of 150 mAh/g. This polymer/gel liked film forms at low voltage (between 0 and 1.8 V) and fully dissolves at over 2 V. And the partial recombination of Sn to SnO or  $\text{SnO}_2$  by Co (or  $\text{Co}_3\text{O}_4$ ) nanoparticle on  $\text{SnO}_2$  hollow sphere might slightly contribute to the extra reversible capacity.

#### **2.2.4. Conclusion**

In this study, the  $\text{SnO}_2@\text{Co}_3\text{O}_4$  hollow sphere was prepared by simple sol-gel process. The morphology of hollow sphere became rough after coating of cobalt oxide, but cobalt oxide related phases were not detected by XRD and TEM. The oxidation state of cobalt oxide is matched to that of  $\text{Co}_3\text{O}_4$ . The STEM analysis demonstrated that the Co element is well dispersed on the  $\text{SnO}_2$  hollow sphere. The  $\text{SnO}_2@\text{Co}_3\text{O}_4$  hollow sphere showed the higher electrochemical capacity than  $\text{SnO}_2$  hollow sphere. The reversible capacity of  $\text{SnO}_2@\text{Co}_3\text{O}_4$

hollow sphere electrode is  $963 \text{ mAh g}^{-1}$  after 100 cycles, and it showed also good rate capability. At higher current density of 500 and  $900 \text{ mA g}^{-1}$ , the  $\text{SnO}_2@\text{Co}_3\text{O}_4$  hollow sphere electrode show good cyclability and high reversible capacity ( $721 \text{ mAh g}^{-1}$  at  $500 \text{ mA g}^{-1}$  and  $394 \text{ mAh g}^{-1}$  at  $900 \text{ mA g}^{-1}$  after 50 cycles).

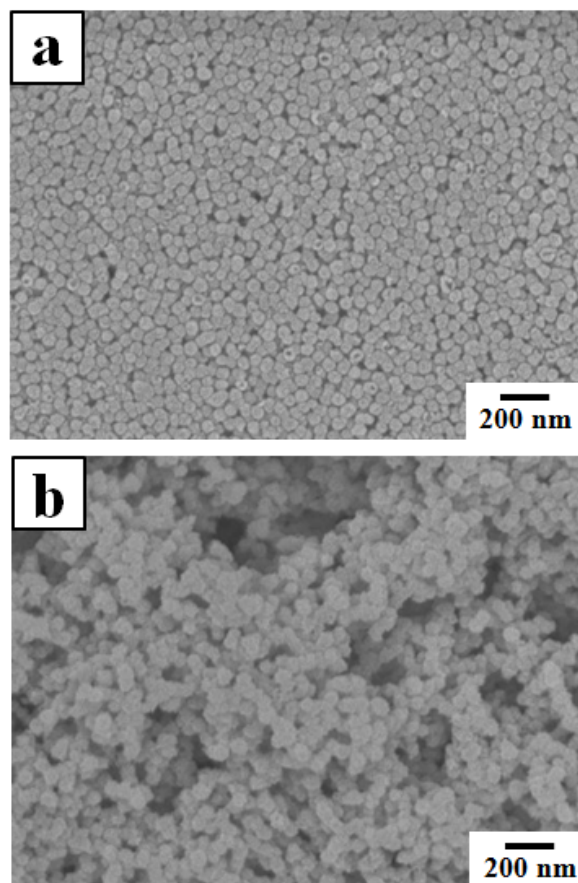


**Figure 2.2.1.** SEM images of (a) SnO<sub>2</sub> hollow sphere and (b) SnO<sub>2</sub>@cobalt oxide hollow sphere.

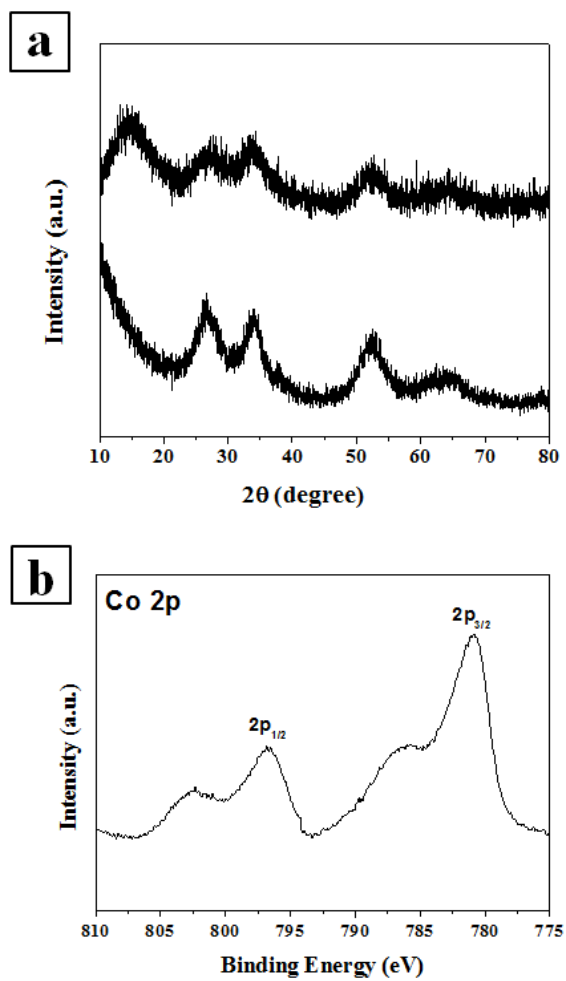


**Figure 2.2.2.** (a) XRD of SnO<sub>2</sub> hollow sphere and SnO<sub>2</sub>@cobalt oxide hollow sphere, (b) Co2p XPS of SnO<sub>2</sub>@cobalt oxide hollow sphere.

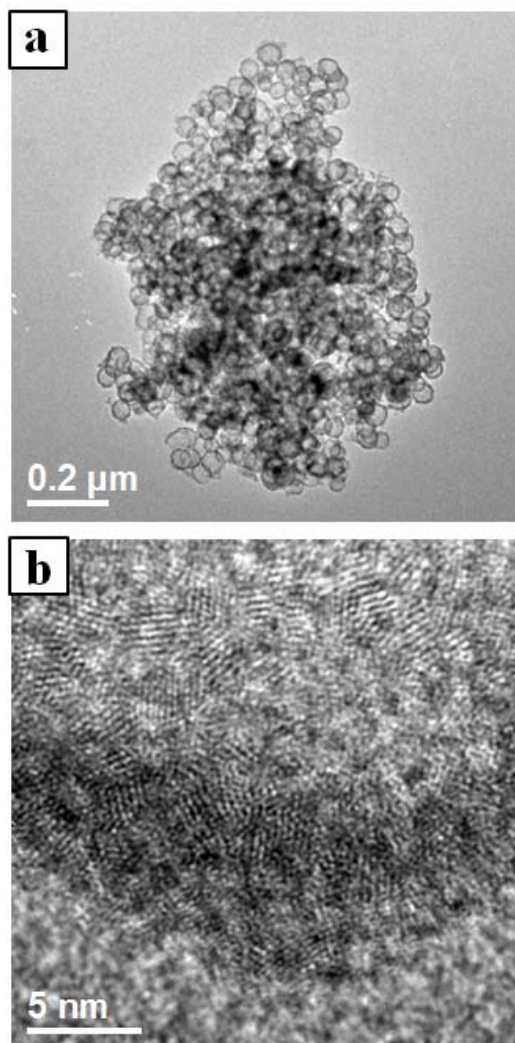


**Figure 2.2.3.** TEM images of SnO<sub>2</sub>@cobalt oxide hollow sphere (a) low- and (b) high- magnification.

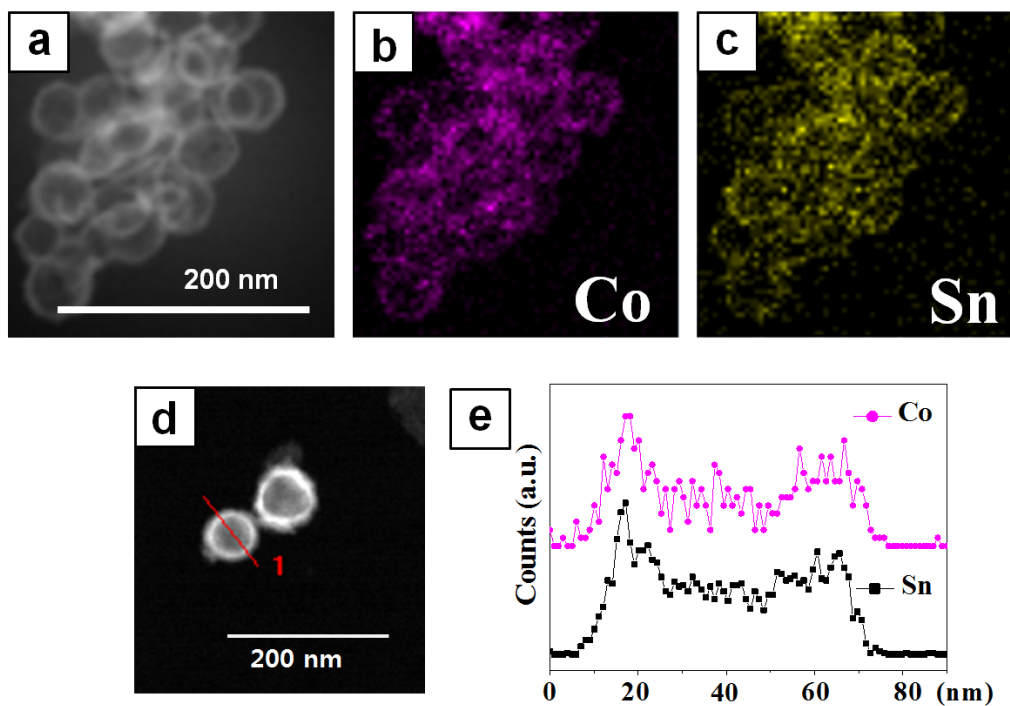


**Figure 2.2.4.** (a) STEM images of SnO<sub>2</sub>@cobalt oxide hollow sphere and EDX mapping of (b) cobalt and (c) Tin. (d) and (e) line scan profile of Co and Tin elements.

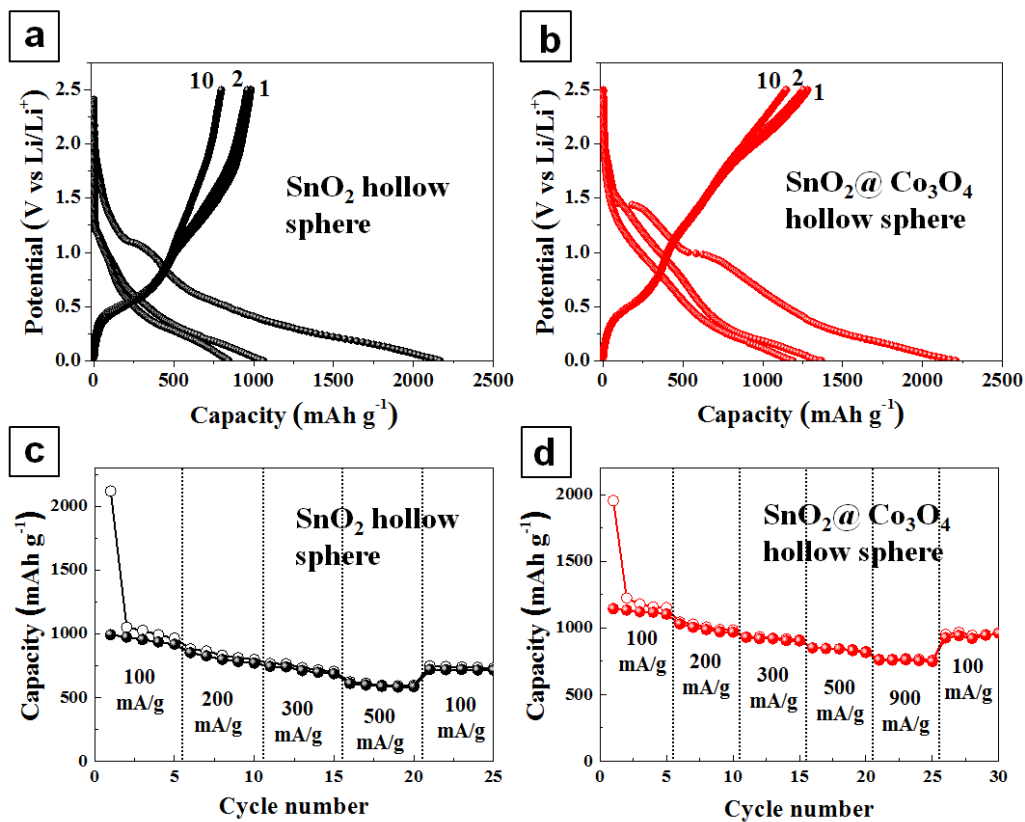


**Figure 2.2.5.** Voltage profiles of (a) SnO<sub>2</sub> and (b) SnO<sub>2</sub>@Co<sub>3</sub>O<sub>4</sub> multi-layered hollow sphere between 0.01 and 2.5 V at 100 mA g<sup>-1</sup>, rate capabilities of (c) SnO<sub>2</sub> and (d) SnO<sub>2</sub>@Co<sub>3</sub>O<sub>4</sub> multi-layered hollow sphere.

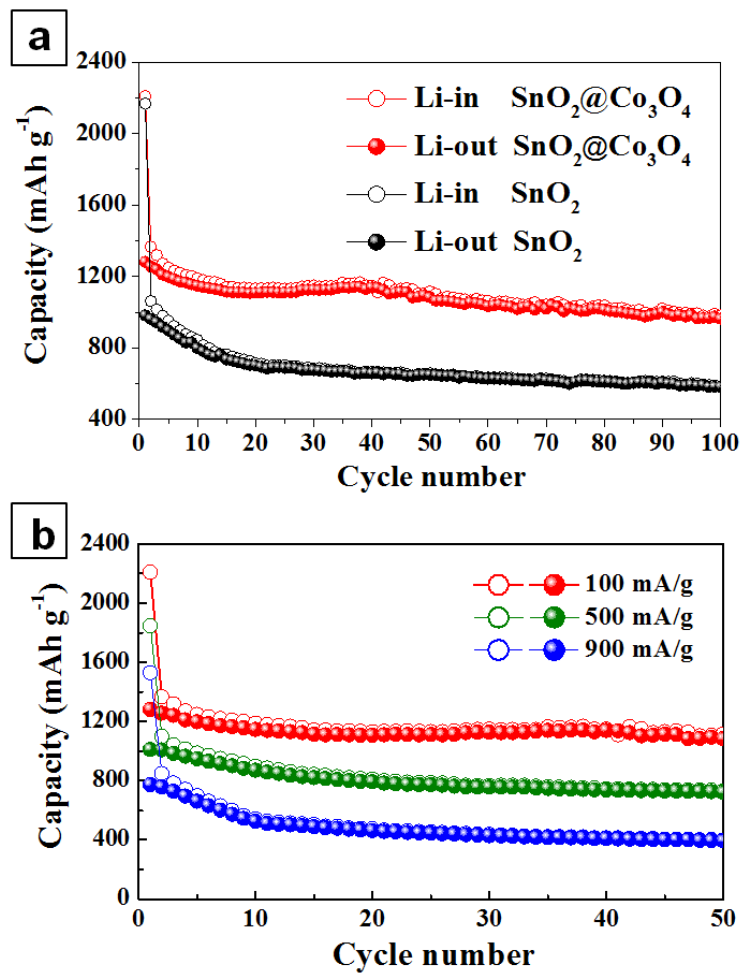


**Figure 2.2.6.** (a) cycling performance of SnO<sub>2</sub> and SnO<sub>2</sub>@Co<sub>3</sub>O<sub>4</sub> multi-layered hollow sphere at 100 mA g<sup>-1</sup>, (b) cycling performance of SnO<sub>2</sub>@Co<sub>3</sub>O<sub>4</sub> multi-layered hollow sphere at 100, 500, and 900 mA g<sup>-1</sup>.

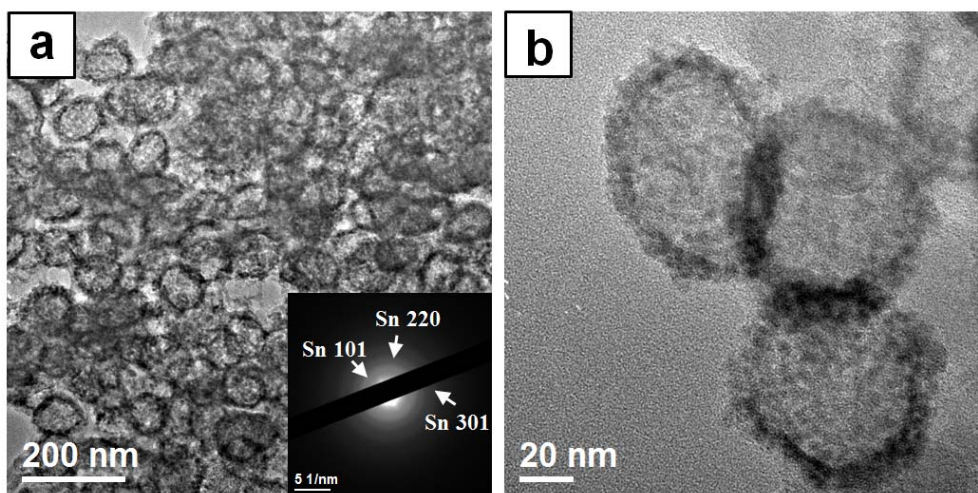


**Figure 2.2.7.** (a) and (b) TEM images of  $\text{SnO}_2@\text{Co}_3\text{O}_4$  hollow sphere after 50 cycles at  $100 \text{ mA g}^{-1}$ .

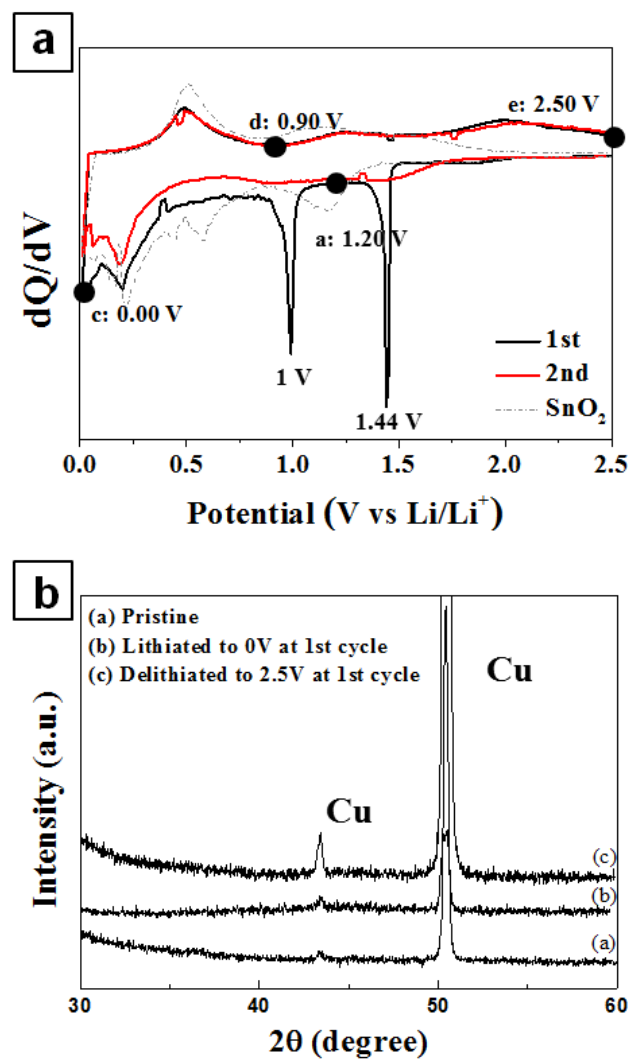


**Figure 2.2.8.** (a) DCP (differential capacity plot) of  $\text{SnO}_2@\text{Co}_3\text{O}_4$  hollow sphere at 1<sup>st</sup> and 2<sup>nd</sup> cycles, (b) ex-situ XRD analysis.

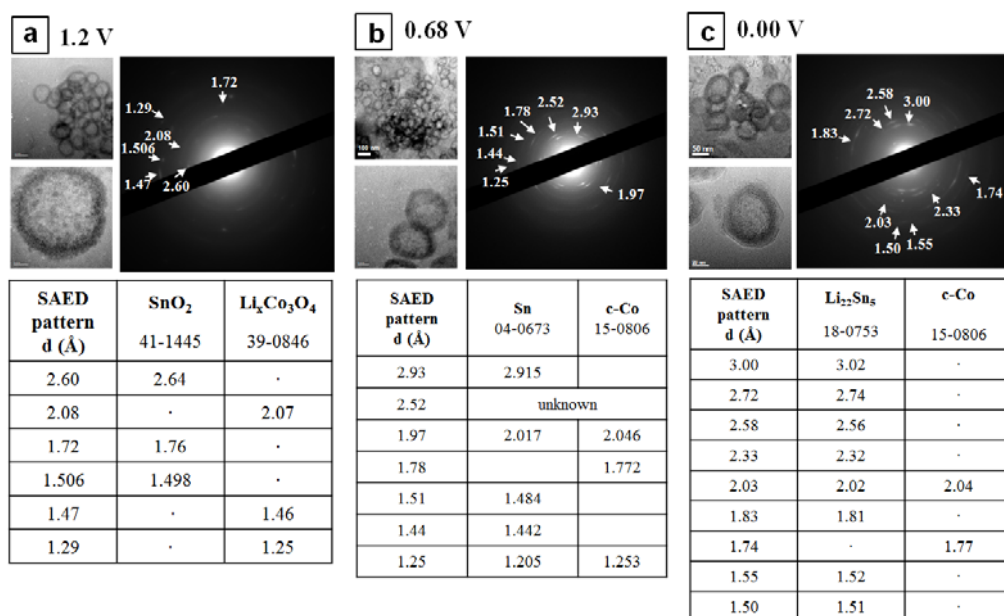


**Figure 2.2.9.** Ex-situ TEM images with SAED patterns of the SnO<sub>2</sub>@Co<sub>3</sub>O<sub>4</sub> hollow sphere electrode. Discharge process: (a) 1.20 V, (b) 0.68 V, (c) 0.00V.

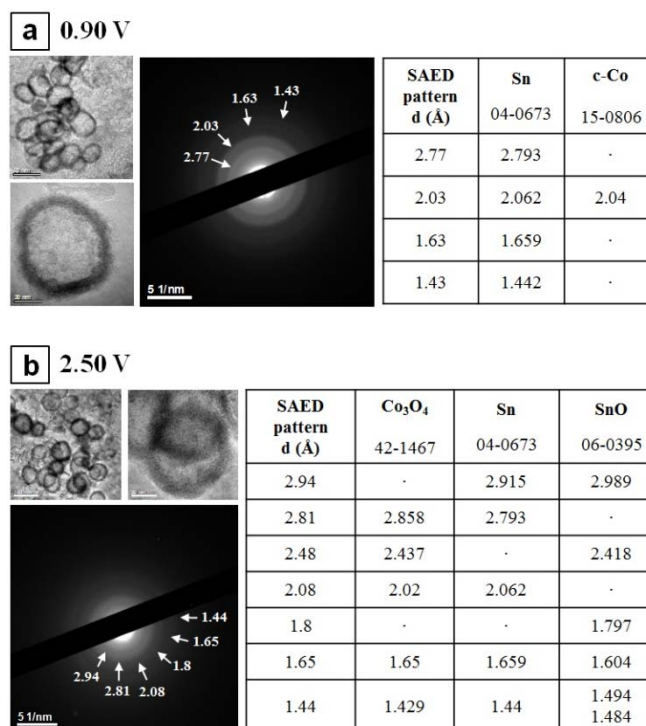


**Figure 2.2.10.** Ex-situ TEM images with SAED patterns of the SnO<sub>2</sub>@Co<sub>3</sub>O<sub>4</sub> hollow sphere electrode. Charge process: (a) 0.90 V, (b) 2.50 V.

### 2.3. Reference

- (1) B. Scrosati, *Nature*, 1995, 373, 557-558.
- (2) S. Megahed and W. Ebner, *J. Power. Sourc.*, 1995, 54, 155-162.
- (3) Y. Nishi, *J. Power. Sourc.*, 2001, 100, 101-106.
- (4) M. Endo, C. Kim, K. Nishimura, T. Fujino and K. Miyashita, *Carbon*, 2000, 38, 183-197.
- (5) D. Fauteux and R. Koksang, *J. Appl. Electrochem.*, 1993, 23, 1-10.
- (6) L. Ji, Z. Lin, M. Alcoutlabi and X. Zhang, *Energ. Environ. Sci.*, 2011, 4, 2682-2699.
- (7) K. T. Lee, Y. S. Jung and S. M. Oh, *J. Am. Chem. Soc.*, 2003, 125, 5652-5653.
- (8) I. A. Courtney and J. Dahn, *J. Electrochem. Soc.*, 1997, 144, 2045.
- (9) M. Winter, J. O. Besenhard, M. E. Spahr and P. Novák, *Adv. Mater.*, 1998, 10, 725-763.
- (10) H. Kim, M. Seo, M. H. Park and J. Cho, *Angew. Chem. Int. Ed.*, 2010, 49, 2146-2149.
- (11) C. Kim, M. Noh, M. Choi, J. Cho and B. Park, *Chem. Mater.*, 2005, 17, 3297-3301.
- (12) M. H. Park, M. G. Kim, J. Joo, K. Kim, J. Kim, S. Ahn, Y. Cui and J. Cho, *Nano Lett.*, 2009, 9, 3844-3847.
- (13) J. Ye, H. Zhang, R. Yang, X. Li and L. Qi, *Small*, 2010, 6, 296-306.

- (14) C. K. Chan, H. Peng, G. Liu, K. McIlwrath, X. F. Zhang, R. A. Huggins, Y. Cui, *Nature nanotechnology*, 2007, 3, 31-35.
- (15) C. K. Chan, X. F. Zhang and Y. Cui, *Nano Lett.*, 2008, 8, 307-309.
- (16) J. Y. Huang, L. Zhong, C. M. Wang, J. P. Sullivan, W. Xu, L. Q. Zhang, S. X. Mao, N. S. Hudak, X. H. Liu and A. Subramanian, *Science*, 2010, 330, 1515.
- (17) M. S. Park, G. X. Wang, Y. M. Kang, D. Wexler, S. X. Dou and H. K. Liu, *Angew. Chem.*, 2007, 119, 764-767.
- (18) H. Kim, B. Han, J. Choo and J. Cho, *Angew. Chem.*, 2008, 120, 10305-10308.
- (19) H. Jia, P. Gao, J. Yang, J. Wang, Y. Nuli and Z. Yang, *Adv. Energy Mater.*, 2011. 1, 1036-1039
- (20) H. Kim and J. Cho, *J. Mater. Chem.*, 2008, 18, 771-775.
- (21) Y. Yao, M. T. McDowell, I. Ryu, H. Wu, N. Liu, L. Hu, W. D. Nix and Y. Cui, *Nano Lett.*, 2011. 11, 2949-2954
- (22) M. H. Park, K. Kim, J. Kim and J. Cho, *Adv. Mater.*, 2010, 22, 415-418.
- (23) H. Ma, F. Cheng, J. Y. Chen, J. Z. Zhao, C. S. Li, Z. L. Tao and J. Liang, *Adv. Mater.*, 2007, 19, 4067-4070.
- (24) X. M. Yin, C. C. Li, M. Zhang, Q. Y. Hao, S. Liu, L. B. Chen and T. H. Wang, *J. Phys. Chem. C*, 2010, 114, 8084-8088.
- (25) S. Han, B. Jang, T. Kim, S. M. Oh and T. Hyeon, *Adv. Funct. Mater.*, 2005, 15, 1845-1850.

- (26) H. X. Yang, J. F. Qian, Z. X. Chen, X. P. Ai and Y. L. Cao, *J. Phys. Chem. C*, 2007, 111, 14067-14071.
- (27) D. Deng and J. Y. Lee, *Chem. Mater.*, 2008, 20, 1841-1846.
- (28) L. Xiao, J. Li, Q. Li and L. Zhang, *J. Solid State Electrochem.*, 2010, 14, 931-936.
- (29) S. Ding, J. S. Chen, G. Qi, X. Duan, Z. Wang, E. P. Giannelis, L. A. Archer and X. W. Lou, *J. Am. Chem. Soc.*, 2010, 133, 21-23
- (30) Z. Wang, D. Luan, F. Y. C. Boey and X. W. Lou, *J. Am. Chem. Soc.*, 2011, 133, 4738-4741.
- (31) X. W. Lou, Y. Wang, C. Yuan, J. Y. Lee and L. A. Archer, *Adv. Mater.*, 2006, 18, 2325-2329.
- (32) X.-Y. Xue, Z.-H. Chen, L.-L. Xing, S. Yuan and Y.-J. Chen, *Chem. Commun.*, 2011, **47**, 5205-5207
- (33) W. Zhou, C. Cheng, J. Liu, Y. Y. Tay, J. Jiang, X. Jia, J. Zhang, H. Gong, H. H. Hng, T. Yu, H. J. Fan, *Adv. Funct. Mater.* 2011, 21, 2439-2445.
- (34) X.-Y. Xue, B. He, S. Yuan, L.-L. Xing, Z.-H. Chen and C.-h. Ma, *Nanotechnology*, 2011, 22, 395702.
- (35) W. Stober, A. Fink and E. Bohn, *J. Colloid Interface Sci.*, 1968, 26, 62-69.
- (36) J. Kim, L. Kim and C. Kim, *Biomacromolecules*, 2007, 8, 215-222.
- (37) K. T. Nam, D. -W. Kim, P. J. Yoo, C. -Y. Chiang, N. Meethong, P. T.

- Hammond, Y. -M. Chiang, A. M. Belcher, *Science*, 2006, 312, 885-888
- (38) J. -M. Tarascon, S. Grugeon, M. Morcrette, S. Laruelle, P. Rozier, P. Poizot, *C. R. Chimie*, 2005, 8, 9-15
- (39) H. Kim, S. -W. Kim, Y. -U. Park, H. Gwon, D. -H. Seo, Y. Kim, K. Kang, *Nano Res.*, 2010, 3, 813-821.
- (40) J. S. Chen, C. M. Li, W. W. Zhou, Q. Y. Yan, L. A. Archer, X. W. Lou, *Nanoscale*, 2009, 1, 280-285
- (41) Z. Shan, G. Adesso, A. Cabot, M. Sherburne, S. A. S. Asif, O. Warren, D. Chrzan, A. Minor and A. Alivisatos, *Nature Mater.*, 2008, 7, 947-952.
- (42) S. Laruelle, S. Grugeon, P. Poizot, M. Dollé, L. Dupont, J-M. Tarascon, 2002, 149 (5), A627-A634.
- (43) Y. -M. Kang, M. -S. Song, J. -H. Kim, H. -S. Kim, M. -S. Park, J. -Y. Lee, H.K. Liu, S.X. Dou, *Electrochimica Acta*, 2005, 50, 3667-3673.
- (44) N. O. V. Plank, H. J. Snaith, C. Ducati, J. S. Bendall, L. Schmidt-Mende, M. E. Welland, *Nanotechnology* 19 (2008) 465603
- (45) G. Qi, Y. Liu, W. Jiao, L. Zhang, *Micro & Nano Letters*, 2010 (5), 278-281.
- (46) Y. Qiu, J. Yu, *Solid State Communications*, 2008, 148, 556-558.
- (47) Q.-L. Ye, H. Yoshikawa, K. Awaga, *Materials* 2010, 3, 1244-1268.
- (48) H. Qian, G. Lin, Y. Zhang, P. Gunawan, R. Xu, *Nanotechnology* 18 (2007) 355602.

- (49) G. A. Carson, M. H. Nassir, M. A. Langell, *J. Vac. Sci. Technol. A*, 1996(14), 1637.
- (50) M. Burriel, G. Garcia, J. Santiso, A. Abrutis, *Chem. Vap. Deposition*, 2005 (11) 106.
- (51) X. W. Lou, D. Deng, J. Y. Lee, L. A. Archer, *J. Mater. Chem.*, 2008, 18, 4397–4401.
- (52) N. Yan, L. Hu, Y. Li, Y. Wang, H. Zhong, X. Hu, X. Kong, Q. Chen, *J. Phys. Chem. C* 2012, 116, 7227–7235.
- (53) M.M. Thackeray, S.D. Baker, K.T. Adendorff, *Solid State Ionics*, 1985 (17), 175 – 181.
- (54) I. A. Courtney, J. R. Dahn, *J. Electrochem. Soc.*, 1997 (144), 2045-2052.
- (55) D. Larchera, G. Sudanta, J.-B. Leriche, Y. Chabreb, J.-M. Tarascona, *Journal of The Electrochemical Society*, 2002 (149), A234-A241.
- (56) M. Mohamedi, S.-J. Lee, D. Takahashi, M. Nishizawa, T. Itoh, I. Chida, *Electrochim. Acta*. 2001(46) 1161.
- (57) P. Lian, X. Zhu, S. Liang, Z. Li, W. Yang, H. Wang, *Electrochim. Acta*. 2011, 56, 4532.

## **Chapter 3.**

### **Preparation of One-dimensional SnO<sub>2</sub>**

### **Nanostructures for Gas Sensing**

### **Application**

## **3.1. Synthesis of SnO<sub>2</sub> nanotube for gas sensing application**

### **3.1.1. Introduction**

Tin dioxide (SnO<sub>2</sub>) is a wide band gap (3.6 eV) n-type semiconductor and extensively studied as gas sensors detecting various flammable and toxic gases [1-8]. To enhance the sensitivity and selectivity toward certain gases or to reduce the operating temperature, various techniques have been explored to fabricate SnO<sub>2</sub> nanostructures. Among them, nanotubes are highly expected to enhance the gas sensing performance [7-10], because the tubular structure can provide a higher surface-to-volume ratio (outer and inner surfaces) for gas adsorption/desorption. Various methods to fabricate SnO<sub>2</sub> nanotubes have been explored including thermal evaporation [11][12], hydrothermal process [13], infiltration casting [14], sol-gel template [15][16], electrochemical deposition [17,18], etc. The commonly employed templates for nanotube fabrication were anodized aluminum oxide (AAO), polycarbonate membranes, etc [17-20]. However, the nanotubes based on these templates have structural limitations, such as large crystallites, thick wall thickness (over 10 nm), and short tube length (a few  $\mu\text{m}$  at most).

Electrospinning has been proved to be a versatile and effective method to fabricate one-dimensional nanoscale fibers for inorganic as well as organic

materials. Electrospun metal oxide fibers are generally composed of nanocrystallites, which stimulates great interest in applications such as gas sensor [6,19,20], photocatalyst [21], lithium ion battery [22], and solar cell [23], etc. In addition, electrospun polymeric nanofibers have been used as a template for metal oxide nanotube synthesis because of their low cost, easy control of nanofiber dimension, and high yield [24-29]. Atomic layer deposition (ALD) has been employed to fabricate the metal oxide nanotubes on electrospun polymer fibers because it is a self-limiting process and has unique advantages such as superior step coverage, uniformity, and atomic scale thickness control [24, 26] compared to sol-gel [28], PVD, and CVD methods [29]. Al<sub>2</sub>O<sub>3</sub> and TiO<sub>2</sub> nanotubes have been fabricated by ALD on the electrospun polymer templates [24-27], but this strategy has not been applied to the fabrication of SnO<sub>2</sub> nanotube for gas sensing application.

Here, we study a novel strategy to synthesize SnO<sub>2</sub> nanotubes with a precisely controlled diameter and wall thickness by combining electrospinning and ALD techniques and to fabricate the nanotube network sensor for gas sensing application. Polyacrylonitrile (PAN) was chosen as a electrospinning material and electrospun PAN nanofibers were used as a template for SnO<sub>2</sub> coating, which is durable under O<sub>2</sub> plasma during ALD process and can be removed by calcination for the nanotube formation. For SnO<sub>2</sub> deposition on the polymeric PAN

nanofibers, plasma enhanced atomic layer deposition (PEALD) using dibutyl tin diacetate (DBTDA) as Sn source has been explored to reduce the growth temperature down to 100 °C and overcome the halide contamination [30] instead of commonly employed SnCl<sub>4</sub> [31,32] and SnI<sub>4</sub> [31,33], which requires a relatively high growth temperature (~600 °C). The SnO<sub>2</sub> nanotube network was placed on the Pt electrode patterned SiO<sub>2</sub>/Si substrate and the gas sensing characteristics of network sensor were investigated, particularly focusing on the ethanol detection.

### **3.1.2. Experimental procedure**

*1) Preparation of electrospun PAN Nanofiber:* For electrospinning, PAN (MW= 200,000 g mol<sup>-1</sup>, Misui chemical) was dissolved in dimethylformamide (DMF, purity = 99.5%, Daejung chemical) and the concentration of the solution was fixed to be 10 wt% to produce the uniform nanofibers with an average diameter of 100~200 nm. The optimum electrospinning conditions were determined as follows; applied voltage: 20 kV, tip-to-collector distance: 10 cm, and flow rate of solution: 0.5 ml h<sup>-1</sup>. The as-electrospun PAN nanofibers were subsequently stabilized at 250 °C for 2 h to transform their linear molecular structure to six-membered ring structure. The stabilized PAN nanofibers could withstand in thermally harsh environment, i.e. O<sub>2</sub> plasma and became an adequate template for subsequent SnO<sub>2</sub> coating by ALD.

**2) SnO<sub>2</sub> coating on PAN Nanofiber by PEALD:** SnO<sub>2</sub> thin films were coated on the stabilized PAN nanofibers by plasma enhanced atomic layer deposition (PEALD). Dibutyltindiacetate (DBTDA) ((CH<sub>3</sub>CO<sub>2</sub>)<sub>2</sub>Sn [(CH<sub>2</sub>)<sub>3</sub>-CH<sub>3</sub>]<sub>2</sub>) was used as Sn precursor and it was evaporated at 40 °C and transported to the deposition chamber by Ar (99.99%) gas of 50 sccm. The O<sub>2</sub> (99.99%) and Ar (99.99%) gases of 50 sccm were used as plasma and purge gases, respectively. The time sequence for source pulse, first purge, plasma pulse, and second purge was 3, 12, 12, and 12 s, respectively. The deposition was conducted with an rf power of 100 W at 240 mtorr and the substrate temperature during deposition was maintained at 100 °C. The thickness of SnO<sub>2</sub> thin films was controlled by the number of ALD cycles, e.g., 100, 300, and 500 cycles. The SnO<sub>2</sub> thin film coated PAN nanofibers were annealed at 700 °C for 1 h to burn out the PAN template and crystallize the SnO<sub>2</sub>.

**3) Characterization:** The phase of as-prepared SnO<sub>2</sub> nanotubes was examined by X-ray diffraction (XRD, M18XHF-SRA, MAC Science Co.). The morphology was observed by field emission scanning electron microscopy (FE-SEM, JSM-6330F, JEOL) and high resolution transmission electron microscopy (HRTEM, JEM-3000F, JEOL).

**4) Measurement of gas sensing properties:** For the gas sensing measurements, a pair of comb-like Pt electrodes were formed on the SiO<sub>2</sub>/Si substrate by sputtering through a mask and Au wires were attached to them using silver (Ag) paste. The

Pt patterned SiO<sub>2</sub> substrate was then annealed at 600 °C for 1 h in order to ensure the electrical contact between Ag paste and Au wires. Thereafter, a piece of SnO<sub>2</sub> nanotube sheet was distributed on the Pt patterned SiO<sub>2</sub>/Si substrate and then annealed again at 600 °C for 1 h in air for a stable sensing. The sensor devices were placed in a quartz tube located inside an electrical tube furnace with a gas inlet and outlet. A continuous flow-through measurement system was used and the sample gases used were ethanol (5~100 ppm), H<sub>2</sub> (100 ppm), CO (100 ppm), NH<sub>3</sub> (100 ppm), and NO<sub>2</sub> (100 ppm) balanced with air. The gas sensing properties were determined by measuring the changes of the electric resistance between the sample gas and the reference gas (pure air) at various operating temperatures ranging from 300 to 500 °C. The magnitude of the gas response (S, sensitivity) was defined as a ratio of  $R_{\text{air}}/R_{\text{gas}}$ , i.e., the ratio of the electrical resistance in air ( $R_{\text{air}}$ ) to that in the sample gas ( $R_{\text{gas}}$ ). The response time ( $t_{90\%}$ ) was defined as the times required for the sensor to reach 90% of the final signal.

### **3.1.3. Results and discussion**

#### ***Fabrication and characterization of SnO<sub>2</sub> nanotubes***

SnO<sub>2</sub> nanotubes were fabricated in four steps, and the representative FESEM images in each step are presented in Figure 3.1.1. The as-electrospun

PAN nanofibers had a relatively uniform diameter of 100~200 nm and were connected each other forming a self-supporting network (Figure 3.1.1(a)). The surface of as-electrospun nanofibers appeared to be wavy, which became smooth after stabilization at 250 °C for 2 h without a significant change of their dimensions (Figure 3.1.1(b)) [34]. The ALD process yielded the uniform and conformal SnO<sub>2</sub> coating on the PAN templates preserving the original arrangements of as-electrospun nanofibers (Figure 3.1.1(c)). The calcination at 700 °C removed the PAN nanofiber cores resulting in the SnO<sub>2</sub> nanotubes, and the inset in Figure 3.1.1(d) clearly showed the nanotubes of uniform wall thickness without any structural distortion such as wrinkle or collapse. In case of non-stabilized PAN nanofiber templates, SnO<sub>2</sub> nanotubes showed a wrinkle structure and in some cases, they were partially disintegrated (Figure 3.1.2).

No distinctive diffraction peaks were observed in the XRD patterns of as-electrospun and as-stabilized PAN nanofibers except the broad peak around 20 ° (Figure 3.1.3(a) and (b)). It was reported that as-electrospun PAN nanofibers had the diffraction peaks at 16.8 and 28.6 °, and as-stabilized PAN nanofibers exhibited the broad peak at 25.3 ° [35]. These diffraction peaks might be obscured by the broad background originating from the glass holder and could not be observed in this study. Furthermore, the SnO<sub>2</sub> coated PAN nanofibers did not

exhibit any diffraction peak (Figure 3.1.3(c)), possibly due to a non-crystalline nature of oxide coating resulting from the low substrate temperature of 100 °C. It was reported that the crystalline SnO<sub>2</sub> thin film could be realized at the substrate temperature of  $\geq 200$  °C by PE-ALD using DBTDA [30]. However, the calcination of SnO<sub>2</sub> coated PAN nanofibers at 700 °C crystallized the amorphous coating material and resulted in a single phase of rutile SnO<sub>2</sub> (Figure 3.1.3(d)). All the diffraction peaks were broadened, which is believed to be due to a nanocrystalline nature of the obtained SnO<sub>2</sub> nanotubes.

The developed SnO<sub>2</sub> nanotubes were further characterized by transmission electron microscopy (TEM) after ultrasonically dispersing them on carbon grid. Low magnification TEM image (Figure 3.1.4(a)) revealed the tube-like structure with the center bright and the outside dark. The diameter of nanotubes was  $\sim 100$  nm and the wall thickness was seen to be uniform along the entire length. High magnification TEM image (Figure 3.1.4(b)) indicated that the nanotubes were indeed composed of interconnected nanoparticles (or nanocrystallites) of  $< 10$  nm and it clearly displayed the lattice fringes, indicating a high crystallinity. The spots and rings in the selected area electron diffraction (SAED) pattern revealed the randomly oriented polycrystalline nature of the nanotubes, and the patterns were completely indexed to the rutile SnO<sub>2</sub> (JCPDS No. 41-1445) (inset in Figure 3.1.4(b)). Some of nanoparticles clearly exhibited the lattice fringes with a lattice

spacing of 0.34 nm, which is close to the (110) interplanar spacing of cassiterite SnO<sub>2</sub> (Figure 3.1.4(c)).

The wall thickness of SnO<sub>2</sub> nanotubes was determined by TEM (Figure 3.1.5(a), (b), (c)) and plotted as a function of ALD cycle number (Figure 3.1.5 (d)). The average wall thickness was 8, 22, and 37 nm for 100, 300, and 500 ALD cycles, respectively. The wall thickness increased linearly with the ALD cycle number and the average growth rate was determined to be 0.08 nm cycle<sup>-1</sup>. The results in Figure 3.1.5 indicates that the wall thickness of SnO<sub>2</sub> nanotubes can be precisely controlled by the number of ALD cycles because of its excellent layer-growth by self-limiting surface reaction [24][26]. The quantitative determination of crystallite size in nanotubes was not possible due to the overlapping, but TEM micrographs revealed that the crystallite size was not significantly changed with the number of ALD cycles and remained approximately 10 nm size.

#### ***Gas sensing properties towards ethanol***

Figure 3.1.6(a) shows an optical micrograph of SnO<sub>2</sub> nanotube network sensor formed on the Pt patterned SiO<sub>2</sub>/Si substrate for gas sensing measurement. The gap between Pt electrodes was 0.2 mm and the width was 6.4 mm, and a piece of SnO<sub>2</sub> nanotube sheet was distributed in the middle of the pattern marked

by dash line. The SEM micrograph indicates that SnO<sub>2</sub> nanotubes were homogeneously distributed between Pt electrodes and connected each other forming the network (Figure 3.1.6(b)). Moreover, the micrographs of nanotube networks show that the length of nanotubes is more than several ten micrometers.

A typical response transient of SnO<sub>2</sub> nanotube network sensor toward 100 ppm ethanol balanced with air measured at 450 °C is shown in Figure 3.1.7. Upon injecting a target gas, the resistance rapidly decreased by more than two orders of magnitude. The recovery was slightly slow, but the sensing signal was quite stable and reversible even after switching the gases several times. The determined magnitude of gas response (S) and response time ( $t_{90\%}$ ) toward 100 ppm ethanol are shown in Figure 3.1.8 as a function of sensing temperature for the sensors formed after different ALD cycles. For comparison, the sensor was fabricated using the commercial SnO<sub>2</sub> powder (325 mesh, Aldrich) after dispersing in ethanol and depositing in the same Pt-patterned electrodes [36], and its sensing behavior was included in Figure 3.1.8(a). At low temperature (300~350 °C), the magnitude of gas response in the nanotube sensors was comparable to that of commercial powder sensor, but it was an order of magnitude higher above 400 °C. Furthermore, the nanotube sensor with a thinner wall (100 ALD cycles) showed the substantially higher gas response. Thus, the highest gas response of 188 toward 100 ppm ethanol was observed at 450 °C in the sensor formed after 100

ALD cycles, which was comparable or higher than that observed in other metal oxide sensors [37-40], other SnO<sub>2</sub> nanostructures such as nanoparticle [41,42], nanowire [43,44], nanofiber [6], nanoplate [45], and hollow sphere [46], and the commercial ethanol sensor [TGS2620, Figaro Eng.]. The crystallite size of the nanotubes was not strongly dependent on the number of ALD cycles and it was comparable to the Debye length of SnO<sub>2</sub> (~6 nm) [47]. It appears that the highest gas response in the sensor of 100 ALD cycles is due to the complete electron depletion and fast effective gas diffusion through thinnest and permeable wall of nanotubes [48]. The nanotube network sensor responded very rapidly toward ethanol and the response time was a few seconds at the temperature range investigated. In particular, the response time was significantly reduced by decreasing the wall thickness at low temperature (Figure 3.1.8(b)).

The response transients of SnO<sub>2</sub> nanotube network sensors are shown in Figure 3.1.9(a). All the sensors were stable and reversible and responded to ethanol down to 5 ppm. The magnitude of the gas response increased almost linearly with increasing ethanol concentration from 5 to 100 ppm at 450 °C (log (gas response) vs log (concentration)) (Figure 3.1.9(b)), and the sensor formed after 100 ALD cycles exhibited the higher gas response in the concentration range investigated. The nanotube network sensors also responded toward H<sub>2</sub>, CO, NH<sub>3</sub>, and NO<sub>2</sub>

gases (Figure 3.1.9(c)), but the magnitude of gas response toward other reducing gases was significantly lower than that of ethanol. Thus, the SnO<sub>2</sub> nanotube network sensors exhibited the excellent selectivity toward ethanol against H<sub>2</sub>, CO, and NH<sub>3</sub> gases. The higher selectivity toward ethanol is not well understood at this stage, but it is believed to be associated with higher reactivity of ethanol in this temperature range [44,49] and more electron generation when the same number of gas molecules react with the surface-adsorbed oxygen species than the other gases [50]. On the other hand, the gas response of nanotube network sensor toward oxidizing NO<sub>2</sub> was comparable to that of ethanol and the nanotube network sensors showed a weak selectivity.

### **3.1.4. Conclusions**

SnO<sub>2</sub> nanotube network was successfully prepared by combining electrospinning of PAN nanofiber and atomic layer deposition of SnO<sub>2</sub> on nanofiber template. The diameter of the obtained SnO<sub>2</sub> nanotubes was 100~200 nm, and the wall thickness was controlled by the number of ALD cycles ranging from 8 to 37 nm. The structural analyses by XRD and TEM revealed that nanotube was a polycrystalline SnO<sub>2</sub> of cassiterite structure and composed of

several nanometer-sized crystallites. The gas sensing performance was investigated toward various gases, but SnO<sub>2</sub> nanotube network sensor showed an excellent selectivity toward ethanol with a fast response time. In particular, the network sensor with a thinnest wall thickness of ~8 nm showed the highest gas response of 188 toward 100 ppm ethanol at 450 °C, which was higher than the best values reported previously.

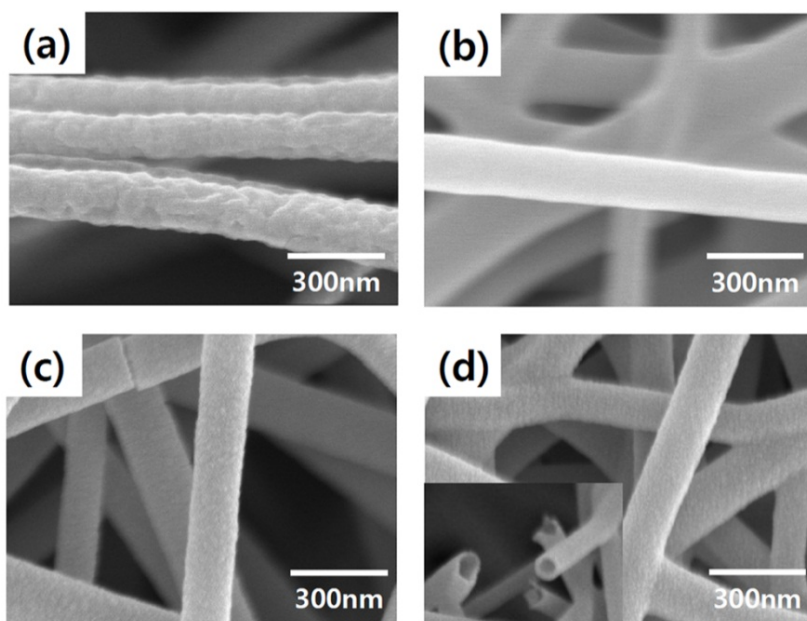


**Figure 3.1.1.** FESEM images of (a) as-electrospun PAN nanofibers, (b) as-stabilized PAN nanofibers at 250 °C, (c) SnO<sub>2</sub> coated PAN nanofibers by ALD (300 cycles at 100 °C), and (d) SnO<sub>2</sub> nanotubes after calcination at 700 °C. The inset clearly showed the tubular morphology of nanofibers.

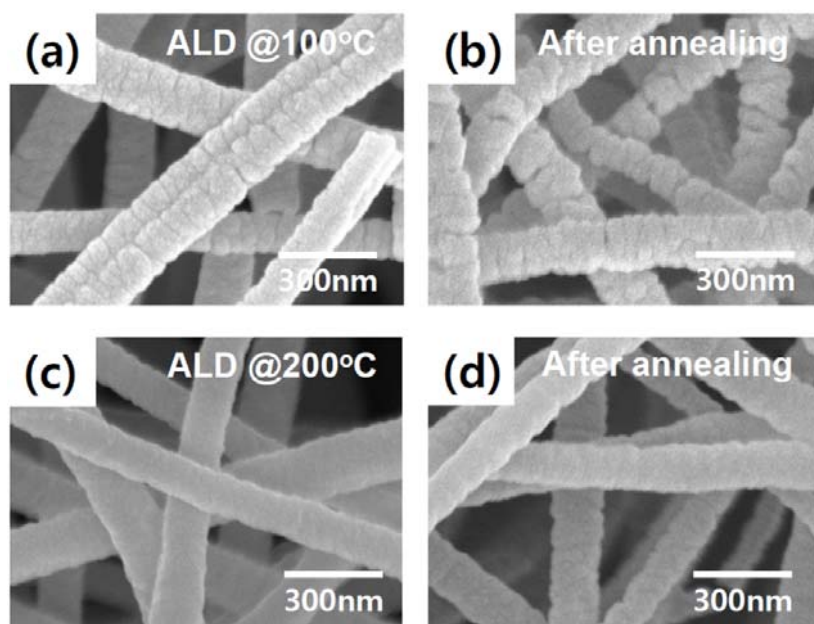


**Figure 3.2.2.** FESEM images of non-stabilized PAN nanofibers (a) after SnO<sub>2</sub> coating by ALD at 100 °C, (b) after calcining of (a) at 700 °C, (c) after SnO<sub>2</sub> coating by ALD at 200 °C, and (d) after calcining of (c) at 700 °C.

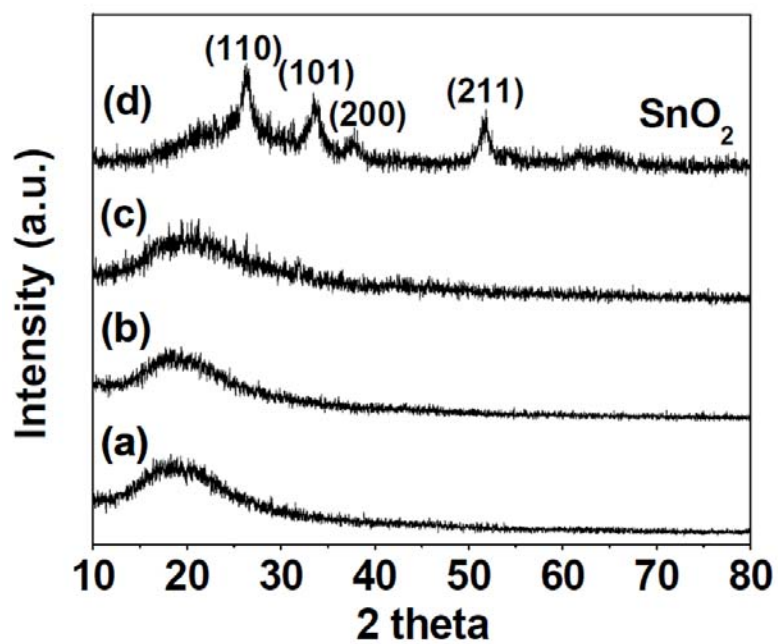


**Figure 3.1.2.** XRD patterns of (a) as-electrospun PAN nanofibers, (b) as-stabilized PAN nanofibers at 250 °C, (c) SnO<sub>2</sub> coated PAN nanofibers by ALD (300 cycles at 100 °C), and (d) SnO<sub>2</sub> nanotubes after calcination at 700 °C.

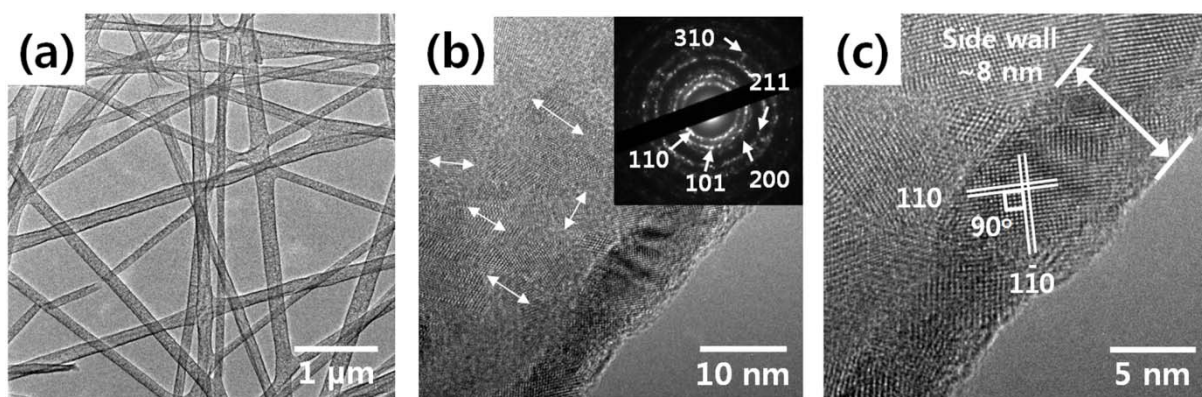


**Figure 3.1.3.** (a) Low magnification and (b), (c) high resolution TEM images of  $\text{SnO}_2$  nanotubes (100 cycles at  $100^\circ\text{C}$ ) after calcination at  $700^\circ\text{C}$ . The inset in (b) is the SAED pattern of  $\text{SnO}_2$  nanotubes.

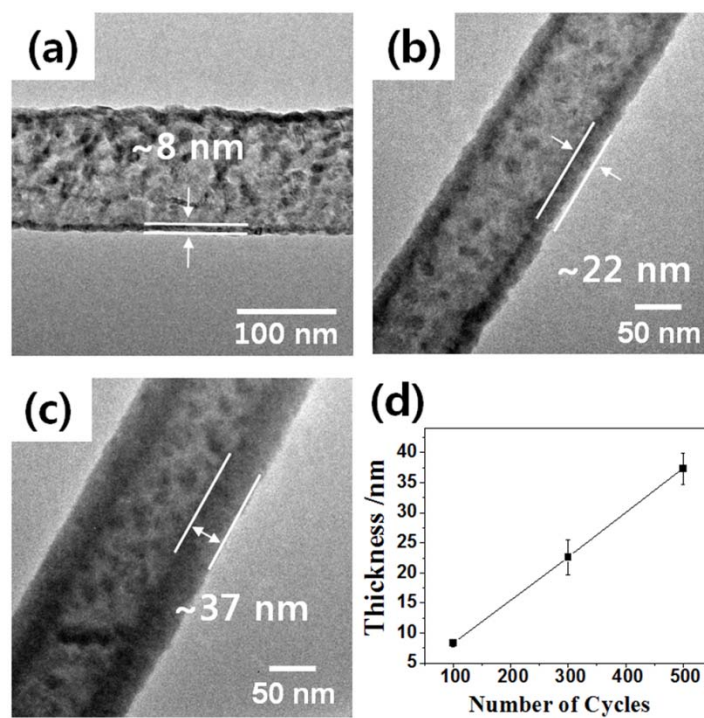


**Figure 3.1.4.** Low magnification TEM images of of SnO<sub>2</sub> nanotubes after calcination at 700 °C; (a) 100 (b) 300 (c) 500 ALD cycles, and (d) Wall thickness of SnO<sub>2</sub> nanotubes as a function of ALD cycles measured by TEM.

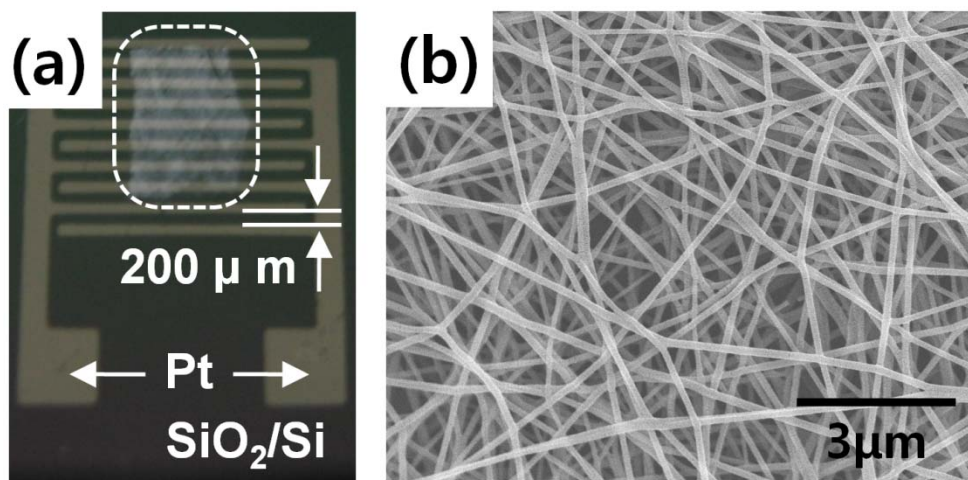


**Figure 3.1.5.** (a) Optical and (b) SEM micrographs of SnO<sub>2</sub> nanotube network sensor placed on Pt patterned SiO<sub>2</sub>/Si substrate.

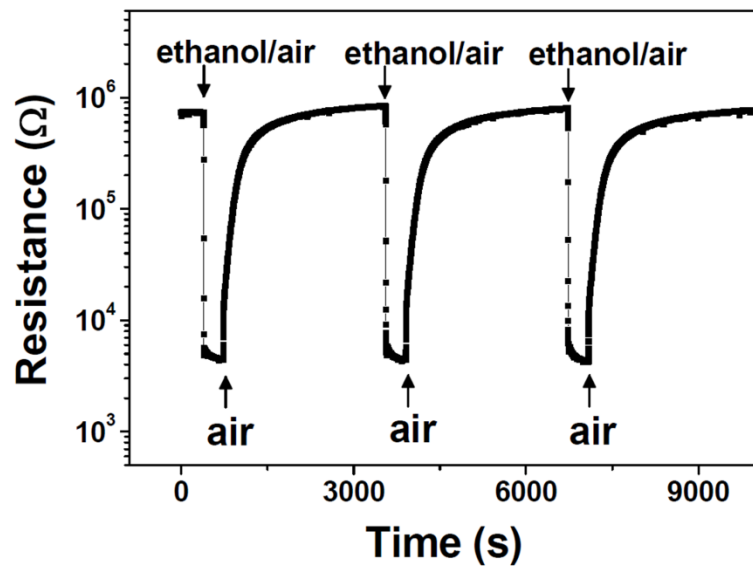


**Figure 3.1.6.** Typical response transient of SnO<sub>2</sub> nanotube network sensor toward 100 ppm ethanol.

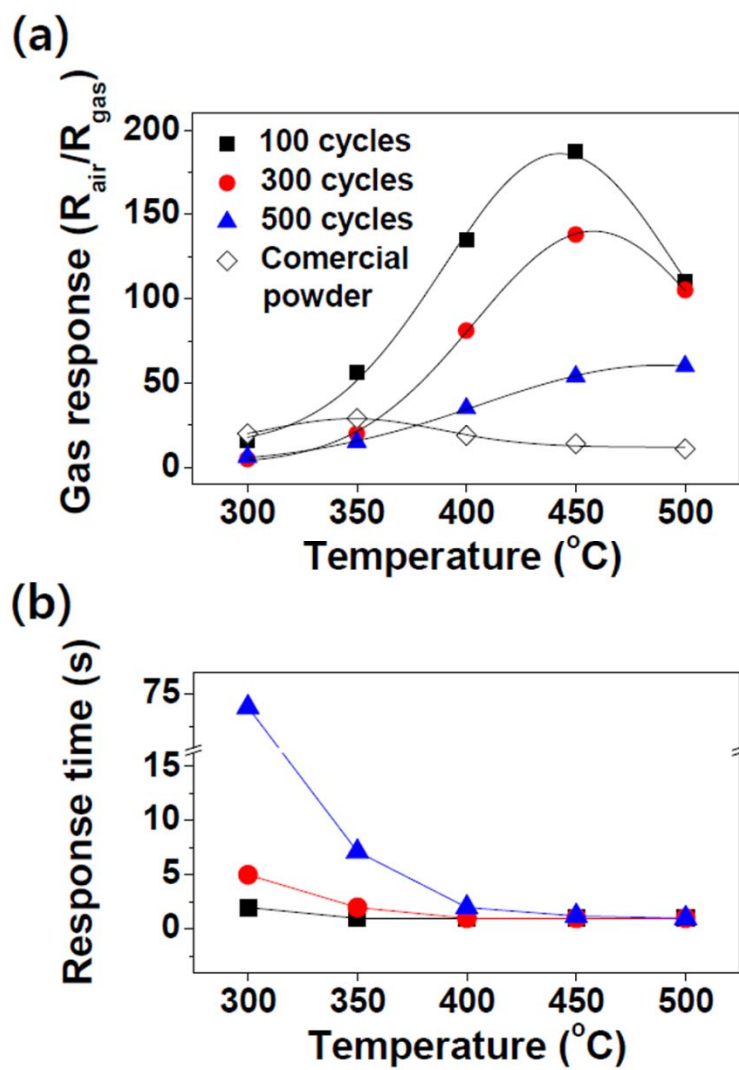


**Figure 3.1.7.** (a) Magnitude of gas response and (b) response time of SnO<sub>2</sub> nanotube network sensors toward 100 ppm ethanol as a function of sensing temperature.

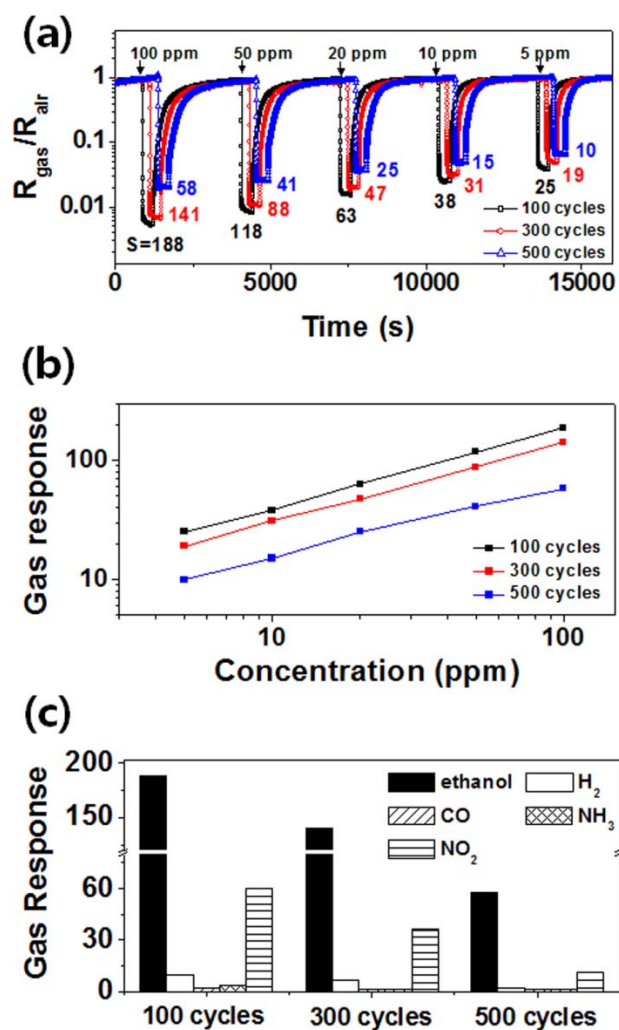


**Figure 3.1.8.** (a) Ethanol concentration dependence of gas response (b) concentration dependence of gas response at 450 °C, and (c) selectivity of SnO<sub>2</sub> nanotube network sensor toward ethanol against H<sub>2</sub>, CO, NH<sub>3</sub>, and NO<sub>2</sub> gases. In (a), the resistance in sample gas was normalized by the resistance in air for clarity.

## **3.2. Vertically grown SnO<sub>2</sub> nanowire on r-cut sapphire**

### **3.2.1. Introduction**

The alignment and placement of nano-materials are one of the key factors in the nano-scale devices. Thus, vertically well-aligned nanowires have attracted much attention because of their potential applications as vertically integrated field effect transistors (FETs),[51] light-emitting diodes,[52] highly efficient dye-sensitized solar cells,[53] nanogenerators,[54] and Li-ion batteries.[55] Well-aligned nanowires have been fabricated using hetero-epitaxial growth by various techniques in a variety of systems.[56-59]

Tin dioxide (SnO<sub>2</sub>) is a wide bandgap ( $E_g=3.6$  eV) n-type semiconductor[60] that has been used in gas sensors and bio sensors,[61,62] transparent electrodes,[63] transparent FETs,[64] and Li-ion batteries.[65] Various SnO<sub>2</sub> nanostructures such as urchin-like nanostructures,[66] nano-trees,[67] nanotubes,[68] nanofibers,[69] and nanoplates,[70] have been synthesized to improve the desired properties for many applications. The differently aligned or oriented nanostructures, particularly nanowires, are expected to exhibit the different optical and electrical properties.[71-74] However, there are a few reports on highly aligned growth of SnO<sub>2</sub> nanowires on single crystal substrates,[75-80] and the understanding of aligned SnO<sub>2</sub> nanowire growth behavior is very limited.

Recently, highly aligned (101) SnO<sub>2</sub> nanowires were epitaxially grown on

(101)  $\text{TiO}_2$  substrate by carbothermal reduction via Au catalyzed vapor-liquid-solid (VLS) growth, and the orientation relationship and interface structure between nanowire and substrate were determined.[81] The (101) oriented epitaxial or polycrystalline  $\text{SnO}_2$  thin films have been deposited on the r-cut (012) sapphire substrate and the heteroepitaxial relationships have been reported.[82] However, to our knowledge, the fabrication of vertically aligned (101)  $\text{SnO}_2$  nanowires and their heteroepitaxial relationships have not been demonstrated on the r-cut sapphire substrate.

The growth of branched nanowires has been demonstrated in many material systems,[83-85] and they offer another approach to increase structural complexity and provide greater functionality.[86-88] The branched nanowires are commonly synthesized via a controlled multistep catalyst mediated VLS process.<sup>39-40</sup> In some instances, the branched nanowires were fabricated without a multistep catalyst deposition. In that case, the catalyst migration from the tip or residual catalyst on the surface of nanowires was responsible for the growth of branches via VSL mechanism.[83,91]  $\text{SnO}_2$  nanowires with branches have been synthesized in a single or multiple step procedure,[88,90,92-93] but there is lack of report on the growth of branch nanowires from the vertically aligned trunk (or stem) nanowires and orientation relationships between substrate, trunk nanowire, and branch nanowire.

Herein we successfully fabricated the well-aligned SnO<sub>2</sub> nanowires on the r-cut sapphire substrate by carbothermal reduction via Au-catalyzed heteroepitaxial growth. The orientation relationship and interface structure between nanowires and substrate were determined by X-ray pole figure and high resolution transmission electron microscopy. The interface between Au catalyst and SnO<sub>2</sub> nanowires was also investigated to find out the orientation relationship because metal catalysts could affect the alignment or growth direction of nanowires.[94] In addition, branch nanowires were synthesized on the vertically aligned SnO<sub>2</sub> nanowires in one step without a multiple catalyst deposition just by changing the growth condition (Ar flow rate).

### **3.1.2. Experimental procedure**

*1) Preparation of Au coated substrate:* For the vertical growth of SnO<sub>2</sub> nanowire, the Au catalyst was deposited by sputter. The sputtering was conducted for 15 s at 5 mA current under 0.075 torr.

*2) Nanowire growth condition:* For SnO<sub>2</sub> nanowire synthesis, the feedstock source was prepared by thoroughly mixing SnO<sub>2</sub> powder (purity 99.99%) and graphite (purity 99.99%) in a 2:1 ratio. The feedstock was loaded into an alumina

boat and placed 7 cm upstream from the Au-coated substrate in a quartz tube. The quartz tube was then inserted into a horizontal tube furnace and evacuated by a rotary pump to a pressure of  $5 \times 10^{-2}$  torr. The furnace was heated to 800 °C at a heating rate of 10 °C/min and maintained at that temperature for 30 min under a constant Ar gas flow (300 sccm) at a total pressure of 10 torr. After deposition, the furnace was cooled to room temperature and the samples were retrieved and characterized.

**3) Characterization:** The morphology of as-synthesized product was observed by field-emission scanning electron microscopy (FE-SEM, JSM-7401F, JEOL). The phase and in- and out of-plane orientation relationships between nanowires and substrate were examined by X-ray diffraction (XRD) and X-ray pole figure (X'Pert Pro, PANalytical). High-resolution transmission electron microscopy (HR-TEM, JEM-3000F, JEOL) analysis was further performed to investigate the crystal structure of nanowires and the nanowire/substrate interface.

### **3.2.3. Results and discussion**

The field emission scanning electron microscopy (FESEM) image of as-grown SnO<sub>2</sub> nanowires on r-cut sapphire is shown in Figure 3.2.1(a). The tilted

view revealed that majority of the nanowires were vertically grown and a few nanowires were aligned with an inclination to the substrate (two different directions). The average diameter of nanowires was  $\sim 20$  nm and the length was  $\sim 1$   $\mu$ m. The growth rate in length direction was  $\sim 33$  nm $\cdot$ min $^{-1}$ . The density of nanowires was estimated to be  $\sim 45$  wires $\cdot$ m $^{-2}$ . The nanowires had the rectangular cross section (inset of Figure 3.2.1(a)). The out-of-plane orientation of SnO<sub>2</sub> nanowires on r-cut sapphire was investigated by X-ray diffraction (Figure 3.2.1(b)). The only (101) peak of SnO<sub>2</sub> (JCPDS Card No. 41-1445, space group: P4<sub>2</sub>/mnm, a=b=0.4738 nm, c=0.3187 nm) and {012} peaks of sapphire (JCPDS Card No. 46-1212, space group: R $\bar{3}$ c, a= b=0.4758 nm, c=1.2992 nm) were observed. This result indicates a strongly preferred (101) orientation of nanowires normal to the substrate even though as-grown SnO<sub>2</sub> nanowires exhibited the three different growth directions. The in-plane orientation of nanowires was examined by X-ray pole figure. The {001} pole figure of (012) sapphire and {101} pole figure of SnO<sub>2</sub> nanowires are shown in Figure 3.2.2 (a) and (b), respectively. Only reflections from {101} family of planes ((101), (0 $\bar{1}$ 1), ( $\bar{1}$ 01), (011)) appeared in the pole figure of SnO<sub>2</sub>, which exactly matched with the (101) stereographic projection of SnO<sub>2</sub> (Figure 3.2.2(d)). This implies that the SnO<sub>2</sub> nanowires were heteroepitaxially grown on r-cut sapphire and there exists in-plane orientation relationship between nanowires and sapphire. The determined in-plane relationships were  $[010]_{\text{SnO}_2} \parallel [100]_{\text{r-cut}}$  and  $[\bar{1}01]_{\text{SnO}_2} \parallel [12\bar{1}]_{\text{r-cut}}$ .

which are consistent with the previously reported epitaxial relationships of SnO<sub>2</sub> thin films.[73, 82]

Based on the heteroepitaxial relationships, the as-grown (101) SnO<sub>2</sub> nanowires were further examined by FESEM along the [100] and [12 $\bar{1}$ ] directions of r-cut sapphire (Figure 3.2.3). The cross-sectional images clearly showed the characteristic angular orientations (aligned direction) of the nanowires with respect to r-cut sapphire substrate. When viewed along the [100] direction of sapphire substrate (Figure 3.2.3(a)), majority of the nanowires were inclined at an angle of 68° to the substrate plane and a few nanowires had an inclination angle of 56°. Three aligned directions were evident when viewed along the [12 $\bar{1}$ ] direction of sapphire (Figure 3.2.3(b)). The major aligned direction was vertical to the surface, while the other two minor aligned directions were projected at an angle of 29° to the surface forming the mirror images. The observed growth directions and angles of (101) SnO<sub>2</sub> nanowires were consistent with those calculated from the rutile SnO<sub>2</sub> crystal structure (Figure 3.2.4). Indeed, the (101) SnO<sub>2</sub> nanowires exhibited the three different growth directions of [101], [011], and [0 $\bar{1}$ 1]. Au nanoparticles were found at the tips of all the nanowires indicating that SnO<sub>2</sub> nanowires were grown via a vapor-liquid-solid (VLS) mechanism.

TEM specimens were prepared using the focused ion beam (FIB) lift-out technique to further analyze the crystallographic growth directions and interfaces between nanowires and substrate.[95] The cross-sectional TEM images viewed along [100] direction of sapphire ([010] direction of SnO<sub>2</sub>) is shown in Figure 3.2.5. The low magnification, bright field image clearly showed the angular growth of SnO<sub>2</sub> nanowires (Figure 3.2.5(a)). The measured angle of 68° was consistent with FESEM observation. The nanowires had a nearly constant diameter of ~20 nm with a smooth surface. The slight bending of nanowires was introduced during the specimen preparation. The nanowires had the larger diameter (broadened) base. The reason is not well understood at this stage, but it could be formed by a surface tension acting on the Au droplet during VLS growth.<sup>46</sup> HRTEM image of nanowire (Figure 3.2.5(b)) demonstrated the clear lattice fringes without obvious defects or dislocations confirming the high single crystallinity of nanowires. The fast Fourier transformation (FFT) pattern (Figure 3.2.5(c)) of nanowire was completely indexed to rutile viewed along the [010] zone axis and the side wall of the nanowire was parallel to the ( $\bar{1}01$ ) plane. The FFT pattern of interface (Figure 3.2.5(d)) indicated that (101) plane of SnO<sub>2</sub> and (012) plane of sapphire were parallel confirming the orientation relationships of (101)<sub>SnO<sub>2</sub></sub>  $\parallel$  (012)<sub>r-cut</sub> and [010]<sub>SnO<sub>2</sub></sub>  $\parallel$  [100]<sub>r-cut</sub>, determined by XRD and X-ray pole figure. The growth direction of nanowires, angled 68° to the (101) plane, was determined to be [101]. Thus, the SnO<sub>2</sub> nanowires grew along the [101]

direction with an inclination angle of  $68^\circ$  to (101) plane. A high magnification image of the interfacial region (Figure 3.2.5(f)) revealed that the interface is clean. The  $(\bar{1}01)$  plane of  $\text{SnO}_2$  was connected to the  $(0\bar{1}4)$  plane of sapphire at the interface. The misfit dislocation can be easily seen in the Fourier filtered image (Figure 3.2.5(g)) and the misfit dislocation was rather irregular due to the roughness of the sapphire substrate. This misfit dislocation was resulted from the large lattice mismatch (11.09 %) in the  $[\bar{1}01]$  direction of  $\text{SnO}_2$  ( $[12\bar{1}]$  direction of sapphire).[82] In addition, the growth direction of the nanowires inclined at an angle of  $56^\circ$  to the substrate when viewed along the  $[100]$  direction of sapphire was determined to be  $[011]$  or  $[0\bar{1}1]$  (Figure 3.2.4), and these nanowires had the same hetero-epitaxial relationships with sapphire (Figure 3.2.6). From these observations, it can be concluded that the (101)  $\text{SnO}_2$  nanowires were hetero-epitaxially grown on the r-cut sapphire substrate without a distinct buffer layer.

The interface of Au catalyst and  $\text{SnO}_2$  nanowire was further investigated by TEM. The HRTEM image (Figure 3.2.7(a)) showed that semi-spherical, crystalline Au catalyst were present at the tip of nanowire and the interface was relatively sharp and straight. The FFT patterns of Figure 3.2.7(b) and (c), viewed along the  $[010]$  direction of  $\text{SnO}_2$  (or  $[101]$  direction of Au), were completely indexed to be Au and  $\text{SnO}_2$ , respectively, and the interface was parallel to the (101) plane of  $\text{SnO}_2$  (or (020) plane of Au).

The energy dispersive X-ray spectroscopy (EDS) analysis indicates that the nanoparticle on the tip was only composed of Au and no evidence of Sn and O was found (Figure 3.2.8). The presence of diffused Au atoms along the Si nanowire has been reported,[97] but Au was not detected along the SnO<sub>2</sub> nanowire within the detection limit of EDS. The interface between Au and SnO<sub>2</sub> was atomistically well defined (Figure 3.2.7) and the orientation relationships were found to be  $(020)_{\text{Au}} \parallel (101)_{\text{SnO}_2}$  and  $[101]_{\text{Au}} \parallel [010]_{\text{SnO}_2}$ . It was reported that the crystalline orientation of the catalyst might determine the growth direction and side surfaces of nanowires and nanobelts.[94] In this study, the crystallographic orientation of SnO<sub>2</sub> nanowire was primarily determined by the hetero-epitaxial relationships with sapphire and thus, the influence of Au catalyst on the growth behavior of SnO<sub>2</sub> nanowire is less likely.

In addition, when the Ar gas flow rate increased from 300 to 500 sccm, the growth rate of SnO<sub>2</sub> nanowires increased from 33 to 56 nm·min<sup>-1</sup>, and the nanowires having several branches at upper part appeared. The branches were not obviously observed in SEM micrograph (Figure 3.2.9(a)), but they were clearly seen in TEM micrographs (Figure 3.2.9(b) and (c)). Surprisingly, the branch nanowires had an inclination angle of 68 ° to the original nanowire (trunk) grown on sapphire substrate. The branch nanowire even had a secondary branch, which

was parallel to the trunk nanowire. The FFT patterns of trunk nanowire (c,d), branch nanowire (f), and interface region (e) marked in Figure 3.2.9 were exactly matched one another, and the HRTEM image showed that the lattice fringes were continued across the interface between trunk and branch nanowires. These results implies that the branch nanowires were homo-epitaxially grown (101) SnO<sub>2</sub> nanowires with <101> family growth directions. Each growth direction was presented in Figure 3.2.9(a). The branch nanowires had the similar diameters to the trunk nanowire with the broadened bases, and Au catalyst was frequently observed at the tip (Figure 3.2.9(h) and (i)). The branched nanowires have been achieved via a controlled multistep catalyst mediated VLS process in many systems.[88, 90] However, in this study, the branched nanowires were obtained in one step without a multiple catalyst deposition just by changing the Ar flow rate.

### **3.2.4. Conclusion**

In summary, well-aligned (101) SnO<sub>2</sub> nanowires were fabricated on r-cut sapphire by carbothermal reduction via Au-catalyzed heteroepitaxial growth. Epitaxially grown (101) SnO<sub>2</sub> nanowires exhibited three angular growth directions with different inclination angles to the substrate due to a tetragonal crystal structure. The orientation relationship between Au catalyst and SnO<sub>2</sub>

nanowire was determined by TEM, but the effect of catalyst on the growth behavior of SnO<sub>2</sub> nanowire was unlikely. The branched SnO<sub>2</sub> nanowires were developed on the vertically aligned trunk nanowires just by changing the growth conditions. The branched nanowires were homo-epitaxially grown on the trunk nanowires and thus, they were (101) SnO<sub>2</sub> nanowires with <101> growth directions.

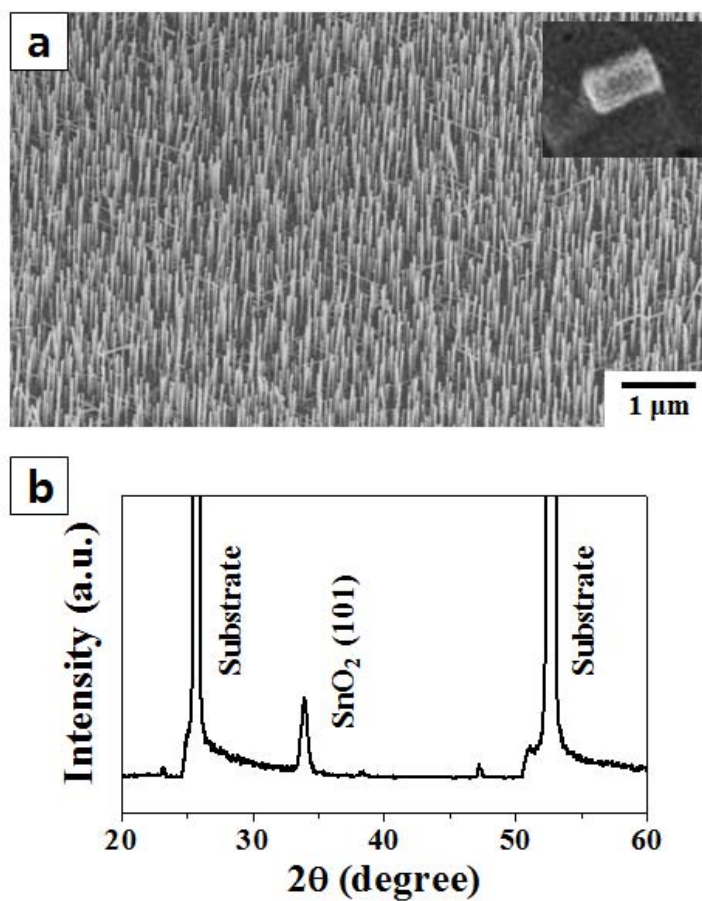


**Figure 3.2.1.** (a) Tilted FESEM image of aligned SnO<sub>2</sub> nanowires grown on r-cut sapphire. The inset is the cross-sectional view of individual nanowire. (b)  $\theta$ - $2\theta$  X-ray diffraction of SnO<sub>2</sub> nanowires.

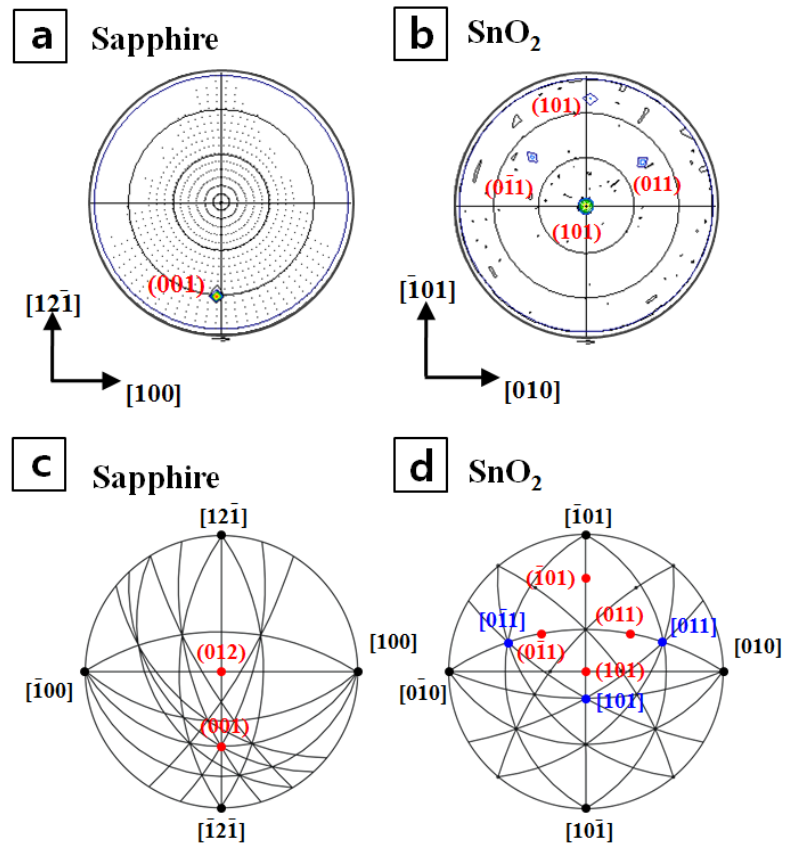


**Figure 3.2.2.** (a)  $\{001\}$  pole figure of (012) sapphire substrate. (b)  $\{101\}$  pole figure of SnO<sub>2</sub> nanowires at 33.89 ° Bragg angle. Stereographic projection of (c) (012) sapphire and (d) (101) SnO<sub>2</sub>.

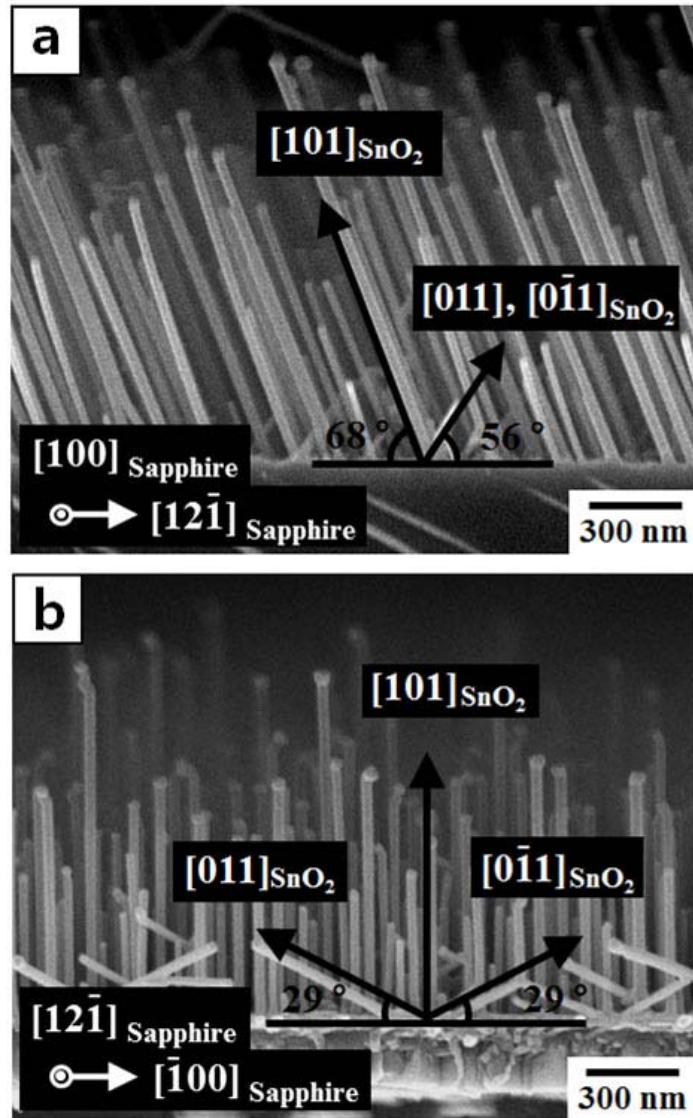


**Figure 3.2.3.** Cross-sectional FESEM images of aligned SnO<sub>2</sub> nanowires grown on r-cut sapphire; (a) viewed along the [100] direction and (b) viewed along the [12 $\bar{1}$ ] direction of r-cut sapphire.

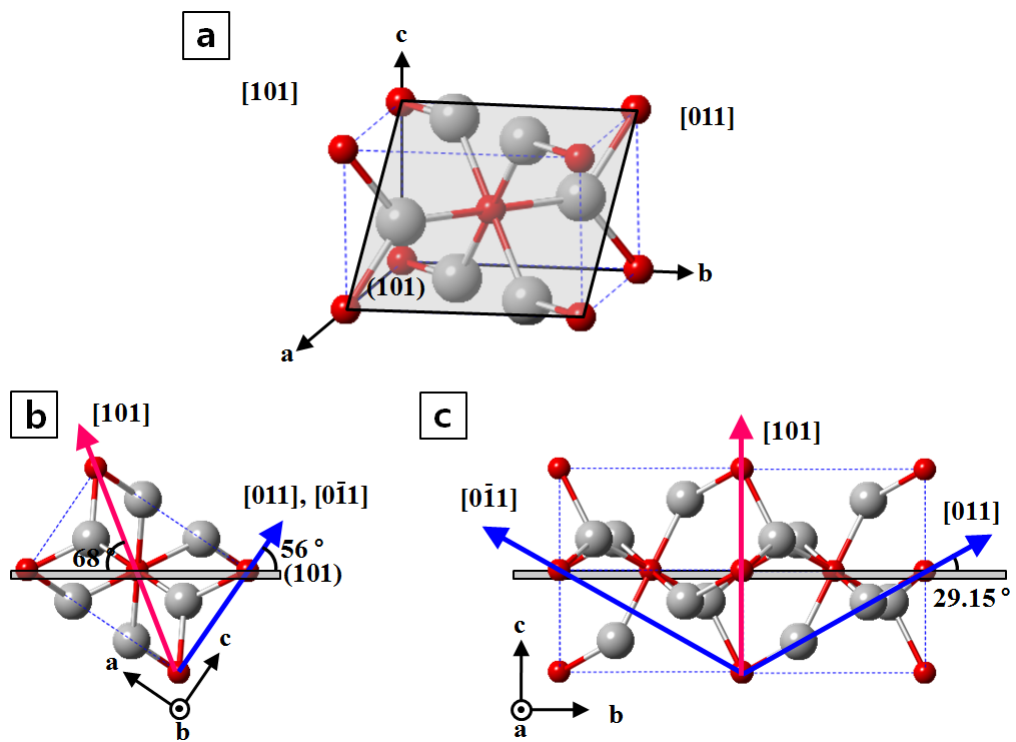


**Figure 3.2.4.** (a) Crystal structure of rutile SnO<sub>2</sub>. The <101> family directions of SnO<sub>2</sub> viewed along the (a) [010] and (b) [100] direction.

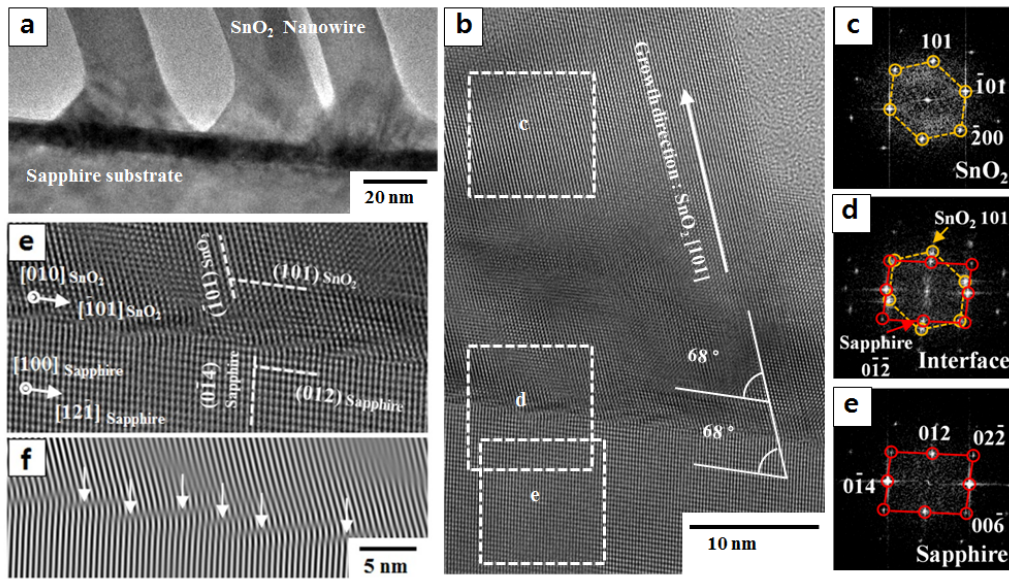


**Figure 3.2.5.** (a) Cross-sectional TEM image of (101) SnO<sub>2</sub> nanowires grown on sapphire ([101] growth direction). (b) HRTEM image of a SnO<sub>2</sub> nanowire on sapphire. Incident beam is in the [100] direction of sapphire. (c), (d), and (e) FFT patterns of SnO<sub>2</sub> nanowire, interface, and sapphire substrate marked by the boxes in panel (b), respectively. (f) high-magnification image of SnO<sub>2</sub>/sapphire interface. (g) Fourier filtered image of (f).

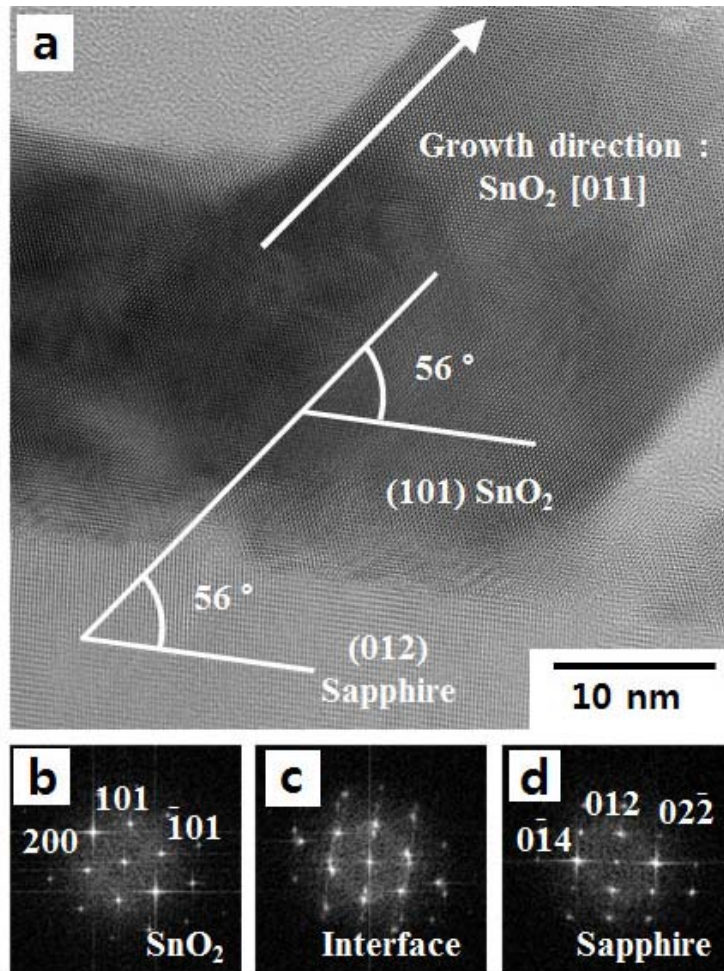


**Figure 3.2.6.** (a) Cross-sectional TEM image of (101) SnO<sub>2</sub> nanowire on sapphire ([011] growth direction). (b), (c), and (d) FFT patterns of SnO<sub>2</sub> nanowire, interface, and sapphire, respectively.

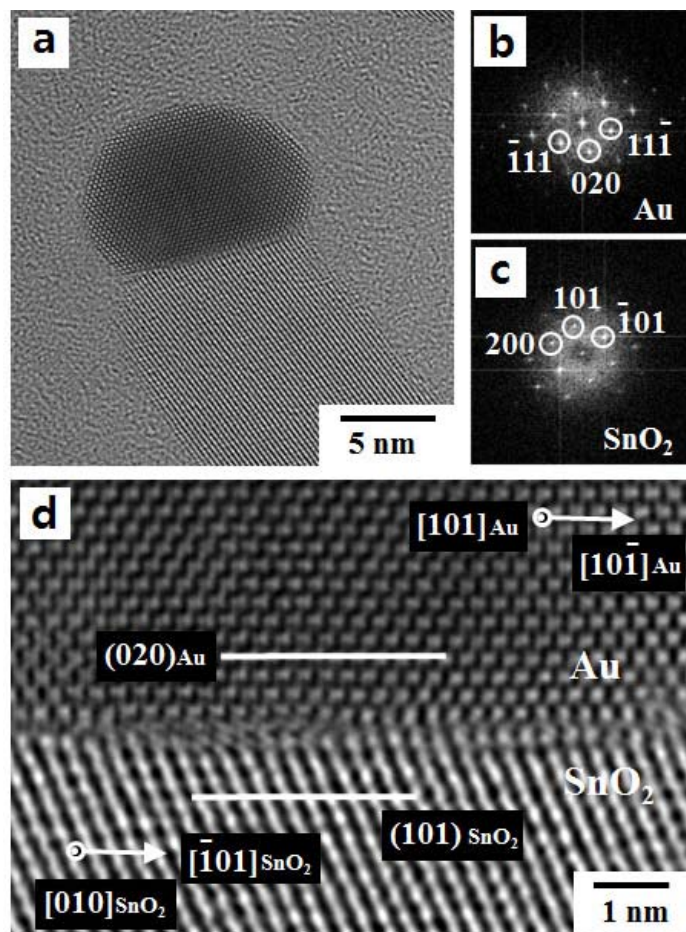


**Figure 3.2.7.** (a) HRTEM image of Au catalyst at the tip of SnO<sub>2</sub> nanowire. (b) and (c) FFT patterns of Au catalyst and SnO<sub>2</sub> nanowire, respectively. (d) high magnification image of Au/SnO<sub>2</sub> interface.

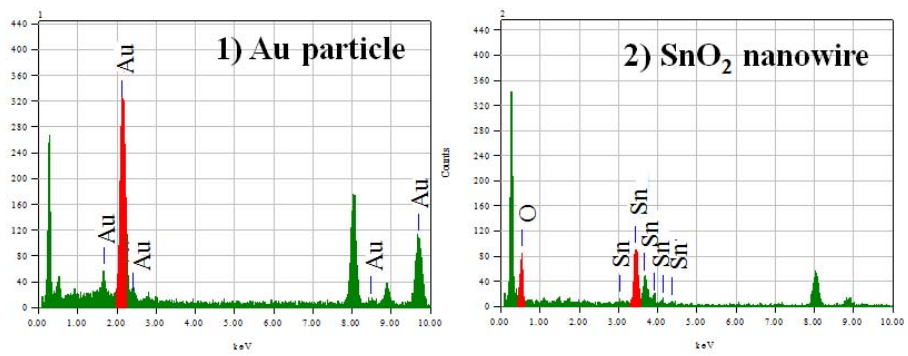
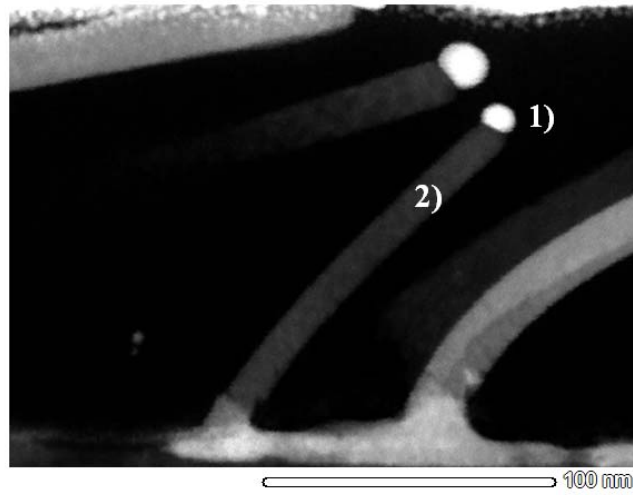


**Figure 3.2.8.** EDS spectra of Au catalyst and SnO<sub>2</sub> nanowire.

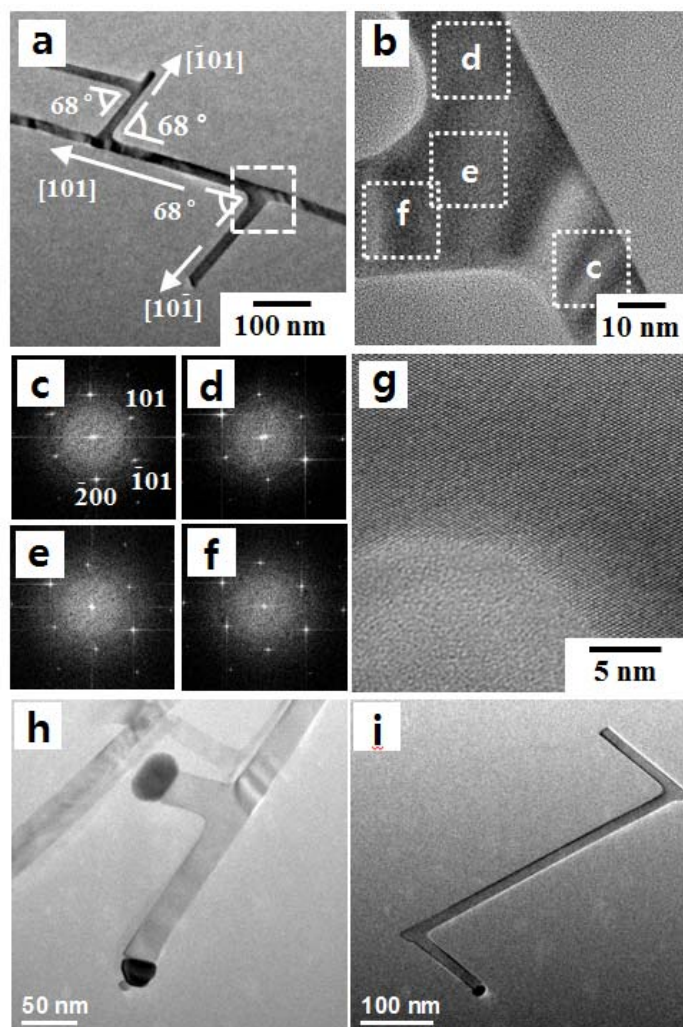


**Figure 3.2.9.** (a) and (b) TEM images of branched SnO<sub>2</sub> nanowires. (c)-(f) FFT patterns of nanowires marked by the boxes in panel (b). (g) HRTEM image of nanowire junction. (h) and (i) TEM images of branched SnO<sub>2</sub> nanowires with Au catalyst.

### **3.3. Horizontal growth of SnO<sub>2</sub> nanowire with one-directional Alignment**

#### **3.3.1. Introduction**

As the conventional microelectronic industry approaches its technological and financial limitations, new advanced devices based on inorganic nanowires (NWs) have received extensive attention as one of the next-generation device architectures. According to this trend, wafer-scale integration of nanowire with well-alignment has been intensively investigated for high operation reliability of nanowire based devices. As mentioned in the chapter 1, ex-situ alignment techniques are mostly complicated and nanowires might be contaminated by solvents during these process. So, in-situ alignment of nanowire during growth is a one of key technique for desirable nanowire-based device.

In this chapter, horizontally grown SnO<sub>2</sub> nanowires with self-alignment will be discussed. The synthesis condition of the horizontally grown SnO<sub>2</sub> nanowire is similar to the vertically grown SnO<sub>2</sub> nanowire. In this case, Au nanoparticle colloid is used as catalyst for VLS growth, because the distance between catalyst could be altered by controlling concentration of Au colloid. The horizontal growth of SnO<sub>2</sub> nanowire is synthesized by using r-cut sapphire

substrate and the SnO<sub>2</sub> nanowire is grown on r-cut sapphire substrate and a epitaxial relationship between nanowire and substrate is the same to vertically grown SnO<sub>2</sub> nanowires.

### **3.3.2. Experimental procedure**

*1) Preparation of Au coated substrate:* For the horizontal growth SnO<sub>2</sub> nanowire, the Au was deposited by using Au colloid. The cleaned substrate was immersed in Poly-L-lysine (PLL, 10 wt. %) solution for 2 min, and washed by D. I. water. After that, Au colloid was dispersed on PLL. The colloids were immobilized on the surface modified substrate. A thin layer of polyelectrolyte adsorbed onto the substrate surface by a quick immersion in 0.1 wt % poly-L-lysine. After rinsing with DI water, the substrates were immersed in the Au nanoparticle solution (1010-1011 particles/mL, Ted Pella Inc.). The polymer possesses a net positive charge in aqueous solution at neutral pH and hence adsorbs onto the substrate due to its electrostatic attraction to deprotonated hydroxyl groups on surface of substrate. Consequently the polymer film presents a positively charged surface to the negatively charged Au colloids in aqueous solution, attracting them to the surface. Following a final rinse with DI water and drying, the substrates were used for nanowire growth in tube furnace.

**2) Nanowire growth condition:** For SnO<sub>2</sub> nanowire synthesis, the feedstock source was prepared by thoroughly mixing SnO<sub>2</sub> powder (purity 99.99%) and graphite (purity 99.99%) in a 2:1 ratio. The feedstock was loaded into an alumina boat and placed 7 cm upstream from the Au-coated substrate in a quartz tube. The quartz tube was then inserted into a horizontal tube furnace and evacuated by a rotary pump to a pressure of  $5 \times 10^{-2}$  torr. The furnace was heated to 800 °C at a heating rate of 10 °C/min and maintained at that temperature for 30 min under a constant Ar gas flow (300 sccm) at a total pressure of 10 torr. After deposition, the furnace was cooled to room temperature and the samples were retrieved and characterized.

**3) Characterization:** The morphology of as-synthesized product was observed by field-emission scanning electron microscopy (FE-SEM, JSM-7401F, JEOL). The phase and in- and out of-plane orientation relationships between nanowires and substrate were examined by X-ray diffraction (XRD) and X-ray pole figure (X'Pert Pro, PANalytical). High-resolution transmission electron microscopy (HR-TEM, JEM-3000F, JEOL) analysis was further performed to investigate the crystal structure of nanowires and the nanowire/substrate interface.

### 3.3.3. Results and discussion

Figure 3.3.1 is SEM images of as grown SnO<sub>2</sub> nanowires catalyzed using 50 nm sized Au nanoparticle. All of nanowires are aligned with and one-direction, and it is [10 $\bar{1}$ ] or [ $\bar{1}$ 01] direction of SnO<sub>2</sub> and [12 $\bar{1}$ ] or [ $\bar{1}$ 2 $\bar{1}$ ] of sapphire (Figure 3.3.1(a)). The nanowire exhibits the quite uniform diameter and it indicates that the Au nanoparticles were well-dispersed and the aggregation of Au is not occurred during heating process. The periodical nodes are interestingly observed in Figure 3.3.1(b). And tilted view of SEM image shows the thickness of nanowire is thinner than the diameter of nanowire and a top surface of nanowire is not flat.

The out-of-plane orientation of lateral grown SnO<sub>2</sub> nanowires on r-cut sapphire substrate was investigated by X-ray diffraction (Figure 3.3.2). Only reflections from the {101} family of planes ((101), ( $\bar{1}$  01), (011), (0 $\bar{1}$  1)) appeared in pole figures for horizontally grown SnO<sub>2</sub> nanowires. This indicates that SnO<sub>2</sub> (101) nanowires were epitaxially grown on r-cut sapphire substrate with in-plane relationships of  $[0\bar{1}0]_{\text{SnO}_2} \parallel [02\bar{1}]_{\text{sapphire}}$  and  $[\bar{1}01]_{\text{SnO}_2} \parallel [12\bar{1}]_{\text{sapphire}}$ . Thus, the obtained SnO<sub>2</sub> nanowires were heteroepitaxially grown on r-cut sapphire substrate similar to heteroepitaxial SnO<sub>2</sub> films and vertically aligned

SnO<sub>2</sub> nanowire. The growth direction of SnO<sub>2</sub> nanowire with orientation of sapphire is already index in Figure 3.3.1. In case of lateral grown SnO<sub>2</sub> nanowire, this relationship is an unexpected result because horizontal nanowire is grown along large lattice mismatch direction (11.24%,  $[\bar{1}01]//[12\bar{1}]$ ).

In other studies, the horizontal growth of nanowire is induced by various approach, epitaxial relationship, faceted surface (on mis-cut substrate), and corrugated surface, and the growth direction of nanowire could be controlled their relationships.[98-100] Recently, it is investigated that growth direction and growth mode (vertical and horizontal growth) of noble metal nanowire could be steered by flux direction of supply.[101] We investigated the growth direction with different gas supply direction, as well. As seen Figure 3.3.3, the substrate was position with different angle to injection direction, but nanowire is grown according to substrate orientation instead of following the flux direction. So it is concluded that the flux direction does not affect to the growth direction of nanowire and the growth of SnO<sub>2</sub> nanowire is controlled by thermodynamic condition of SnO<sub>2</sub> nanowire.

To further investigate the morphology of nanowire and the interface between nanowires and substrate, cross sectional TEM specimens were prepared

using the focused ion beam (FIB) lift-out technique. The cross-sectional TEM image viewed along [100] direction of sapphire substrate is shown in Figure 3.3.4. The interesting cross section TEM image is the formation of periodical sawtooth-facet, the morphological instability. The rough surface and periodical nodes, observed in SEM images, is well-corresponded to cross-sectional TEM images. The SAED pattern of nanowire and sapphire exhibits the nanowire is hetero-epitaxially grown on sapphire but lots of deformations are observed at the interface of nanowire and substrate. Even though some of defect exists at the interface, the specific defect was not observed at the body of nanowire.

The cross-sectional TEM analysis according to the growth direction of nanowire is investigated as well. The (101) and (020) side facet of nanowire is clearly shown in Figure 3.3.5. The lattice of nanowire and sapphire is well-matched due to small lattice mismatch. While clear lattice fringe is observed in Figure 3.3.5(e), some of lattice distortion is observed at the body of nanowire (Figure 3.3.5(f)) even though it seems not to form the dislocation or planar defects.

The growth behavior of SnO<sub>2</sub> nanowire with different catalyst size is shown in Figure 3.3.6. The size of Au catalyst is 5nm, 20 nm and 80 nm,

respectively. It is directly observed that the SnO<sub>2</sub> nanowire is more snaked with decreasing catalyst size. It has been known that the size of Au catalyst affects to the growth mode and behavior of horizontal nanowire. When the increasing of Au catalyst size, the horizontal nanowire become disordered (loss their alignment) and the larger sized catalyst leads to transformation from horizontal to vertical growth. This is resulted by strain at interface between nanowire and substrate. Generally for using smaller sized catalyst, the strain is also small so nanowire growth is determined by underlying substrate. When the Au catalyst size becomes larger, the strain is large enough to overcome the direct influence of substrate, so the nanowire might be randomly grown or vertically grown. However, the horizontally grown SnO<sub>2</sub> nanowires show the counteracting to previous results. In our case, horizontal nanowire is straighten and well-aligned with increasing catalyst size. Interestingly, horizontal SnO<sub>2</sub> nanowires are a tendency to grow according to  $[1\bar{2}1]$  of sapphire in whole cases, even though the nanowire is getting loss their alignment with decreasing catalyst size.

In this study, we use the catalyst as Au colloids for control of spacing between Au particles and density. Au nanoparticle is randomly located on substrate, as the result the further length control is difficult. So we use pattern Au thin film as catalyst to synthesis of ultra-long horizontal SnO<sub>2</sub> nanowire. As

expected, the large amount of vertically grown SnO<sub>2</sub> nanowire is observed in high density region of Au catalyst and the horizontally grown SnO<sub>2</sub> nanowire is shown at the edge of Au pattern (Figure 3.3.7). The length of nanowire is more than 10 μm with well-alignment, as well.

We additionally investigated the transformation from lateral to vertical growth, as well. Even though it is well-known that high density of Au catalyst leads to vertical (or perpendicular) growth, the procedure, toward vertical growth, has not been demonstrated. We could successfully observe the transformation progress by using Au thin film as catalyst for high density nanodots array. Figure 3.3.8 shows the transformation behavior from lateral to vertical growth. In the initial state, Au thin film turns to the randomly distributed Au nanodots and the horizontal nanowire is grown when gas feeding is supplied. In this state, horizontal nanowire is randomly grown because near Au catalyst disturbs their preferred alignment. When collision of the horizontal nanowire is occurred, the nanowire is not horizontally grown any more. And the nanowire is vertically grown, finally. In our previous works, we show the hetero-epitaxial relationship and the specific growth behavior, angular growth of SnO<sub>2</sub> nanowire. This results indicates that the horizontal nanowire of initial state is also followed the hetero-

epitaxial relationship, even though they seem to be grown with random growth direction.

### **3.3.4. Conclusion**

The SnO<sub>2</sub> nanowires are horizontally grown on r-cut sapphire with self-alignment by Au-catalyzed thermal evaporation. The results of pole-figure indicate the nanowires are epitaxially grown and the growth direction of  $[10\bar{1}]$  is parallel to the large mismatch direction with r-cut sapphire. The upper facet of nanowire shows surface roughening while the side facet is flat. This might be result from large lattice mismatch between SnO<sub>2</sub> nanowire and r-cut sapphire. The further studies about growth behavior of SnO<sub>2</sub> nanowire and the surface roughening will be conducted.

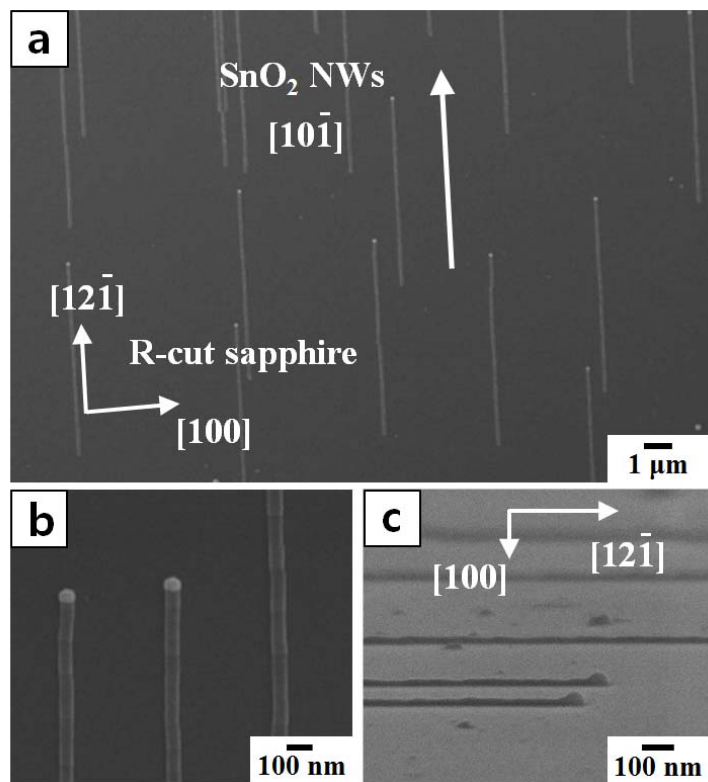


**Figure. 3.3.1.** SEM images of horizontally grown SnO<sub>2</sub> nanowire.

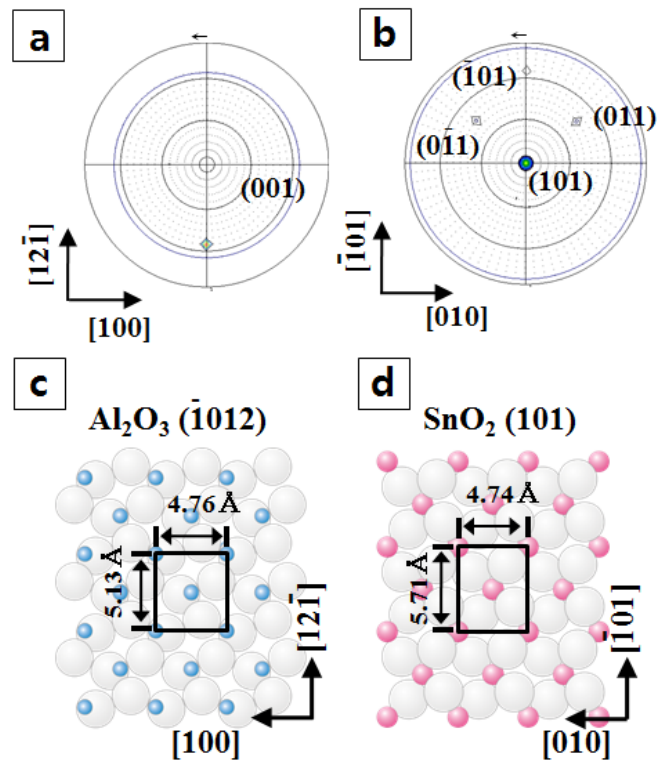


**Figure 3.3.2.** (a)  $\{001\}$  pole figure of (012) sapphire substrate. (b)  $\{101\}$  pole figure of  $\text{SnO}_2$  nanowires at  $33.89^\circ$  Bragg angle. Crystal structure of (c) (012) sapphire and (d) (101)  $\text{SnO}_2$ .

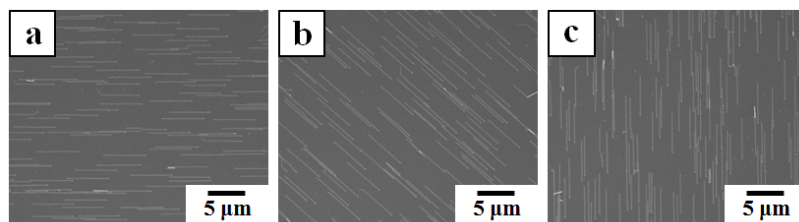
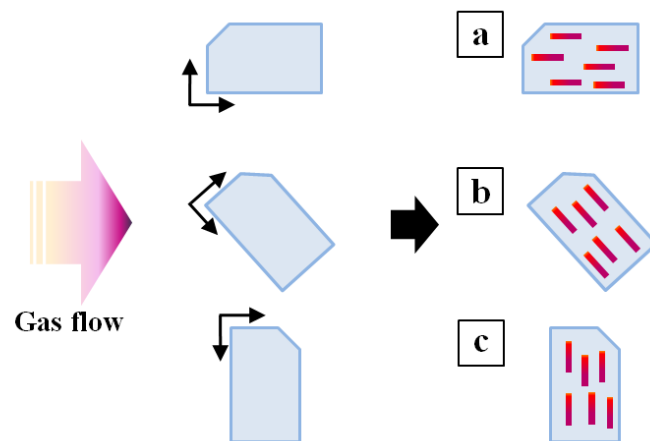


**Figure 3.3.3.** The growth of horizontal SnO<sub>2</sub> nanowire with different direction of gas injection.

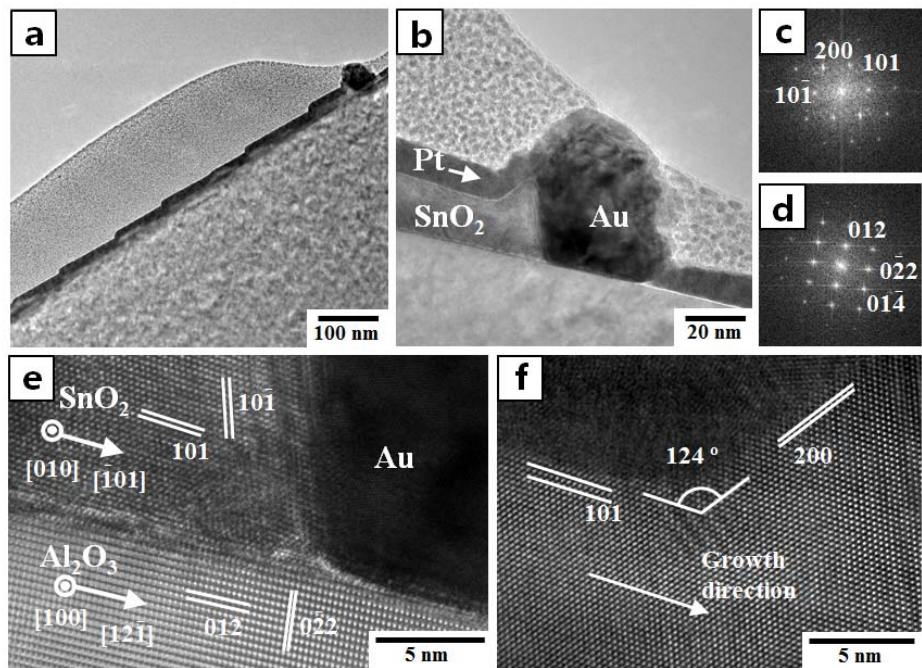


**Figure 3.3.4.** Cross-sectional TEM image with [010] zone axis of SnO<sub>2</sub>.

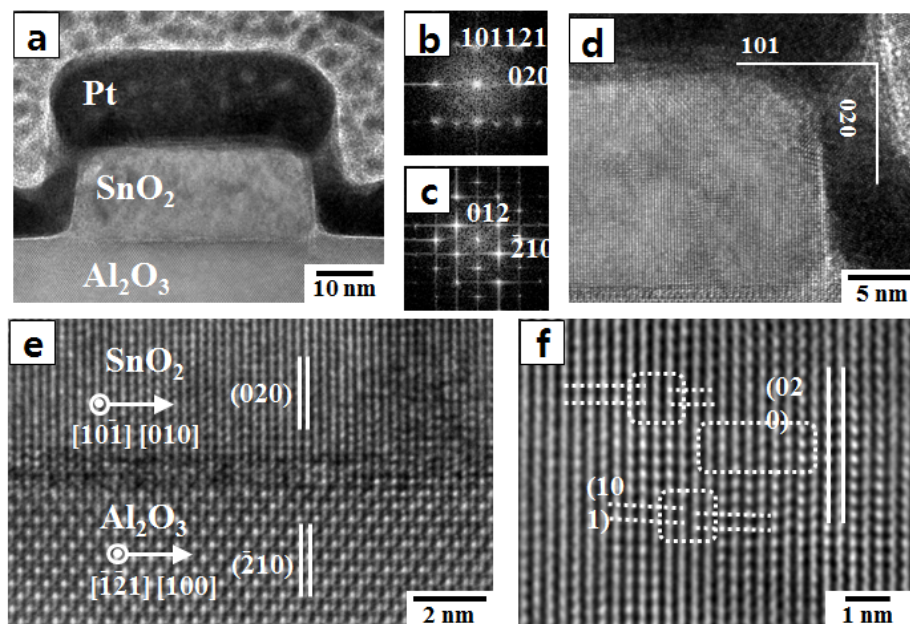


**Figure 3.3.5.** Cross-sectional TEM image with  $[\bar{1}01]$  zone axis of  $\text{SnO}_2$ .

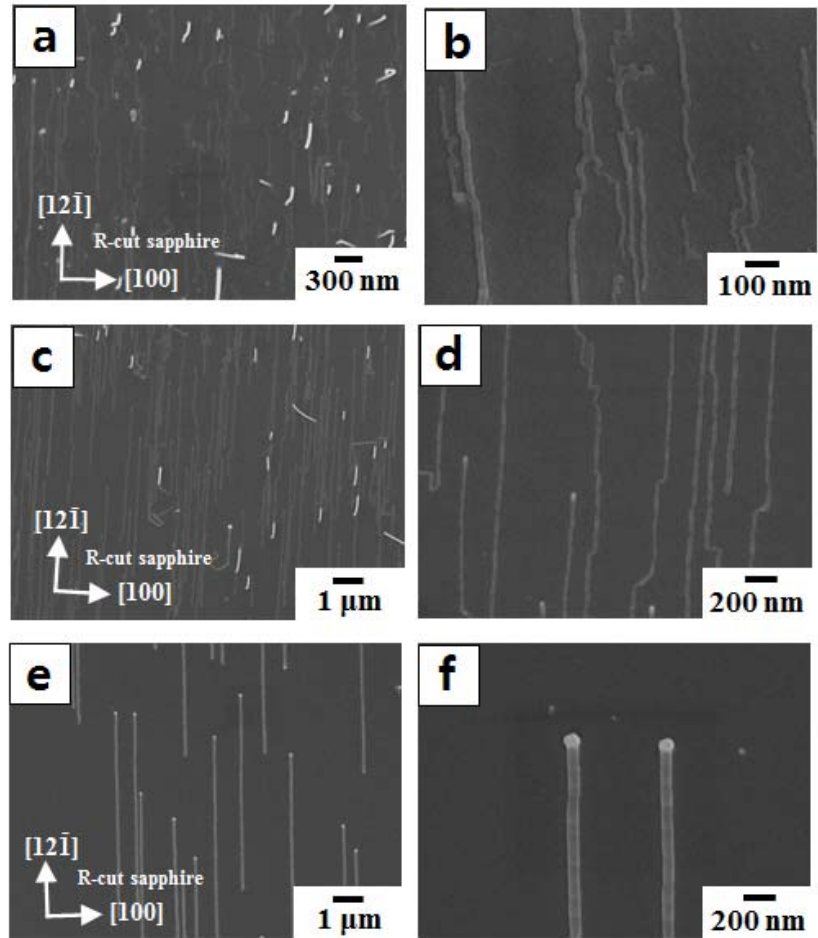


**Figure 3.3.6.** The horizontally grown SnO<sub>2</sub> nanowire with different catalyst size, (a) and (b) : 5 nm, (c) and (d) : 20 nm, (e) and (f) 80 nm.

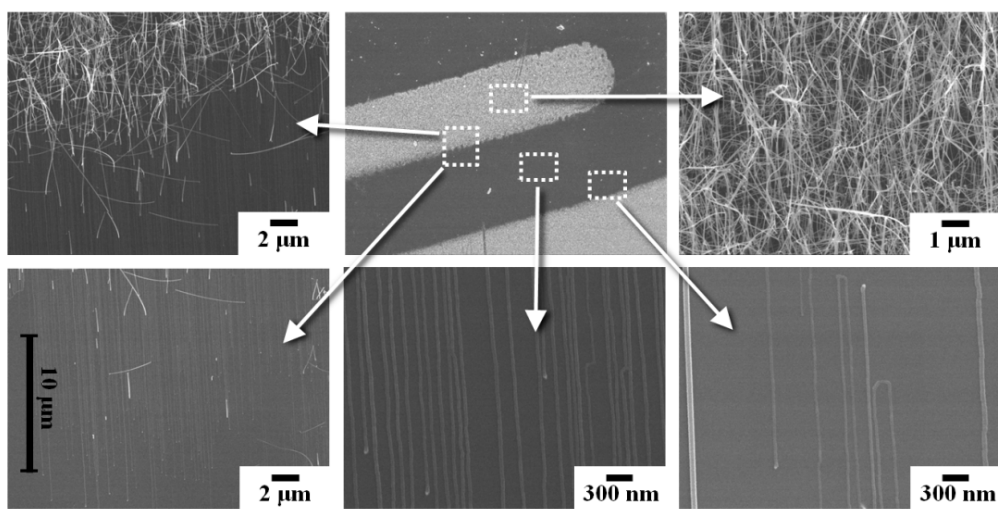


**Figure 3.3.7.** Ultra-long, horizontally grown SnO<sub>2</sub> nanowire from patterned Au thin-film.

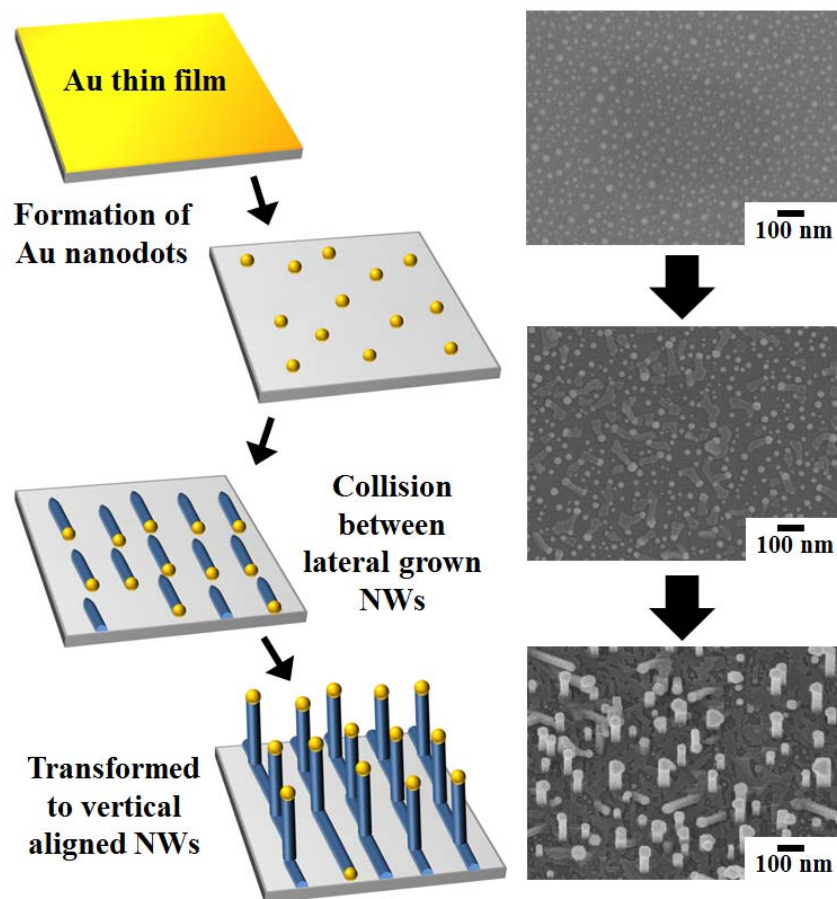


**Figure 3.3.8.** Transformation of growth behavior of SnO<sub>2</sub> nanowire from horizontal to vertical growth.

### 3.4. Reference

- (1) Ç. Kılıç Ç, A. Zunger, Phys. Rev. Lett. 2002, 88, 095501.
- (2) J. –H. Jeun, H. –S. Ryu, S. –H. Hong, J. Electrochem. Soc. 2009, 156, J263-J266.
- (3) C. S. Moon, H. –R. Kim, G. Auchterlonie, J. Drennan, J. –H. Lee, Sens. Actuators B, 2008, 131, 556-564.
- (4) T. Mochida, K. Kikuchi, T. Kondo, H. Ueno, Y. Matsuura, Sens. Actuators B, 1995, 25, 433-437.
- (5) J. Santos, P. Serrini, B. O’Beirn, L. Manes, Sens. Actuators B, 1997, 43, 154-160.
- (6) Y. Zhang, X. He, J. Li, Z. Miao, F. Huang, Sens. Actuators B, 2008, 132, 67-73.
- (7) G. X. Wang, J. S. Park, M. S. Park, X. L. Gou Sens. Actuators B, 2008, 131, 313-317
- (8) J. Huang, N. Matsunaga, K. Shimano, N. Yamazoe, T. Kunitake, Chem. Mater. 2005, 17, 3513-3518.
- (9) O. K. Varghese, D. Gong, M. Paulose, K. G. Ong, E. C. Dickey, C. A. Grimes, Adv. Mater. 2003, 15, 624-627.

- (10) W. -Y. Li, L. -N. Xu, J. Chen, *Adv. Funct. Mater.* 2005, 15, 851-857.
- (11) Y. Liu, M. Liu, *Adv. Funct. Mater.* 2005, 15, 57-62.
- (12) Z. Li, H. Wang, P. Liu, B. Zhao, Y. Zhang, *Appl. Surf. Sci.* 2009, 255, 4470-4473.
- (13) B. Liu, H. C. Zeng, *J. Phys. Chem. B* 2004, 108, 5867-5874.
- (14) Y. Wang, J. Y. Lee, H. C. Zeng, *Chem. Mater.* 2005, 17, 3899-3903.
- (15) W. Zhu, W. Wang, H. Xu, J. Shi, *Mater. Chem. Phys.* 2006, 99, 127-130.
- (16) Y. Wang, M. Wu, Z. Jiao, J. Y. Lee, *Nanotechnology* 2009, 20, 345704.
- (17) M. Lai, J. -H. Lim, S. Mubeen, Y. Rheem, A. Mulchandani, M. A. Deshusses, N. V. Myung, *Nanotechnology*, 2009, 20, 185602.
- (18) S. -H. Chou, J. -Z. Wang, H. -K. Liu, S. -X. Dou, *Electrochem. Commun.* 2009, 11, 242-246.
- (19) S. -W. Choi, J. Y. Park, S. S. Kim, *Nanotechnology*, 2009, 20, 465603.
- (20) X. Song, L. Liu, *Sens. Actuators A*, 2009, 154, 175-179.
- (21) Z. Liu, D. D. Sun, P. Guo, J. O. Leckie, *Nano Lett.* 2007, 7, 1081-1085.
- (22) H. -W. Lu, D. Li, K. Sun, Y. -S. Li, Z. -W. Fu, *Solid State Sci.* 2009, 11,

982-987.

(23) M. Y. Song, D. K. Kim, K. J. Ihn, S. M. Jo, D. Y. Kim, *Nanotechnology*, 2004, 15, 1861-1865.

(24) Q. Peng, X. -Y. Sun, J. C. Spagnola, G. K. Hyde, R. J. Spontak, G. N. Parsons, *Nano Lett.* 2007, 7, 719-722.

(25) G. -M. Kim, S. -M. Lee, G. H. Michler, H. Roggendorf, U. Gösele, M. Knez, *Chem. Mater.* 2008, 20, 3085-3091.

(26) Q. Peng, X. -Y. Sun, J. C. Spagnola, C. Saquing, S. A. Khan, R. J. Spontak, G. N. Parsons, *ACS Nano*, 2009, 3, 546-554.

(27) E. Santala, M. Kemell, M. Leskelä, M. Ritala, *Nanotechnology*, 2009, 20, 035602.

(28) Y. Qiu, J. Yu, C. Tan, J. Yin, X. Zhou *Chem. Lett.* 2008, 37, 1114-1115.

(29) M. Bognitzki, H. Hou, M. Ishaque, T. Frese, M. Hellwig, C. Schwarte, A. Schaper, J. H. Wendorff, A. Greiner, *Adv. Mater.* 2000, 12, 637-640.

(30) Choi G, Satyanarayana L, Park J *Appl. Surf. Sci.* 2006, 252, 7878-7883.

(31) A. Rosental, A. Tarre, A. Gerst, J. Sundqvist, A. Härsta, A. Aidla, J. Aarik, V. Sammelselg, T. Uustare, *Sens. Actuators B*, 2003, 93, 552-555.

- (32) H. Virola, L. Niinistö, *Thin Solid Films*, 1994, 249, 144-149.
- (33) A. Tarre, A. Rosental, J. Sundqvist, A. Hårsta, T. Uustare, V. Sammelseg, *Surf. Sci.* 2003, 532-535, 514-518.
- (34) E. Fitzer, W. Frohs, M. Heine, *Carbon*, 1986, 24, 387-395.
- (35) H. Hou, J. J. Ge, J. Zeng, Q. Li, D. H. Reneker, A. Greiner, S. Z. D. Cheng, *Chem. Mater.* 2005, 17, 967-973.
- (36) T. Sahm, L. Mädler, A. Gurlo, N. Barsan, S. E. Pratsinis, U. Weimar, *Sens. Actuators B*, 2004, 98, 148-153.
- (37) X. L. Yu, Y. Wang, H. L. W. Chan, C. B. Cao, *Microporous Mesoporous Mater.* 2009, 118, 423-426.
- (38) C. Xiangfeng, W. Caihong, J. Dongli, Z. Chenmou, *Chem. Phys. Lett.* 2004, 399, 461-464.
- (39) I. Alessandri, E. Comini, E. Bontempi, C. Faglia, L. E. Depero, G. Sberveglieri, *Sens. Actuators B*, 2007, 128, 312-319.
- (40) Z. Yang, L. -M. Li, Q. Wan, Q. -H. Liu, T. -H. Wang, *Sens. Actuators B*, 2008, 135, 57-60.
- (41) L. Xi, D. Qian, X. Tang, C. Chen, *Mater. Chem. Phys.* 2008, 108, 232-236.

- (42) H. -C. Chiu, C. -S. Yeh, *J. Phys. Chem. B*, 2007, 111, 7256-7259.
- (43) Z. Ying, Q. Wan, Z. T. Song, S. L. Feng, *Nanotechnology*, 2004, 15, 1682-1684.
- (44) N. V. Hieu, H. -R. Kim, B. -K. Ju, J. -H. Lee, *Sens. Actuators B*, 2008, 133, 228-234.
- (45) K. -M. Li, Y. -J. Li, M. -Y. Lu, C. -I. Kuo, L. -J. Chen, *Adv. Funct. Mater.* 2009, 19, 2453-2456.
- (46) D. Wang, J. Xu, Q. Pan, *Chem. Lett.* 2008, 37, 1086-1087.
- (47) C. Xu, J. Tamaki, N. Miura, N. Yamazoe, *Sens. Actuators B*, 1991, 3, 147-155.
- (48) J. -H. Lee, *Sens. Actuators B*, 2010, 140, 319-336.
- (49) Y. K. Fang, J. J. Lee, *Thin Solid Films*, 1989, 169, 51-56
- (50) S. G. Ansari, P. Boroojerdian, S. R. Sainkar, R. N. Karekar, R. C. Aiyer, S. K. Kulkarni, *Thin Solid Films*, 1997, 295, 271-276.
- (51) A. Lugstein, M. Steinmair, C. Henkel and E. Bertagnolli, *Nano Lett.*, 2009, 9 , 1830-1834.
- (52) X. -M. Zhang, M. -Y. Lu, Y. Zhang, L. -J. Chen and Z. L. Wang, *Adv. Mater.*

2009, 21, 2767–2770.

(53) K. Peng, X. Wang and S. -T. Lee, *Appl. Phys. Lett.*, 2008, 92, 163103.

(54) M. -P. Lu, J. Song, M. -Y. Lu, M. -T. Chen, Y. Gao, L. -J. Chen and Z. L. Wang, *Nano Lett.*, 2009, 9 (3), 1223-1277.

(55) C. K. Chan, H. Peng, G. Liu, K. McIlwrath, X. F. Zhang, R. A. Huggins and Y. Cui, *Nature Nanotechnology*, 2008, 3, 31 – 35.

(56) G. Yuan, H. Zhao, X. Liu, Z. S. Hasanali, Y. Zou, A. Levine and D. Wang, *Angew. Chem.*, 2009, 121, 9860-9864.

(57) Y. Liang, H. Xu and S. K. Hark, *J. Phys. Chem. C*, 2010, 114, 8343–8347.

(58) Y. K. A. Lau, D. J. Chernak, M. J. Bierman and S. Jin, *J. Mater. Chem.*, 2009, 19, 934–940.

(59) Y. Sierra-Sastre, S. A. Dayeh, S. T. Picraux, and C. A. Batt, *ACS Nano*, 2010, 4 (2), 1209-1217.

(60) Ç. Kılıç, A. Zunger, *Phys. Rev. Lett.*, 2002, 88, 095501.

(61) Y. -X. Yin, L. -Y. Jiang, L. -J. Wan, C. -J. Li and Y. -G. Guo, *Nanoscale*, 2011, 3, 1802-1806.

(62) L. Li, J. Huang, T. Wang, H. Zhang, Y. Liu, J. Li, *Biosensors and*

Bioelectronics, 2010, 25, 2436–2441.

(63) A. Klamchuen, T. Yanagida, K. Nagashima, S. Seki, K. Oka, M. Taniguchi and T. Kawai, *Appl. Phys. Lett.*, 2009, 95, 053105.

(64) E. N. Dattoli, Q. Wan, W. Guo, Y. Chen, X. Pan, W. Lu, *Nano Lett.*, 2007, 7 (8), 2463-2469.

(65) Y. Han, X. Wu, Y. Ma, L. Gong, F. Qu and H. Fan, *CrystEngComm*, 2011, 13, 3506-3510.

(66) S. Supothina, R. Rattanakam, S. Vichaphund and P. Thavorniti, *J. European Cer.*, 2011, 31, 2453–2458.

(67) X. Wua, J. Suia, W. Caia, F. Qub, *Mater. Chem. Phys.*, 2008, 112, 325–328.

(68) W. -S. Kim, B. -S. Lee, D. -H. Kim, H. -C. Kim, W. -R. Yu, S. -H. Hong, *Nanotechnology*, 2010, 21, 245605.

(69) I. -D. Kim, E. -K. Jeon, S. -H. Choi, D.-K. Choi, H. L. Tuller, *J. Electroceram.*, 2010, 25, 159-167.

(70) P. Sun, W. Zhao, Y. Cao, Y. Guan, Y. Sun and G. Lu, *CrystEngComm*, 2011, 13, 3718.

- (71) T. Kuykendall, P. J. Pauzauskie, Y. Zhang, J. Goldberger, D. Sirbuly, J. Deninger and P. Yang, *Nature Materials*, 2004, 3, 524-528.
- (72) X. Wang, Y. Liu, G. Yu, C. Xu, J. Zhang and D. Zhu, *J. Phys. Chem. B*, 2001, 105, 9422-9425.
- (73) D. H. Kim, W. -S. Kim, S. B. Lee and S. -H. Hong, *Sens. Actuators B*, 2010, 147, 653-659.
- (74) M. Batzill and U. Diebold, *Prog. Surf. Sci.*, 2005, 79, 47–154.
- (75) S. Budak, G. X. Miao, M. Ozdemir, K. B. Chetry and A. Gupta, *J. Cryst. Growth*, 2006, 291, 405–411.
- (76) L. Mazeina , Y. N. Picard, J. D. Caldwell, E. R. Glaser, S. M. Prokes, *J. Cryst. Growth*, 2009, 311, 3158-3162.
- (77) P. Nguyen, H. T. Ng, J. Kong, A. M. Cassell, R. Quinn, J. Li, J. Han, M. McNeil and M. Meyyappan, *Nano Lett.*, 2003, 3 (7), 925-928.
- (78) S. Mathur and S. Barth, *Small*, 2007, 3, 2070-2075.
- (79) A. Leonardy, W. -Z. Hung, D. -S. Tsai, C. -C. Chou and Y. -S. Huang, *Cryst. Growth Des.*, 2009, 9 (9), 3958-3963.
- (80) J. Pan, H. Shen, U. Werner, J. D. Prades, F. Hernandez-Ramirez, F. Soldera, F.

- Mücklich and S. Mathur, *J. Phys. Chem. C*, 2011, 115, 15191–15197.
- (81) W. -S. Kim, D. Kim, K -J. Choi, J. -G. Park and S. -H. Hong, *Cryst. Growth Des.*, 2010, 10 (11), 4726-4751.
- (82) J. -H. Kwon, Y. -H. Choi, D. Kim, M. Yang, J. Jang, T. W. Kim, S. -H. Hong and M. Kim, *Thin Solid Films*, 2008, 517, 550-553.
- (83) G. S. Doerk, N. Ferralis, C. Carraro and R. Maboudian, *J. Mater. Chem.*, 2008, 18, 5376-5381.
- (84) C. Yan, M. Y. Chann, T. Zhang and P. S. Lee, *J. Phys. Chem. C*, 2009, 113, 1705-1708.
- (85) K. A. Dick, S. Kodambaka, M. C. Reuter, K. Deppert, L. Samuelson, W. Seifert, L. R. Wallenberg and F. M. Ross, *Nano Lett.*, 2007, 7 (6), 1817-1822.
- (86) F. Gu, L. Gai, W. Shao, C. Li and L. Schmidt-Mende, *Chem. Commun.*, 2011, 47, 8400–8402.
- (87) R. F. Zhuo, H. T. Feng, J. T. Chen, D. Yan, J. J. Feng, H. J. Li, B. S. Geng, S. Cheng, X. Y. Xu and P. X. Yan, *J. Phys. Chem. C* 2008, 112, 11767–11775.
- (88) Q. Wan, J. Huang, Z. Xie, T. Wang, E. N. Dattoli and W. Lu, *Appl. Phys. Lett.*, 2008, 92, 102101.

- (89) Jung, D. -K. Ko and R. Agarwal, *Nano Lett.*, 2007, 7 (2), 264-268.
- (90) S. Sun, G. Meng, G. Zhang, J. -P. Masse and L. Zhang, *Chem. Eur. J.*, 2007, 13, 9087-9092.
- (91) W. -J. Lee, J. Ma, J. Bae, M. -Ho. Cho and J. P. Ahn, *CrystEngComm*, 2011, 13, 690-696.
- (92) J. X. Wang, D. F. Liu, X. Q. Yan, H. J. Yuan, L. J. Ci, Z. P. Zhou, Y. Gao, L. Song, L. F. Liu, W. Y. Zhou, G. Wang and S. S. Xie, *Solid State Commun.*, 2004, 130, 89-94.
- (93) Y. X. Chen, L. J. Campbell and W. L. Zhou, *J. Cryst. Growth* 2004, 270, 505.
- (94) Y. Ding, P. X. Gao and Z. L. Wang, *J. AM. CHEM. SOC.*, 2004, 126, 2066-2072.
- (95) Z. Liu, D. Elbert, C. -L. Chien and P. C. Searson, *Nano Lett.*, 2008, 8 (8), 2166–2170.
- (96) V. Schmidt, S. Senz and U. Gösele, *Appl. Phys. A: Mater. Sci. Process.*, 2005, 80, 445– 450.
- (97) J. E. Allen, E. R. Hemesath, D. E. Perea, J. L. Lensch-Falk<sup>1</sup>, Z. Y. Li, F. Yin, M. H. Gass, P. Wang, A. L. Bleloch, R. E. Palmer, L. J. Lauhon, *Nature Nanotechnology*, 2008, 3, 168-173.

- (98) D. Tsivion, M. Schwartzman, R. Popovitz-Biro, P. v. Huth, E. Joselevich, *Science*, 2011 (333), 1003.
- (99) C. L. Hsin, J. H. He, C. Y. Lee, W. W. Wu, P. H. Yeh, L. J. Chen, Z. L. Wang, *Nano Lett.*, 2007 (7), 1799-1803.
- (100) S. A. Fortuna, J. Wen, I. S. Chun, X. Li, *Nano Lett.*, 2008 ( 8), 4421-4427.
- (101) Y. Yoo, K. Seo, S. Han, K. S. K. Varadwaj, H. Y. Kim, J. H. Ryu, H. M. Lee, J. P.g Ahn, H. Ihee, B. Kim, *Nano Lett.*, 2010, 10 (2), 432-438.

## **Chapter 4.**

# **Magnesiothermic Reduced Silicon Nano-structure for Li-ion Battery Application**

## **4.1. Synthesis of reduced graphene oxide wrapped silicon nanosheet from natural sand and their electrochemical properties**

### **4.1.1. Introduction**

Currently, graphite is used as anode electrode for Li-ion battery for industry due to excellent capacity retention during the cycling. Nevertheless, graphite electrode has a low specific capacity ( $372 \text{ mAh g}^{-1}$ ) and shows a poor rate capability.[1-3] Li-ion battery have predominantly provided the electrical power necessary to operate small portable electronic devices such as cellular phones, laptop computers, and camcorders in the past decade. Recently, it has been applied to both HEVs (hybrid electric vehicles) and back-up electricity storage units for renewable energy sources. Since the demand for safe Li-ion batteries exhibiting high power, large capacity, and high rate capability is ever increasing, new electrode materials is required to replace graphite of low capacity. Most of all, silicon based systems are definitely attractive candidates since silicon has a large theoretical specific capacity at room temperature ( $\text{Li}_{15}\text{Si}_4 : 3600 \text{ mAh g}^{-1}$ ) and low operating voltage (around  $0.1 \text{ V vs. Li/Li}^+$ ).[4,5] However, silicon based electrodes undergo a large volume change during the cycling and it leads to a poor rate capability.[6,7] To mitigate these problems, various nanostructures were employed to anode material for Li-ion battery. But, synthesis of

nanostructured silicon is required complicated route with toxic precursor or high cost technique, such as CVD (chemical vapor deposition).[8-11] Sandhage group reported that synthesis of porous silicon from SiO<sub>2</sub>, which is a magnesiothermic reduction. They demonstrate that three-dimensional silica was formed into microporous silicon replicas in a sealed steel ampoule at 650 °C by the following reaction:  $2\text{Mg} + \text{SiO}_2 (\text{s}) \rightarrow 2\text{MgO} (\text{s}) + \text{Si} (\text{s})$ . [12,13] Recently, the magnesiothermic reduction process has been attracted and various silicon nanostructures, such as nanotube, hollow sphere, porous structure, etc., were formed via this technique.[14-16] These studies show good electrochemical properties but most research is required a several step to synthesize a nanostructured SiO<sub>2</sub>.

Herein, a silicon nanosheet is successfully prepared by magnesiothermic reduction with natural sand. As well-known, two-dimensional silicon nanostructures, such as nanosheet and nanoplate, are a promising structure. But, two-dimensional silicon nanostructure is required complicate process with CVD technique, as well.[17,18] Even though, silicon nanosheet is recently prepared by using graphene oxide as template and magnesiothermic reduction.[19] This process is also required a purified SiO<sub>2</sub> source, TEOS. In this study, the sand was used as precursor and template for synthesis of silicon nanosheet. This might be the lowest cost process for synthesis technique of silicon nanostructure.

#### **4.1.2. Experimental procedure**

**1) Synthesis of Silicon Nanosheet:** 1 g of commercial sand (ficher) was crushed by planetary ball milling for 4h. The crushed sand was washed with D. I. water, dried and calcined to remove organic impurities at 600 °C for 1h. Then, 0.4 g of calcined sand and 0.32 g of magnesium (325 mesh, Stream) were mixed by grinding. The mixture was heated in a tube furnace at 700 °C for 4h at 5 vol. % H<sub>2</sub>/N<sub>2</sub> atmospheres. The brown products were washed with hydrochloric acid solution and hydrofluoric acid solution. (10 wt. %)

**2) Synthesis of graphene oxide:** Graphite oxide (GO) was prepared through Hummers' method,[20] by reacting commercially obtained graphite powder in a mixture of H<sub>2</sub>SO<sub>4</sub>, NaNO<sub>3</sub>, and KMnO<sub>4</sub>. After completion of the reaction, H<sub>2</sub>O<sub>2</sub> was added to the reaction vessel. The GO was filtered and washed twice with 1 M HCl and twice with DI water. The GO separated in the form of a dry, brown powder.

**3) Graphene wrapping:** 0.1 g of prepared silicon nanosheet was dispersed in 100 mL absolute ethanol and 2 mL of APTES was added.[21] After stirring for 4h, the above solution was wash and centrifuged with absolute ethanol. And, 0.15 g

G.O was dispersed in 80 mL water by tip-signification and 20 mL silicon nanosheet water solution was added in prepared G.O solution. The stirring of mixture solution is conducted for 4h. The solution was washed and centrifuged by D.I.water and the Si-G.O. composite was filtered and dried. Finally, the obtained powder was reduced at 400 °C for 6h under 5 % H<sub>2</sub>/N<sub>2</sub>.

**4) Electrochemcial Test:** The test electrodes consisted of the active powder material (70 wt.%), carbon black (Ketjen Black, 10 wt.%) as a conducting agent and poly amide imide (PAI, 20 wt.%) dissolved in N-methyl pyrrolidinone (NMP) at 60 °C as a binder. Each component was well mixed to form a slurry using a magnetic stirrer. That slurry was coated on a copper foil substrate, pressed, and dried at 200 °C or 4 h under a vacuum. A coin-type electrochemical cell was used with lithium foil as the counter and reference electrode and 1 M LiPF<sub>6</sub> and 10% fluoroethylene carbonate (FEC) in ethylene carbonate (EC)/diethyl carbonate (DEC) (3:7 (v/v), PANAX) as the electrolyte. The cell assembly and all of the electrochemical tests were carried out in an Ar-filled glove box. The cell experiments were galvanostatically performed using a Maccor automater tester at a constant current of 200 mA g<sup>-1</sup> (200 mA g<sup>-1</sup>, 500 mA g<sup>-1</sup>, 1000 mA g<sup>-1</sup>, 2000 mA g<sup>-1</sup>, 3000 mA g<sup>-1</sup>, 200 mA g<sup>-1</sup> at each step in the rate capability test) for the active material within the voltage range between 0.0

V and 2.0 V (vs. Li/Li<sup>+</sup>).

### 4.1.3. Results and discussion

#### *Phase and morphology of synthesized silicon nanosheet*

X-ray diffraction (XRD) analysis shows that the crushed sands were converted to Si nanosheet by magnesiothermic reduction. The XRD patterns of ball-milled sand, as reduced specimen, after HCl and HF treatment are shown in Figure 4.1.1. The XRD pattern of the ball-milled is indexed to quartz-SiO<sub>2</sub>. After reduction, silicon (JCPDS No. 27-1402), magnesium oxide (MgO, JCPDS No. 45-0946), magnesium silicide (Mg<sub>2</sub>Si, JCPDS), and remained quartz-SiO<sub>2</sub> is observed. When mixing the ball-milled sand and magnesium, the molar ratio of the sand and magnesium is 1: 0.8 according to SiO<sub>2</sub>+2Mg=Si+2MgO. But it is impossible to form a perfect mixture with micro-sized the sand and magnesium powder, so unreacted sand and Mg<sub>2</sub>Si, resulted from excess Mg, is observed. Indeed, the solid phase of magnesium is transformed to liquid or gas phase at 700 °C processing temperature while the ball-milled sand is micro-scaled solid. Therefore, most of the ball-milled sand powders are exposure to the Mg excess condition. The peaks of MgO are disappeared after HCl treatment, silicon and quartz, unreacted sand, phases are observed after HCl treatment. After HF treatment, only silicon peaks are observed.

The SEM image of commercial sand is shown in Figure 4.1.2(a). The commercial sand is a few hundreds micrometer size and it reduced to hundreds nanometer ~ micrometer during planetary ball-milling (4.2(b)). Especially, a few micrometers sized sand show flat surface and it is the critical role as template for growth of silicon nanosheet. As seen in Figure 4.1.2, the silicon nanosheet is formed on the surface of sand, so flat and large surface is favorable for synthesis of wide silicon nanosheet. After HF treatment, two-dimensional silicon nanosheet is obtained (4.1.2(c) and (d)). The nanosheet has a fallen leaves liked shape and the diameter is a few hundreds nanometer. The torn region of silicon nanosheet might be resulted by HF treatment. The exact thickness of silicon nanosheet is not measured from SEM image, but the nanosheet is flexible and very thin, compared to the area of nanosheet.

Transmission electron microscopy (TEM) images of the synthesized silicon nanosheet are shown in Figure 4.1.3. The low-magnification TEM image shows the widely dispersed silicon nanosheet and the selected area electron diffraction (SAED) indicated the synthesized silicon nanosheets are well-crystallized as single phase without other impurities, as well. At higher magnification, the 2-dimesional structure is revealed with over 50 nm width. Even though polycrystalline liked morphologies are shown, the silicon nanosheet is,

indeed, composed of single crystal. The high resolution TEM image of Figure 4.1.3(d) clearly shows the silicon nanosheet is the single crystal. In the general concept of magnesiothermic reduction, the reduced silicon has polycrystalline nature with a few nano-sized grains but our synthesized silicon nanosheet is the single crystalline and the size (or width) is from 20 nm to a few hundreds nanometers. This single crystalline structure indicates that the represented silicon nanosheets are formed by different mechanism from general magnesiothermic reduction.

Figure 4.1.4 shows nitrogen adsorption–desorption isotherms and surface area of silicon nanoparticle and synthesized nanosheet. The BET surface area and pore parameters of the samples determined from the nitrogen adsorption–desorption isotherm by the BJH (Barrett–Joyner–Halenda) method are summarized in Table 4.1.1.

### ***Synthesis sequence of silicon nanosheet***

To understand a formation of the silicon nanosheet, the HCl treated sand, reduced by magnesiothermic reduction, was investigated by TEM analysis. It is revealed the most of particles have the yolk/shell liked structure or hollow structure (Figure 4.1.5). The large size spherical particle is not observed in SEM image

(Figure 4.1.2) because  $\text{SiO}_2$  is dissolved by HF treatment, so core material might be  $\text{SiO}_2$ . From this observation, it is concluded that the Mg did not reach to the core and the large amount of  $\text{SiO}_2$  remained in our condition, only surface of sand was reacted and reduced. The hollow space might be results of dissolution of  $\text{Mg}_2\text{Si}$  in HCl because  $\text{Mg}_2\text{Si}$  is easily dissolved in HCl solution. As seen in Figure 4.1.5(d), the silicon nanosheet is formed with follow step: the core-shell structure of  $\text{SiO}_2/\text{Mg}_2\text{Si}/\text{silicon}$  is, at first, formed during magnesiothermic reduction. Then, the  $\text{Mg}_2\text{Si}$  and  $\text{SiO}_2$  are dissolved during HCl and HF treatment, sequentially, and the shell-layer of silicon is partially etched by HF solution, as well. Finally, the silicon nanosheet is obtained. A HR-TEM image of shell-layer reveals the thickness of silicon nanosheet (Figure 4.1.5(c)). The thickness of shell layer is about 20 nm and it is composed of multi layered structure. The thickness of silicon nanosheet is supposed to about 20 nm through these results even though the thickness of silicon nanosheet was directly not measured.

### ***Graphene wrapped silicon nanosheet***

For improvement of electrochemical properties, the silicon nanosheets were encapsulated to overcome their low electrical conductivity and to support the large volume expansion by graphene. The graphene was simple prepared by well-known hummer method and the encapsulation was conducted by aminopropyltrim-ethoxysilane (ATPES) modification.[20,21] The TEM images of

graphene encapsulated silicon nanosheet is shown in Figure 4.1.6. The graphene is not well observed in low-magnification TEM and SAED is exactly the same to the bare silicon nanosheet. The HRTEM image clearly reveals that silicon nanosheet is well-encapsulated by graphene.

### ***Electrochemical properties***

The electrochemical properties of silicon nanosheet and graphene encapsulated silicon (Si@ Graphene) nanosheet electrodes were shown in Figure 4.1.7. The electrochemical test was carried out in the voltage of 0-2 V with a current density of 200 mA g<sup>-1</sup>. The voltage profiles of silicon nanosheet and Si@ Graphene are shown in Figure 4.1.7(a). The first cycle discharge and charge capacity of silicon nanosheet were 3563 and 2431 mAh g<sup>-1</sup> and those of Si@Graphene were 3769 and 2625 mAh g<sup>-1</sup>. The charge capacity of Si@ Graphene is similar to that of silicon nanosheet and specific difference of voltage profile was not observed at the first cycle. This indicates the silicon is fully lithiated to Li<sub>15</sub>Si<sub>4</sub>. Figure 4.1.7(b) clearly shows the higher cyclability of graphene encapsulated silicon nanosheet. The silicon nanosheet exhibits higher reversible capacity than commercial nano-silicon even though it was synthesized from sand. The graphene wrapping effectively improved the cyclability of silicon nanosheet and the rate capability of graphene wrapped silicon nanosheet is very impressive. The reversible capacity of graphene wrapped silicon nanosheet is not

decreased with increasing a discharge current density and it show 1113 mAh g<sup>-1</sup> at a high discharge current density at 3 A g<sup>-2</sup>.

#### **4.1.4. Conclusions**

In summary, we simply synthesized the silicon nanosheet by the magnesiothermic reduction with natural sand as source and template. The synthesized silicon nanosheet was well crystallized and showed better electrochemical properties than commercial silicon nanopowder for anode of lithium rechargeable battery and further enhancement was achieved by graphene encapsulation. Indeed, there are still a few questions about the synthesis mechanism even though we proposed the formation mechanism of silicon nanosheet.

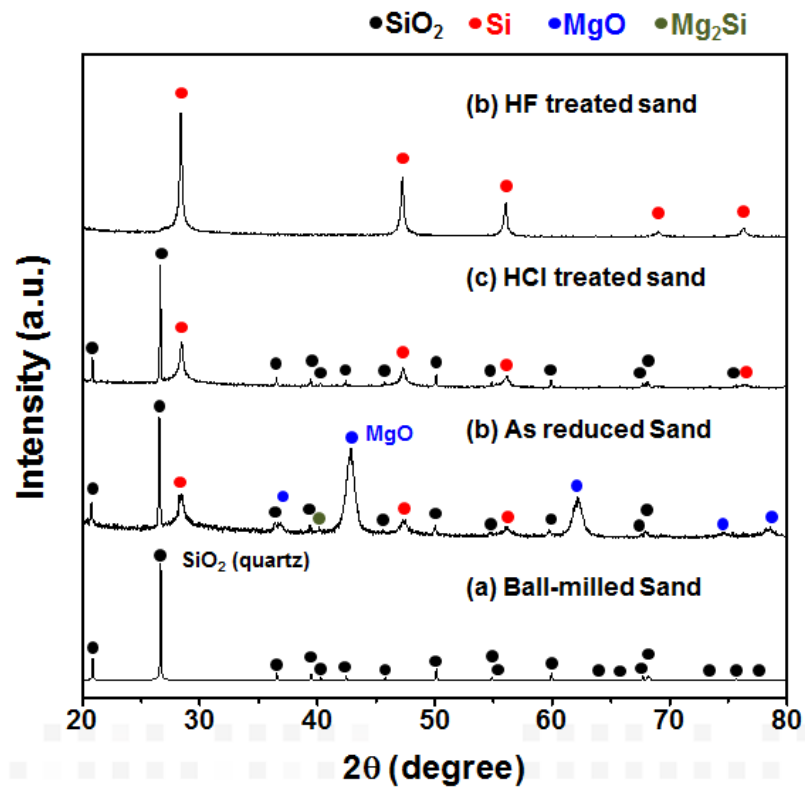


**Figure 4.1.1.** XRD patterns of (a) ball-milled sand, (b) as reduced silicon, (c) HCl and (d) HF acid treated silicon nanosheet.

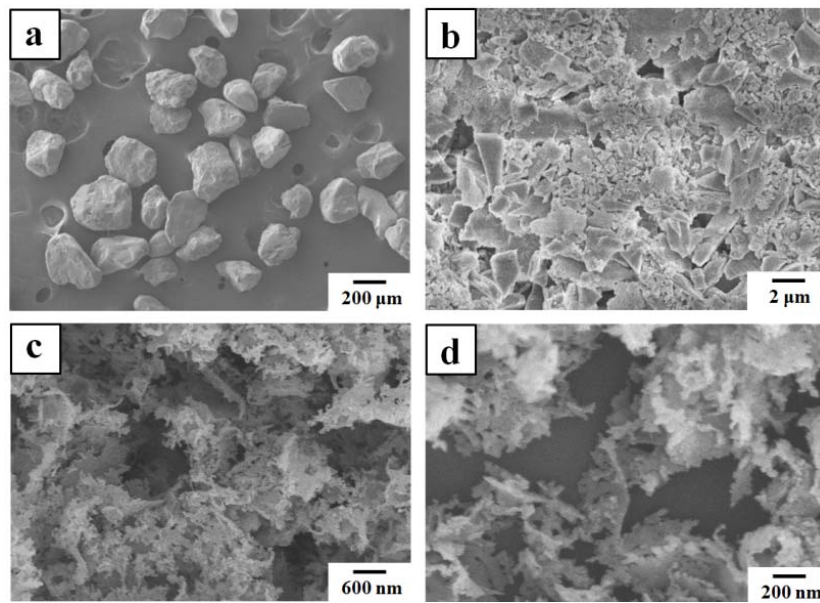


**Figure 4.1.2.** SEM image of (a) commercial sand, (b) ball-milled sand, (c) and (d) synthesized silicon nanosheet.

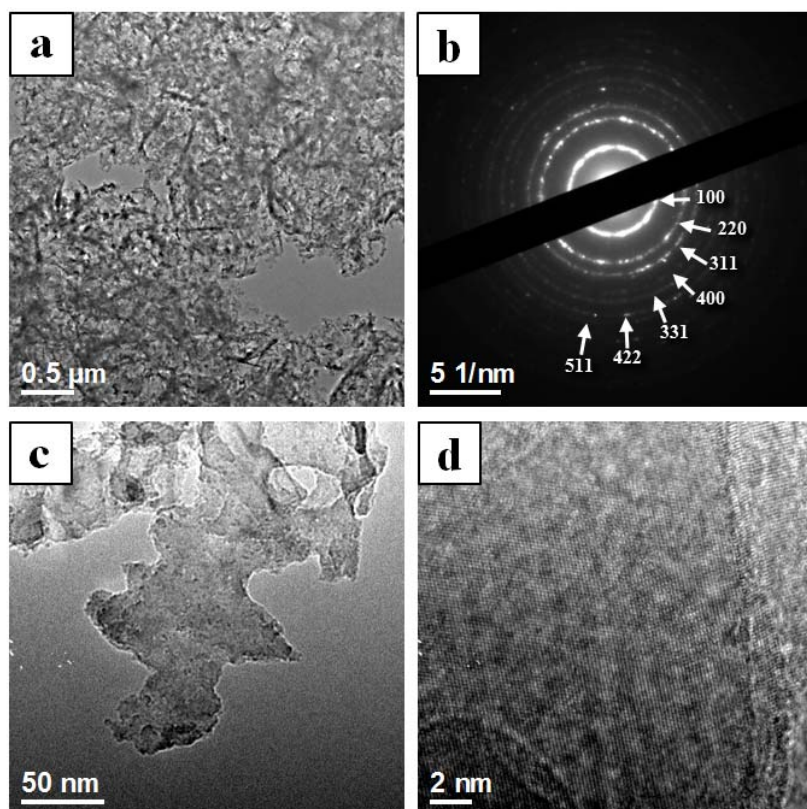


**Figure 4.1.3.** (a) low magnification TEM image of silicon nanosheet, (b) SAEP of silicon nanosheet, (c) and (d) HRTEM image of silicon nanosheet.

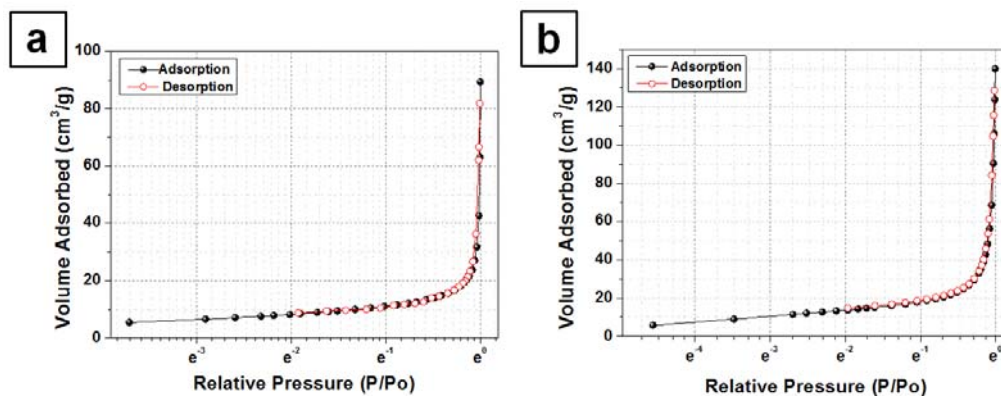


**Figure 4.1.4.** Nitrogen adsorption–desorption isotherms of (a) commercial silicon nanoparticle, (b) synthesized silicon nanosheet.

**Table 4.1.1.** (a)-(c) HCl treated products, (d) Schematic illustration of the synthesis of silicon nanosheet.

		Commercial nano-silicon	Silicon nanosheet
<b>BET Surface Area (m<sup>2</sup>/g)</b>		33.7426	55.7588
<b>Pore (m<sup>2</sup>/g)</b>	<b>BJH Adsorption Surface Area of pores</b>	27.4843	50.8200
	<b>BJH Desorption Surface Area of pores</b>	25.3879	49.0293

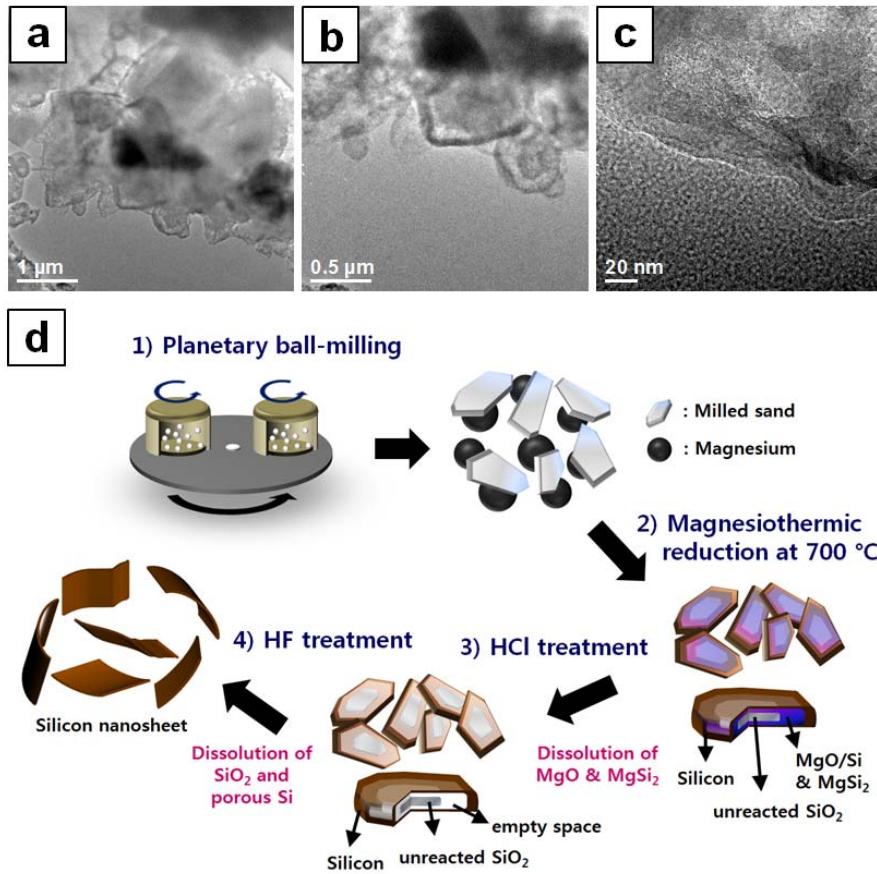


**Figure 4.1.5.** (a)-(c) HCl treated products, (d) Schematic illustration of the synthesis of silicon nanosheet.

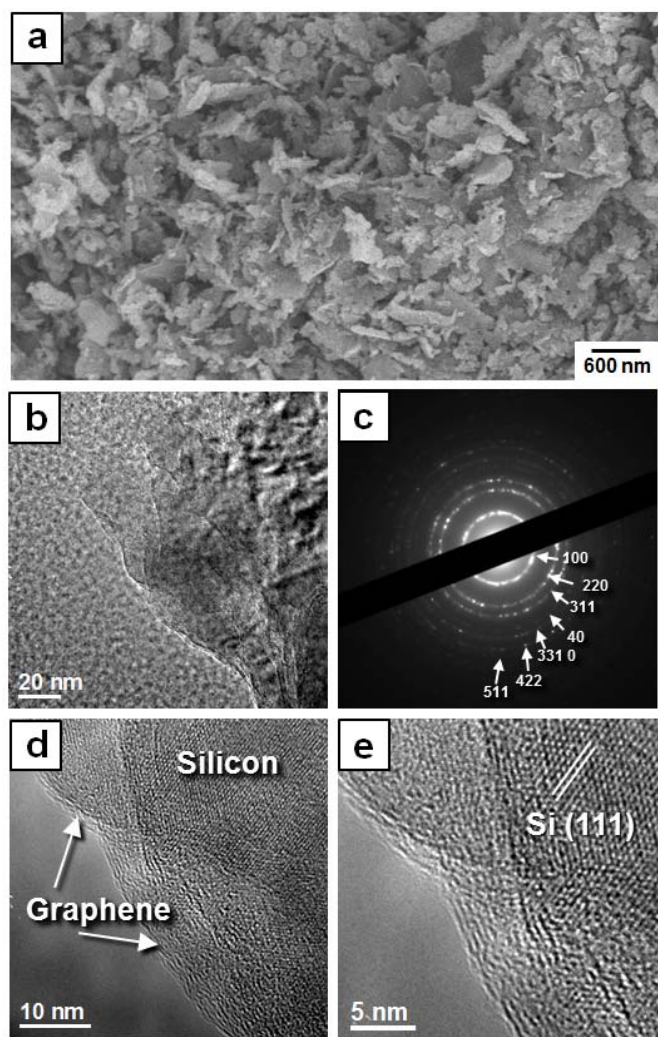


**Figure 4.1.6.** TEM and SAEP image of graphene wrapped silicon nanosheet.

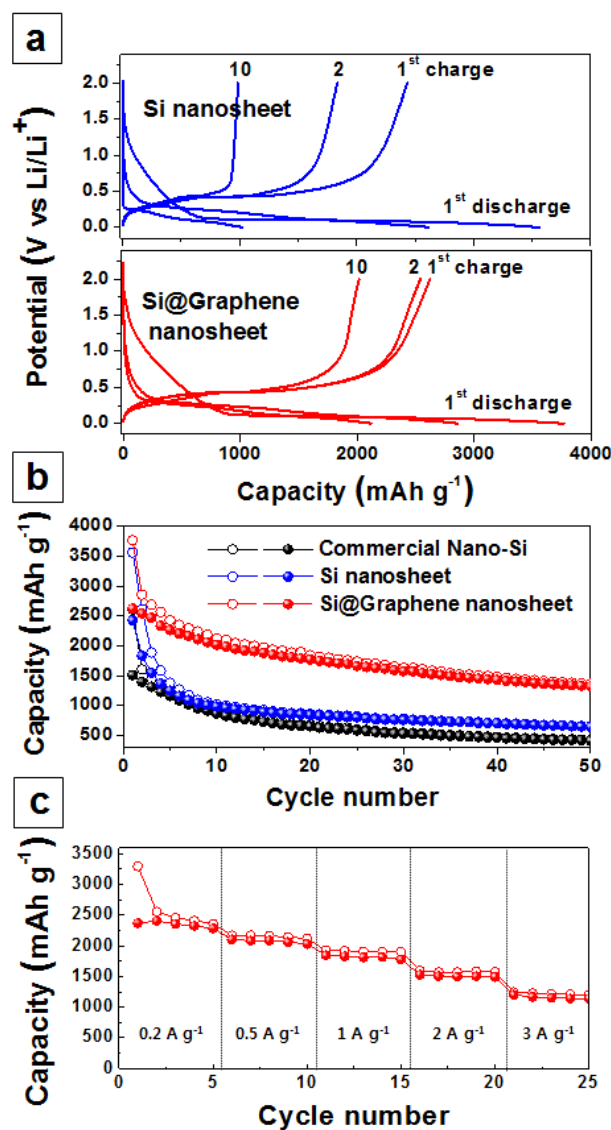


**Figure 4.1.7.** (a) Voltage profiles of silicon nanosheet and graphene encapsulated silicon nanosheet electrodes after 1, 2, 10, 30, 50 cycles at 200 mA g<sup>-1</sup> between 0 and 2.0 V. (b) Cyclability of commercial nano-silicon power, silicon nanosheet and graphene wrapped silicon nanosheet, (c) rate capability of graphene wrapped silicon nanosheet.

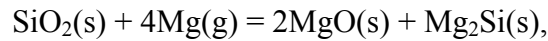
## 4.2. Understanding of magnesiothermic reduction

### 4.2.1. Introduction

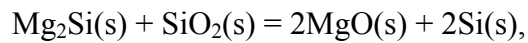
In previous chapter, synthesis of silicon nanosheet is demonstrated, but the exact formation mechanism is not still established. A multi-layered structure of  $\text{SiO}_2@\text{Mg}_2\text{Si}@\text{Si}$  is formed during synthesis of silicon nanosheet. However the formation of this multi-layered structure could not be explained by according to general reaction of magnesiothermic reaction,  $\text{SiO}_2 + 2\text{Mg} = 2\text{MgO} + \text{Si}$ . So the detailed reduction mechanism of magnesiothermic reduction is investigated in the chapter.

Barati et al recently suggested the  $\text{Mg}_2\text{Si}$  might be involved during reduction reaction at the early stage of reduction process and the  $\text{SiO}_2$  is reduced by  $\text{Mg}_2\text{Si}$ . [22] Figure 4.2.1 show that comparison of Si yield and  $\text{Mg}_2\text{Si}$  yield with processing temperature and  $\text{Mg}/\text{SiO}_2$  mol ratio. When decreasing of  $\text{Mg}_2\text{Si}$ , the Si yield is increasing. From these results, they suggested that  $\text{Mg}_2\text{Si}$  is consumed for the  $\text{SiO}_2$  reduction. Due to the accelerated kinetics of the reactions at higher temperatures, reduction by  $\text{Mg}_2\text{Si}$  ( $\text{Mg}_2\text{Si} + \text{SiO}_2 = 2\text{Si} + 2\text{MgO}$ ) that requires solid state reaction or diffusion can take place to a greater extent, giving rise to more reduction of  $\text{SiO}_2$  at the expense of  $\text{Mg}_2\text{Si}$ .

This is the one of evidence for understanding the reaction mechanism of magnesiothermic reduction. The reaction of  $\text{SiO}_2 + 2\text{Mg} = 2\text{MgO} + \text{Si}$  could be divided into followed two reactions as mentioned in chapter 1.3:



$$\Delta G^\circ(650^\circ\text{C}) = -332.3 \text{ kJ/mol} \quad (1.3.2)$$



$$\Delta G^\circ(650^\circ\text{C}) = -189.6 \text{ kJ/mol} \quad (1.3.3)$$

The reaction of (1.3.2) and (1.3.3) is thermodynamically stable but it has not been observed in experimental results.

In this chapter, two topics will be discussed; 1) the initial stage of reduction mechanism, and 2) the formation of inverse opal liked porous silicon nanostructure. The initial stage of reduction mechanism is investigated by using 100 nm sized  $\text{SiO}_2$  nanoparticles and the reduction was conducted at various temperatures, from 475 to 700 °C. And inverse opal liked silicon structure is induced from 50nm sized  $\text{SiO}_2$ , the  $\text{SiO}_2$  nanoparticle was mixed with magnesium powder and formed a pellet.

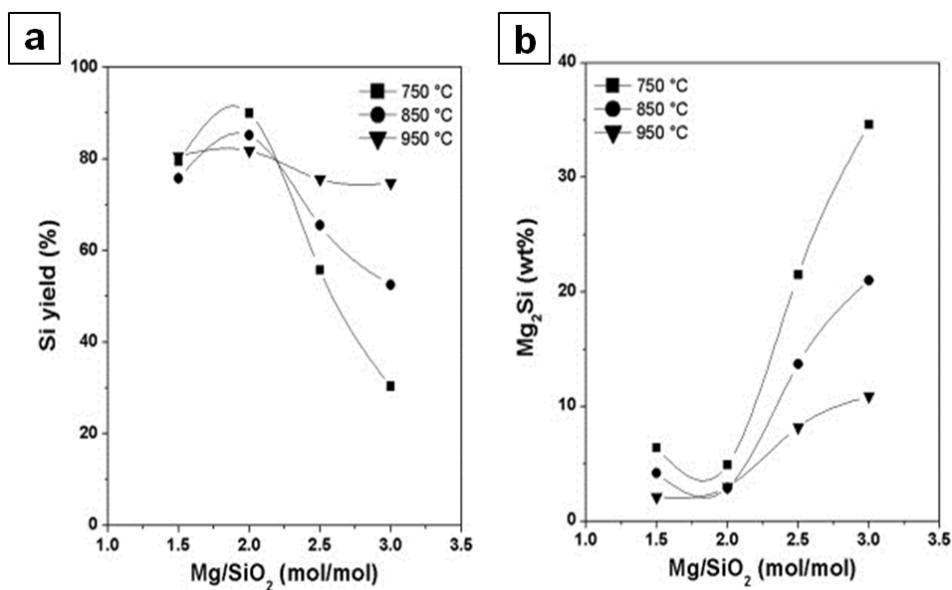


**Figure 4.2.1.** (a) Effect of magnesium/silica ratio and temperature on (a) Si yield and (b) Mg<sub>2</sub>Si amount.[22]

#### 4.2.2. Experimental procedure

##### *Synthesis of silicon nanoparticle and inverse-opal liked silicon nanostructure:*

Nano-sized SiO<sub>2</sub> powder and magnesium powder were used as precursor. The SiO<sub>2</sub> nanopowder was synthesized by Stöbber method (details in the experimental section, chapter 2. The synthesized SiO<sub>2</sub> nanopowder was annealed at 600 C for 1h. After that, the SiO<sub>2</sub> and well-grinded magnesium powder were mixed with 2:1 weigh ratio (0.2 g of SiO<sub>2</sub> and 0.16 g Mg). For the synthesis of silicon nanoparticle, the mixture powder was heated in a tube furnace at a certain

processing temperature (from 425 to 700 °C). And the mixture powder was uniaxially pressed into pellets (green body) of 10 mm in diameter at 40 kg/cm<sup>2</sup> pressure for synthesis of inverse opal liked silicon nanostructure. The green body was located at the center of tube furnace and the reduction process was conducted at 700 °C for 30 min. All of reduction process was conducted under Ar atmosphere. The products were collected and washed with hydrochloric acid solution and hydrofluoric acid solution (10 wt. %).

### **4.2.3. Results and discussion**

#### ***Reduction mechanism of silicon nanoparticle***

To reveal the initial stage of reduction process, the process was conducted at different temperature. The mixture powder of Mg and 100 nm sized SiO<sub>2</sub>, with weight of 0.8:1, is used as starting material. As seen the figure 1.3.3, reaction of “SiO<sub>2</sub> + 4Mg = 2MgO + Mg<sub>2</sub>Si” is thermodynamically more favorable than “SiO<sub>2</sub> + 2Mg = 2MgO + Si”. However, the initial stage of reduction process has not been investigated in the previous studies. Usually, the reduction process was conducted at around 650 ~ 750 °C, but these temperatures are not suitable for investigation of initial stage due to the accelerated kinetics of the reaction at higher temperature. Figure 4.2.2 shows the XRD pattern of reduced SiO<sub>2</sub> various temperature, from

425 to 700 °C. Mg<sub>2</sub>Si and MgO phase is observed from 475 °C and Mg is still remained, but any silicon phase was not observed. The Mg<sub>2</sub>Si peaks are increased to 500 °C and it is slightly decreased from 550 °C and it might reveal the formation of Mg<sub>2</sub>Si is almost finished. In contrast, silicon phase is observed from at 600 °C and the highest intensity is shown at 650 and 700 °C. But further increasing of silicon peaks is not observed. The appeared phases at different temperature are shown in the Table 4.2.1. The XRD results indicate that the Mg<sub>2</sub>Si is formed at the initial stage of reduction and Si is generated by consuming the Mg<sub>2</sub>Si.

Indeed, kinetic factors, such as diffusion length into SiO<sub>2</sub> and evaporation rate, of Mg are strongly dependent on the reducing temperature and it might affect to the reducing process of SiO<sub>2</sub>. Mg diffusion into SiO<sub>2</sub> could control the formation of Mg<sub>2</sub>Si and MgO for all of case solid state, liquid-solid, gas-solid reaction, and it directly related to internal structure of reduced silicon nanostructure. And evaporation rate of Mg is increased by increasing the reducing temperature. In the diffusion point of view, higher temperature is favorable to form the well-distributed Mg<sub>2</sub>Si and to uniformly reduce SiO<sub>2</sub> nanostructure. However, higher temperature also induces to accelerate the evaporation of Mg, thus uniform reduction is restricted by loss of reducing agent. In other words,

increasing reducing temperature for increasing diffusion of Mg has to be limited by the term of Mg evaporation.

The phase evolution during reduction process with increasing processing temperature is confirmed in previous section. In this section, the phase evolution with reaction time as constant temperature will be discussed. Figure 4.2.3 shows the XRD results of reduced SiO<sub>2</sub> powder with different reaction time at 500, 600, and 700 °C. As seen the Figure 4.2.3, strong Mg<sub>2</sub>Si peaks are observed when reducing temperature is at 500 °C and the Mg<sub>2</sub>Si is getting disappeared with increasing temperature. From these results, two possibilities of silicon formation are deduced. The first, silicon is generated from the reaction of “Mg<sub>2</sub>Si + SiO<sub>2</sub> (unreacted) = 2MgO + 2Si”. And precipitation of silicon from Mg<sub>2</sub>Si is also possible, because Mg<sub>2</sub>Si have to decompose into Mg and Si to react with SiO<sub>2</sub>. The former reaction is acceptable because the Gibbs free energy of this reaction is negative, as seen the Figure 1.3.3. But the latter reaction is still controvertible because it is difficult to observe the precipitation of silicon from Mg<sub>2</sub>Si. When increasing the reaction temperature, the reduction time is decreased. Whole reduction process is completed in 1h above reduction temperature of 600 °C ,

To investigate how the mg<sub>2</sub>Si forms inside of SiO<sub>2</sub> and the silicon is generated from between Mg<sub>2</sub>Si and SiO<sub>2</sub>, the TEM analysis is conducted.

Unfortunately, as reacted (or reduced) SiO<sub>2</sub> is covered by Mg<sub>2</sub>Si or MgO, so it is impossible to observe. HCl treated reduced SiO<sub>2</sub> is shown in Figure 4.2.4. Figure 4.2.4(a)-(c) is the TEM image of sample, reduced at 500 °C without holding time. As seen the 4.2.3, this sample is composed of Mg<sub>2</sub>Si, MgO, and unreacted SiO<sub>2</sub>, so pore region of this figure is expected as Mg<sub>2</sub>Si and MgO region. After 8h reaction, silicon is generated and the TEM image of this sample is shown in Figure 4.2.4(d)-(g). The SAED pattern is indexed as silicon phase and the reduced silicon sphere is comprised of interconnected silicon nanoparticle.

In summary, the sequence of magnesiothermic reduction is schematically shown in Figure 4.2.5. The reaction “SiO<sub>2</sub>(s) + 4Mg(g) = 2MgO(s) + Mg<sub>2</sub>Si(s)” is occurred at from around 450 to 500 °C, and this reaction is completed in short time. At this stage, the Mg<sub>2</sub>Si is uniformly formed inside of SiO<sub>2</sub>. After that, Si is generated by followed reaction; “Mg<sub>2</sub>Si(s) + SiO<sub>2</sub>(s) = 2MgO(s) + 2Si(s)”. This reaction might be required more time, and it is possible to react under 650 °C (melting point of magnesium).

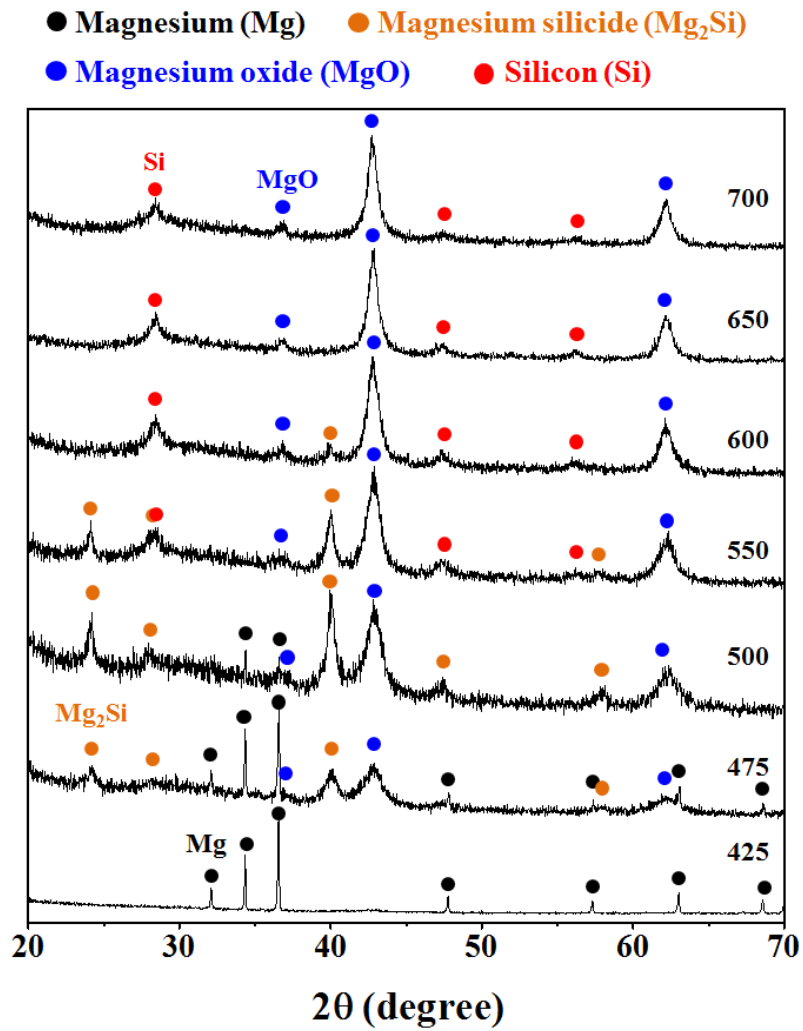
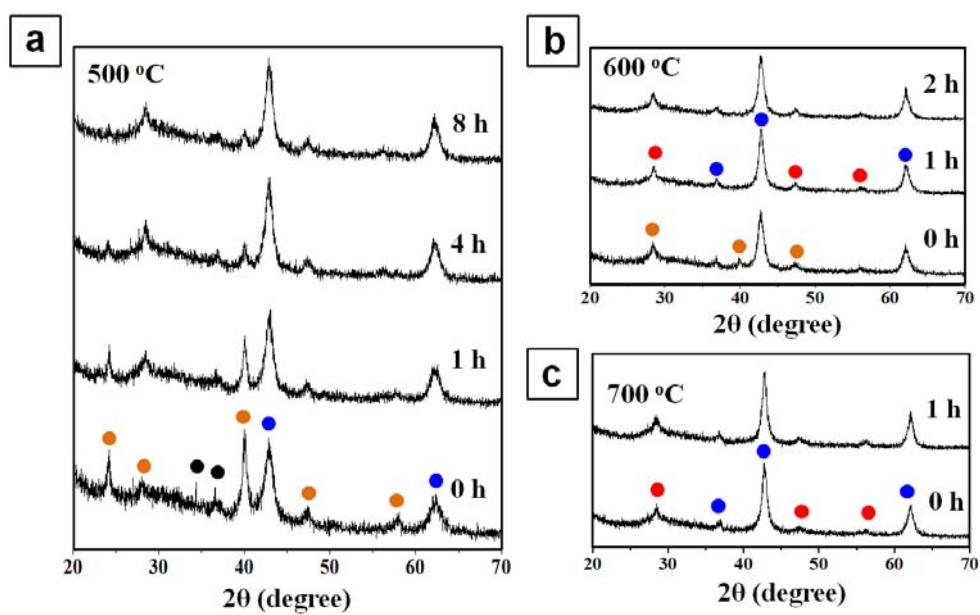


Figure 4.2.2. XRD pattern of reduced SiO<sub>2</sub> with different processing temperature.

**Table 4.2.1.** The phase evolution of magnesiothermic reduction with different temperature.

<b>Temp.</b> (°C)	<b>475</b>	<b>500</b>	<b>550</b>	<b>600</b>	<b>650</b>	<b>700</b>
<b>Phase</b>	Mg, Mg <sub>2</sub> Si, MgO	Mg, Mg <sub>2</sub> Si, MgO	Mg <sub>2</sub> Si, MgO, Si	Mg <sub>2</sub> Si, MgO, Si	MgO, Si	MgO, Si

\* (heating up with 5 °C/min, without holding time)



**Figure 4.2.3.** (a) 500 °C for 0, 1, 4, 8 h, (b) 600 °C for 0, 1, 2h, (c) 700 °C for 0, 1h.

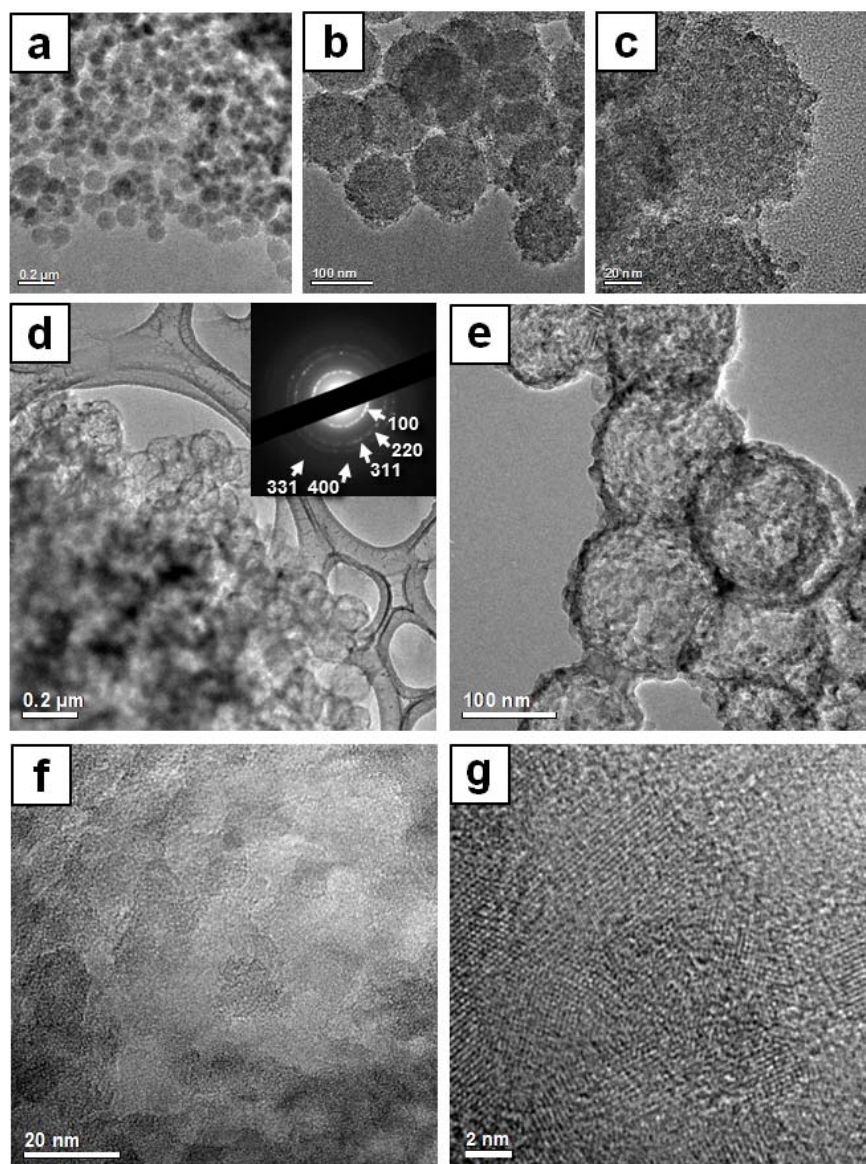


**Figure 4.2.4.** HCl treated reduced SiO<sub>2</sub>, (a)-(c) 500 °C for 1h, (d)-(g) 500 °C for 8h.

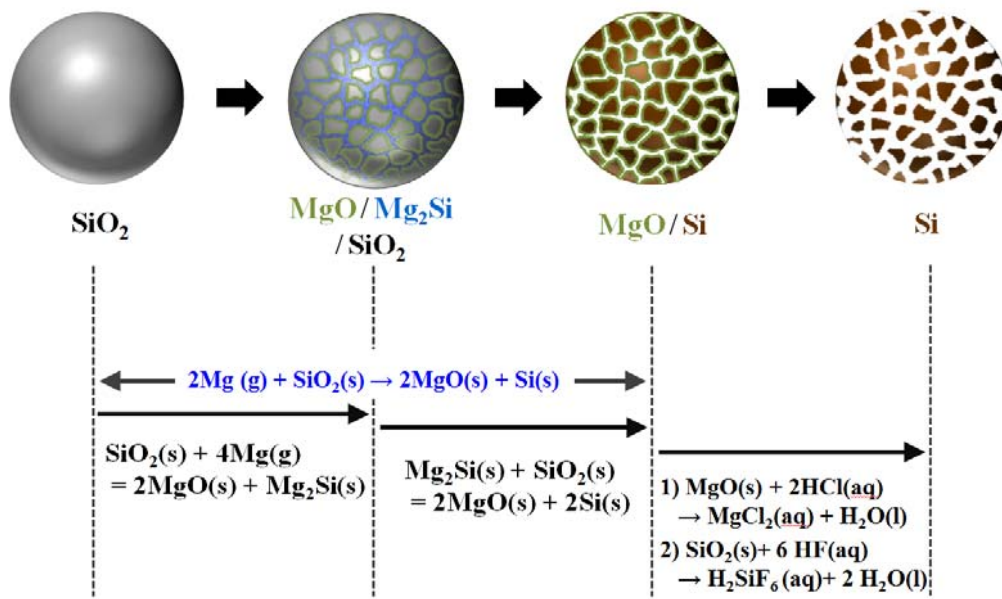


**Figure 4.2.5.** Schematic illustration of magnesiothermic reduction.

### ***Formation mechanism of inverse opal-liked silicon nanostructure***

A very interesting structure of silicon nanostructure was synthesized by using Mg/SiO<sub>2</sub> pellet instead of mixture powder. The SEM image of SiO<sub>2</sub> nanopowder is shown in Figure 4.2.6(a). The SiO<sub>2</sub> nanopowder, served as template and silicon source, is spherical shape and the size is quietly uniform. After reduction and acid (HCl and HF) treatment, the SiO<sub>2</sub> nanoparticle was converted to inverse opal liked silicon nanostructure. The prepared silicon nanostructure is presented in Fig.4.2.6(b)-(d). Even though the particle size is not uniform, all particle show porous (or inverse opal liked) structure. The particle size might be resulted from packing process into mold during formation of pellet, but the further detailed investigation of particle size was not conducted.

The XRD patterns of as reduced and HCl treated sample shown in Figure 4.2.7. The XRD peaks of as reduced sample, at 700 °C for 30 min, are well-matched to Mg<sub>2</sub>Si, MgO, Si and Mg<sub>2</sub>SiO<sub>4</sub> (unmarked peaks, JCPDS 34-0189). Especially, the silicon peaks of inverse opal liked silicon are slightly sharper than that of spherical nanoparticle. It indicates that the inverse opal liked silicon has larger grain size. After HCl and HF treatment, all of by-products are disappeared and only silicon phase is observed.

The TEM images clearly show the internal structure of porous silicon nanostructure (Figure 4.2.8). The porous silicon structure is composed of thin wall around the pore and the SAED patterns are indexed as single phase of silicon. The HRTEM image and FFT pattern show the silicon wall is single-crystalline silicon structure. Figure 4.2.8(f) is the inverse FFT image of figure 4.2.8(e) and this image directly reveal the size of single crystalline silicon is over 20 nm.

To understand the formation mechanism of inverse opal liked silicon, the further XRD analyses were conducted. The XRD patterns of the reduced SiO<sub>2</sub> under different temperature (without holding time) and the observed phase are shown in Fig.4.2.9. Generally, the magnesiothermic reduction is conducted over 650 °C because melting point of magnesium is 650 °C. The diffracted peaks of silicon and MgO were strongly appeared from 450 °C and it indicates the precipitation of silicon is occurred from around 450 °C. The nano SiO<sub>2</sub> powder is amorphous phase so the completion of reduction for all SiO<sub>2</sub> is not known from XRD results. It might be concluded that the reduction or generation of silicon is almost finished because further increasing the peak intensity of Si and MgO is not observed. Mg<sub>2</sub>Si peaks of tiny intensity are detected, and the Mg<sub>2</sub>Si might be crucible factor to formation of nano-porous silicon. As seen the figure 4.2.2 and 4.2.3, the formation of Mg<sub>2</sub>Si is very fast but the reduction, from Mg<sub>2</sub>Si, requires long time or high temperature. So we believe that the formation of inverse opal

liked silicon is different from magnesiothermic reduction.

During reduction process, the pellet burst to powder, but this phenomenon is not occurred in case of powder mixture. The burst powder is blown away from center of tube furnace to around 30 cm away in the quartz tube. This indicated quietly high pressure is applied to inside of pellet. Indeed, it is not still clear how much gas pressure applied to the pellet and how to influence the formation of inverse opal liked silicon structure. Further experiments with different heating schedule were conducted to reveal the effect of gas pressure. To fully release the gas, trapped at contact area of SiO<sub>2</sub> power and pellet, the pellet was calcined at 400 °C for 30 min ~ 8 h. In this case, it was assumed that the reaction between Mg and SiO<sub>2</sub> could be ignored at 400 °C because the calcination temperature is much below the melting point of Mg and any reaction at 400 °C was detected in Figure 4.2.9. The FESEM image of calcined sample clearly (Figure 4.2.10) shows that the silicon nanoparticle was obtained instead of formation inverse opal structure. So it is believed that the trapped gas in the pellet strongly affects the formation of inverse opal liked structure.

Up to now, the precipitation behavior of silicon is not investigated too much. There are a few studies about the precipitation (or growth) of silicon. For example, the precipitation of silicon is studied in the Al-Mg-Si alloys with high

content of silicon. For the alloys without an excess of silicon, the decomposition of the solid solution obtained after quenching from the solutionizing temperature is generally believed to be as follows: supersaturated solid solution (SSS) → cluster (independent cluste of Si and Mg atoms, co-clusters of Si and Mg atoms) → Guinier-preston (GP) zones →  $\beta''$  ( $Mg_5Si$ , coherent precipitates) →  $\beta'$  ( $Mg_{1.8}Si$ , semi-coherent precipitates) →  $\beta$  ( $Mg_2Si$ ) incoherent precipitates.[23] In contrast, precipitation sequence of the alloy with high silicon content is followed: SSS → cluster → GP zones →  $\beta''$  →  $\beta' + Si$  →  $Si + \beta$  ( $Mg_2Si$ ).[23,24] With increasing silicon content, a certain amount of silicon is simultaneously released from  $\beta'$  phase, and precipitation of silicon and  $\beta$  phase is accelerated. Another example is the growth of silicon nanowire by SLS mechanism (soild-liquid-solid). In this case, the amorphous silicon nanowire is synthesized and a Si-Ni liquid droplet is used as catalyst. The deposited Ni film can react with the Si substrate at relatively high temperature, above 930 °C, and forms  $NiSi_2$  eutectic liquid alloy droplets. Because of the relatively high solubility of Si in  $NiSi_2$  eutectic alloy, more Si atoms will diffuse through the solid (the substrate) - liquid inter-face into the liquid-phase (the  $NiSi_2$  droplets). Other liquid - solid (nanowire) interface will form when the liquid phase becomes supersaturated due to thermal or compositional fluctuations, resulting in the growth of silicon nanowires.[25] Even though above two examples are not directly related to our study, but these studies show that the silicon precipitation is possible from metal silicide.

The previous results and related inferences are summarized in the below table.

<p>Result and inference</p>	<ul style="list-style-type: none"> <li>• The Mg<sub>2</sub>Si is formed as intermediate phase at the initial stage of reduction process. (Figure 4.2.1)</li> <li>• The SiO<sub>2</sub>@Mg<sub>2</sub>Si@Si multi-layered structure might be generated. (Figure 4.1.1 and 4.1.5)</li> <li>• Large grain sized silicon is obtained. (Figure 4.1.3 and 4.2.7)</li> </ul> <hr/> <p>➔ Precipitation of silicon is main process for formation of silicon nanostructure instead of general concept of magnesiothermic reduction.</p>
<p>Result and inference</p>	<ul style="list-style-type: none"> <li>• When mixture power was reduced as pellet, the burst power was collected as product. And the sintered body, consisted of nanoparticle, was obtained when calcination was applied. (Figure 4.2.9)</li> <li>• In case of pellet sample, the reduction process is completed at around 450 °C. (Figure 4.2.8)</li> </ul> <hr/> <p>➔ The burst phenomenon is necessary for formation of inverse opal</p>

	<p>liked silicon nanostructure.</p> <p>➔ The gas in the pellet accelerates the precipitation or generation of silicon.</p>
--	--

From above consideration, the formation mechanism of inverse opal liked silicon structure is schematically suggested in Fig.4.2.11. And the detailed explanation is followed:

- 1) At the first step, the  $\text{SiO}_2$  converted to  $\text{Mg}_2\text{Si}$  by followed reaction;  $\text{SiO}_2 + 4\text{Mg} = 2\text{MgO} + \text{Mg}_2\text{Si}$ . Unreacted  $\text{SiO}_2$  and generated  $\text{MgO}$  are also located in the inside of  $\text{SiO}_2$  nanoparticle.
- 2) At the next step, the formed  $\text{Mg}_2\text{Si}$  is reacted with unreacted  $\text{SiO}_2$  and  $\text{SiO}_2$  is reduced to  $\text{Si}$  with follow reaction;  $\text{Mg}_2\text{Si} + \text{SiO}_2 = 2\text{MgO} + 2\text{Si}$ . While reducing to  $\text{Si}$ , the excess  $\text{Mg}$  is simultaneously reacted with reduced  $\text{Si}$  and  $\text{Mg}_2\text{Si}$  is repeatedly formed by followed reaction at the outside of reduced  $\text{Si}$  nanoparticle;  $\text{Si} + 2\text{Mg} = \text{Mg}_2\text{Si}$ .
- 3)  $\text{Mg}$  element of newly formed  $\text{Mg}_2\text{Si}$  as shell layer is diffused into inside of nanoparticle. At this time,  $\text{Mg}$  concentration of  $\text{Mg}_2\text{Si}$  is dramatically decreased and the  $\text{Si}$  is simultaneously precipitated to maintain the composition balance of  $\text{Mg}_2\text{Si}$ .

4) As the result, the single crystalline liked silicon hollow structure, with large grain size, is generated and this each structures are interconnected and inverse opal liked structure is formed.(Mg<sub>2</sub>Si, MgO and unreacted SiO<sub>2</sub> is leached out during acid treatment)

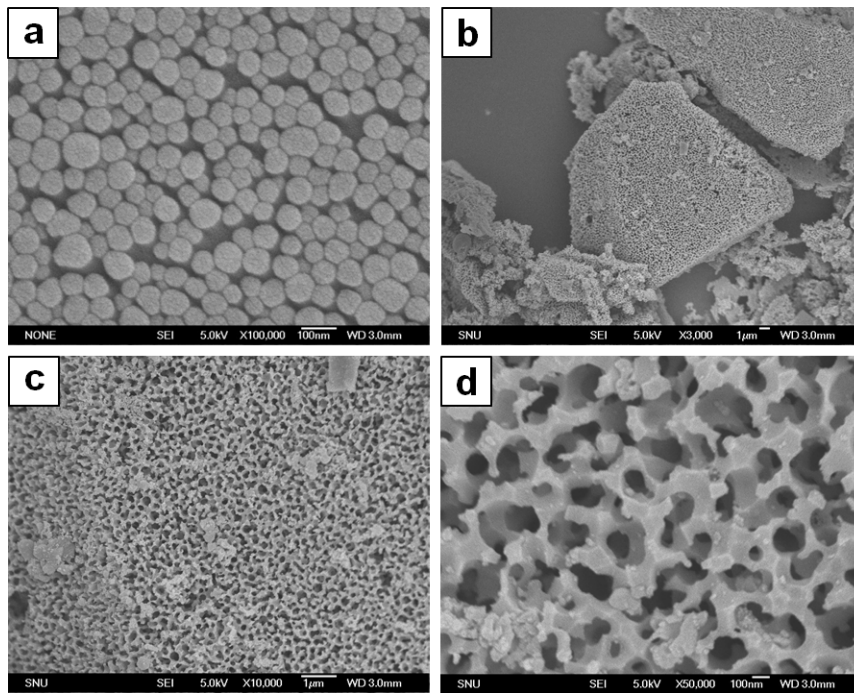


**Figure 4.2.6.** SEM image of (a) SiO<sub>2</sub> nanopowder, (b)-(d) inverse opal liked silicon nanostructure.

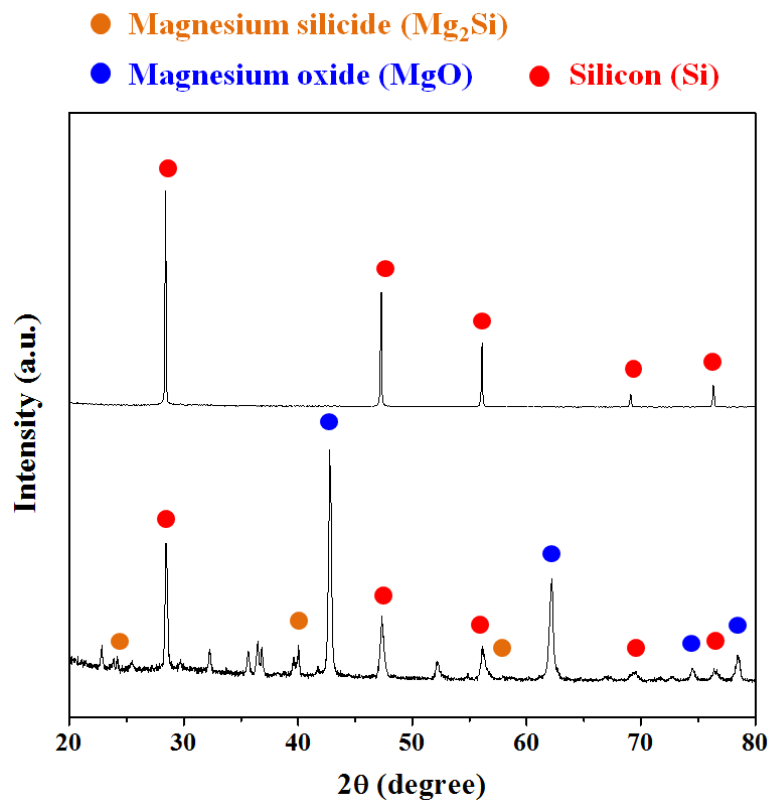


**Figure 4.2.7.** XRD pattern of (a) as reduced SiO<sub>2</sub>, at 700 °C for 1hr, and (d) HCl treated sample.

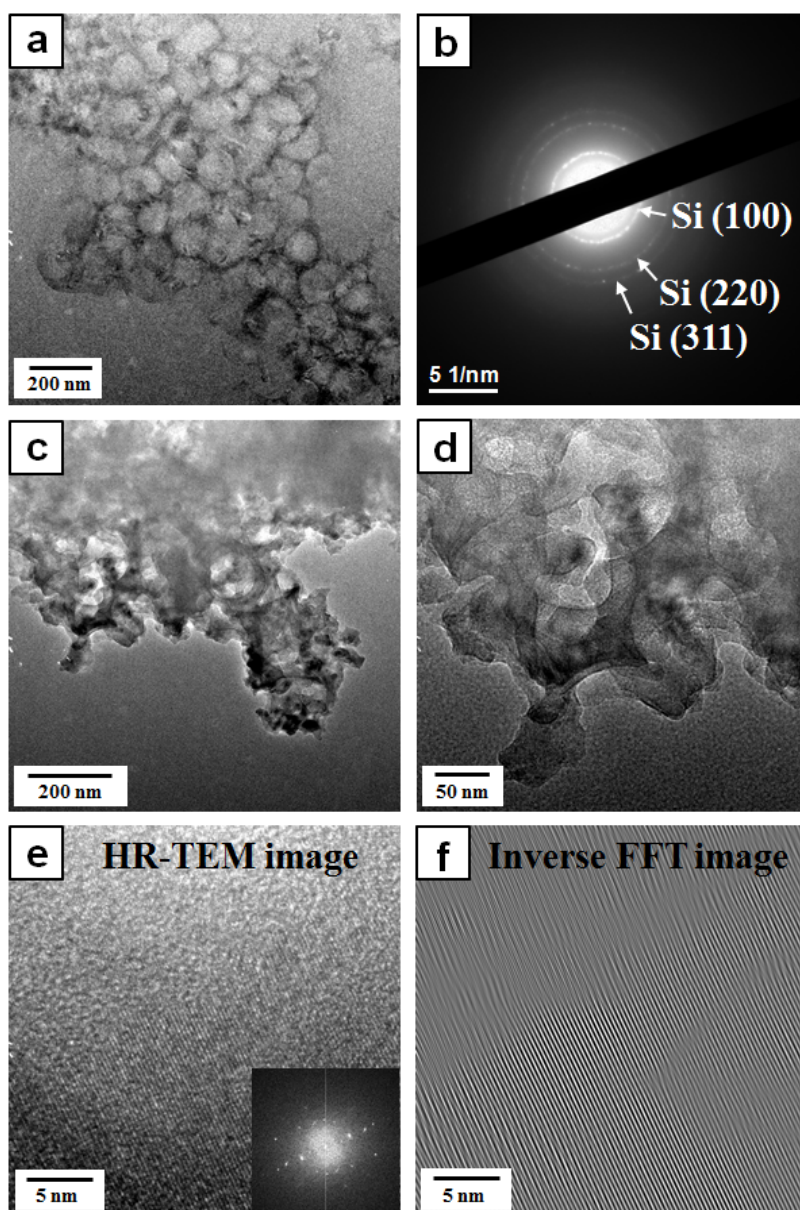


**Figure 4.2.8.** (a),(c),(d) TEM image of invers opal liked silicon structure and (b) SAED. (e) HR-TEM image of silicon and (f) inverse FFT image of (e).

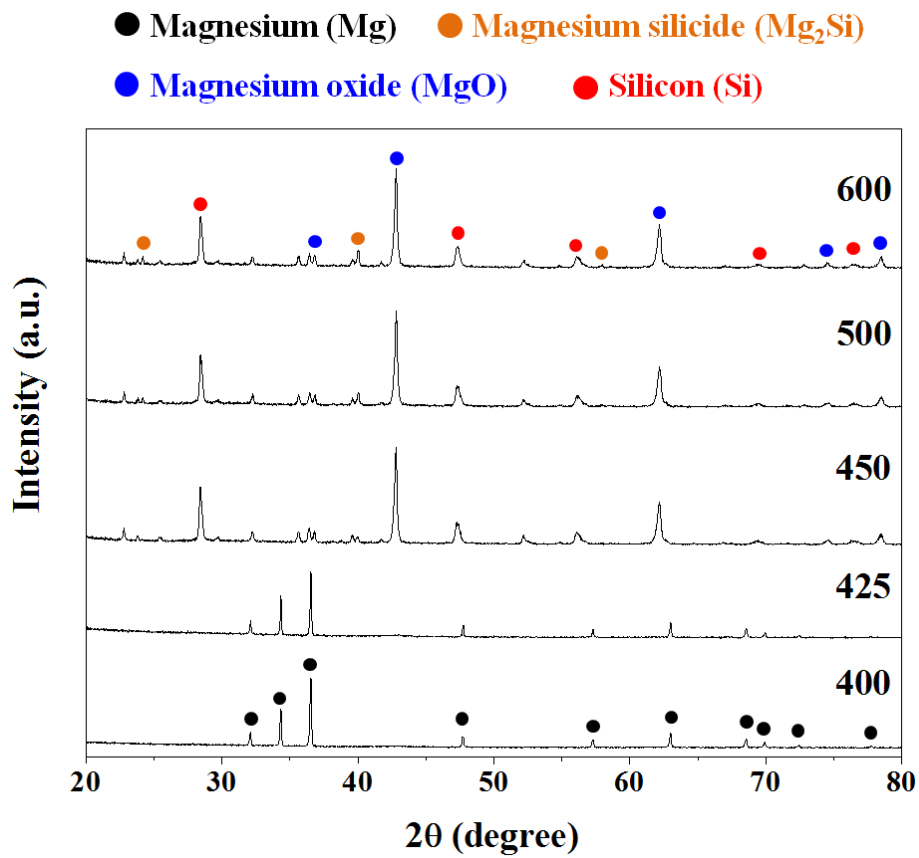


**Figure 4.2.9.** XRD pattern of different reduction temperature (without holding time).

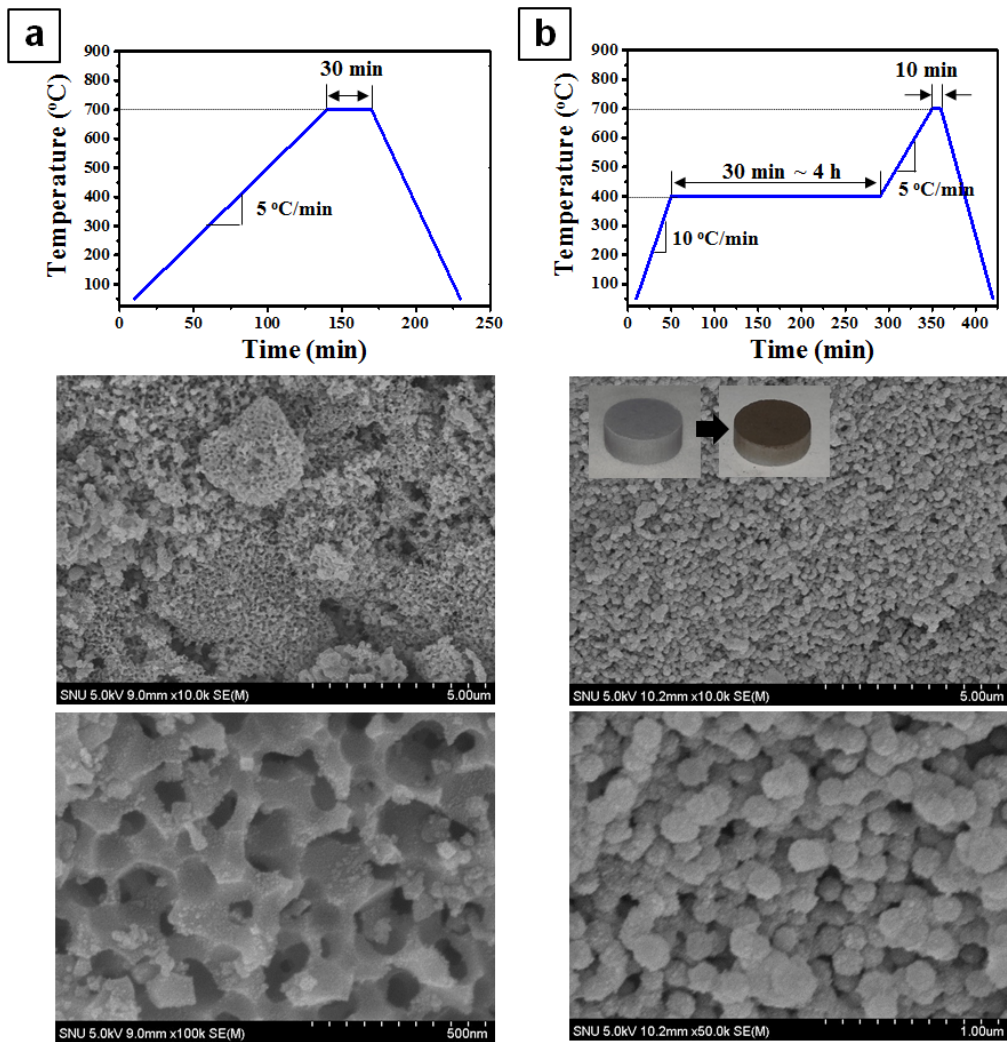
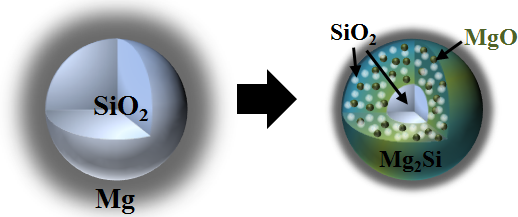
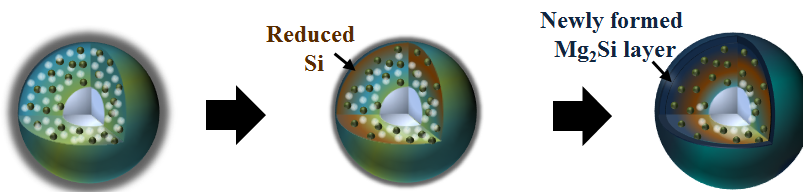


**Figure 4.2.10.** Different shape of silicon nanostructure with different processing schedule, (a) inverse opal liked silicon and (b) silicon nanoparticle.

**Step #1. Formation of  $Mg_2Si$**



**Step #2. Generation of  $Mg_2Si$  shell layer on the reduce Si surface**



**Step #3. Release of Si source from  $Mg_2Si$  shell layer**

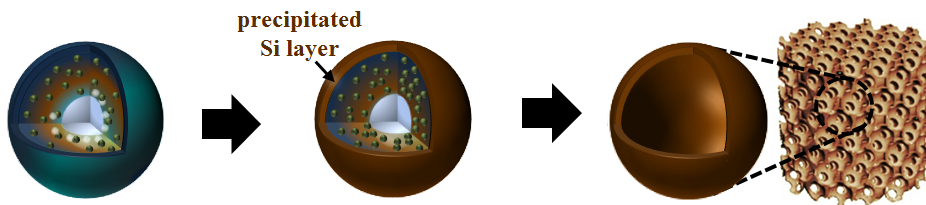


**Figure 4.2.11.** Schematic illustration of formation mechanism (inverse opal liked silicon).

### 4.3. Conclusion

In this chapter, the synthesis of silicon nanostructure is demonstrated. At the first, silicon nanosheet was synthesized by the magnesiothermic reduction with natural sand as source and template. The synthesized silicon nanosheet was well crystallized and showed better electrochemical properties than commercial silicon nanopowder for anode of lithium rechargeable battery and further enhancement was achieved by graphene encapsulation. The formation sequence of silicon nanosheet was suggested by XRD and TEM analysis during reduction and acid process. However, the suggested formation sequence is rather different from the general concept of magnesiothermic reduction. To investigate the details of reduction process, spherical  $\text{SiO}_2$  was used as starting material spherical  $\text{SiO}_2$ . The reduction process was conducted from 425 to 700 °C, it was revealed that the  $\text{Mg}_2\text{Si}$  was formed as intermediate at the initial stage of reduction process. In the silicon nanosphere,  $\text{Mg}_2\text{Si}$  was formed inside of  $\text{SiO}_2$  sphere, and reduced silicon sphere is composed of a few nano-sized silicon grains. Furthermore, inverse opal liked silicon nanostructure was formed when reduction was conducted as pellet, of Mg and  $\text{SiO}_2$ . In contrast of nanosphere, the silicon phase was obtained from 450 °C and further phase change was not observed. The abridged formation mechanism of inverse opal liked silicon structure is suggested.

#### 4.4. Reference

- (1) J. R. Dahn, T. Zheng, Y. Liu, J. S. Xue, *Science* **270** (1995) 590.
- (2) M. Winter, J. O. Besenhard, M. E. Spahr, P. Novak, *Adv. Mater.* **10** (1998) 725.
- (3) X. Y. Song, K. Kinoshita, *J. Electrochem. Soc.* **145** (1996) L120.
- (4) M. N. Obrovac, L. Christensen, *Electrochem. Solid State Lett.*, 2004, 7, A93.
- (5) J. Li, J. R. Dahn, *J. Electrochem. Soc.* **154** (2007) A156.
- (6) C. M. Park, K. H. Kim, H. Kim, H.-J. Sohn, *Chem. Soc. Rev.* **39** (2010) 3115.
- (7) G. Jung, Y. U. Kim, H. Kim, Y. J. Kim, H.-J. Sohn, *Energy Environ. Sci.* **4** (2011) 1986.
- (8) J. D. Holmes, K. P. Johnston, R. C. Doty, B. A. Korgel, *Science*, 2005, 287, 1471-1473.
- (9) K. Peng, Y. Yan, S. Gao, J. Zhu, *Adv. Mater.* 2002, 14, 1164.
- (10) A. M. Morales, C. M. Lieber, *Science*, 1998, 279, 208-211.
- (11) H. Kim, B. Han, J. Choo, J. Cho, *Angew. Chem.* 2008, 120, 10305–10308.
- (12) Y. Cai, S. M. Allan, K. H. Sandhage, F. M. Zalar, *J. Am. Ceram. Soc.*, (2005), 88, 2005–2010.
- (13) Zhihao Bao et al, *Nature*, 2007, 446, 172-175.
- (14) Y. Yu, L. Gu, C. Zhu, S. Tsukimoto, P. A. V. Aken, J. Maier, *Adv. Mater.* 2010, 22, 2247–2250

- (15) D. Chen, X. Mei, G. Ji, M. Lu, J. Xie, J. Lu, J. Y. Lee, *Angew. Chem.* 2012, 124, 1-6
- (16) J.-K. Yoo , J. Kim , Y. S. Jung, K. Kang, *Adv. Mater.* **2012.24**, 5452.
- (17) M. Saito, T. Yamada, C. Yodoya, A. Kamei, M. Hirota, T. Takenaka, A. Tasaka, M. Inaba, *Solid State Ionics*, (2012), 225, 506.
- (18) H. Okamoto, Y. Sugiyama, H. Nakano, *Chem. Eur. J.* 2011, 17, 9864 – 9887.
- (19) Z. Lu, J. Zhu, D. Sim, W. Zhou, W. Shi, H. H. Hng, Q. Yan, *Chem. Mater.*, 2011, 23 (24), 5293–5295.
- (20) W. S. Hummers, R. E. Offeman, *J. Am. Chem. Soc.* **1958**, 80, 1339
- (21) S. Yang, X. Feng, S. Ivanovici, K. Müllen, *Angew. Chem. Int. Ed.* 2010, 49, 8408 –8411.
- (22) M. Barati , S. Sarder, A. McLean, R. Roy, *Journal of Non-Crystalline Solids*, 2011. 357. 18-23.
- (23) L. Zhen, W. D. Fei, S. B. Kang, H. W. Kim, *Journal of Materials Science*, 1997 (32), 1895-1902.
- (24) D. G. Eskin, V. Massardier, P. Merle, *Journal of Materials Science*, 1999 (34), 811– 820.
- (25) D.P. Yu, Y.J. Xing, Q.L. Hang, H.F. Yan, J. Xu, Z.H. Xi, S.Q. Feng, *Physica E* 2001 (9), 305-309.

## 국문 초록

본 연구에서는 1) 산화주석 나노 중공체 및 복합체의 합성 및 전기화학 특성 평가, 2) 일차원 산화주석 나노 구조물의 합성 및 성장 제어, 3) 마그네슘 환원법을 이용한 실리콘 나노 구조체의 합성에 대한 연구를 수행하였다

첫 번째 장에서는 크기가 제어된 산화주석 중공구체의 합성과 이를 기반으로 형성된 나노복합체의 형성 및 이에 따른 전기 화학 특성평가를 수행하였다. 지난 20여 년간 리튬이차전지는 소형 휴대형 전자기기의 전원으로 사용되어 왔으나, 현재는 전력, 전기 자동차와 같은 고성능 이차전지에 대한 수요가 급증하고 있다. 따라서 현재의 상용 리튬 이차 전지에 비해 더 높은 에너지 밀도와 출력 밀도를 갖는 전지의 개발을 위해 음극, 양극, 분리막 및 전해질과 같은 주로 소재에 대한 신재료의 개발이 요구되고 있다. 이 중 음극재의 경우, 현재 탄소계 재료가 가장 널리 사용되고 있으나, 탄소의 낮은 이론용량 ( $372 \text{ mAh g}^{-1}$ )의 한계로 인해 이를 대체할 고용량 음극소재에 대한 연구가 활발히 진행되고 있다. 다양한 대체 소재 중 산화 주석은 탄소계

소재의 두 배 이상의 이론용량 ( $782 \text{ mAh g}^{-1}$ )을 가지고 있으나, 충방전 시 나타나는 부피변화 및 리튬산화물의 형성에 의한 용량의 손실 등의 문제가 여전히 남아 있다. 본 연구에서는 우선적으로 산화 주석 나노 중공체를 형성함으로써 부피 변화에 따른 손실을 최소화 하여 우수한 순환성을 구현하였으며, 중공구체의 크기의 감소에 따라 가역용량이 증가하는 것을 확인하였다. 특히 25 나노의 크기를 갖는 산화주석 중공구체의 경우 50회의 충방전 평가 후에도 이론 용량에 근접한 가역용량 ( $750 \text{ mAh g}^{-1}$ )을 나타내는 것을 확인하였다. 또한 코발트 산화물층을 산화주석 중공구체 위에 형성시킴으로써, 우수한 순환성뿐만 아니라 초기 효율의 향상 및 가역용량이 비약적으로 증가하는 것을 확인하였으며 투과전자현미경 분석을 통해 성능향상의 메커니즘을 제시하였다.

두 번째 장에서는 일차원 나노 구조의 산화주석의 합성 및 성장 제어에 대한 연구 결과를 수록하였다. 금속산화물 기반의 반도체식 가스센서는 넓은 비표면적으로 인한 고기능성 및 낮은 소비 전력 등의 장점으로 인하여 가스감지를 위한 화학센서로서 많은 연구가 진행되고 있다. 특히 산화 주석의 경우, 이차전지뿐만 아니라 가스 센서에

있어서도 훌륭한 감지능력을 나타내며, 특히 나노 튜브와 나노선과 같은 일차원의 나노구조를 형성하는 경우 가스감지 능력이 향상될 수 있다. 본 연구에서는 전기 방사된 고분자나노섬유 위에 원자층 증착법을 통해 산화주석을 코팅함으로써 산화주석 나노 튜브를 합성하는 방법을 제시하고, 합성된 나노 튜브의 가스감지 능력을 평가하였다. 나노튜브의 두께는 원자층 증착 방법을 통해 정밀히 제어되었으며, 수 나노의 산화주석 입자로 나노 튜브가 구성되어 있음을 투과전자현미경을 통해 확인하였다. 합성된 산화주석 나노튜브 네트워크는 수소, 일산화탄소, 암모니아 질소 산화물 가스에 대해 반응하였으며, 특히 에탄올 가스에 대해 5초내외의 반응속도로 우수한 반응도를 나타내었다. 일차원 나노구조체 연구 분야에 있어서는 다결정체의 나노튜브 뿐만 아니라 단결정으로 구성된 나노선의 합성 및 성장 제어 연구도 병행되어 수행되었다. 나노선의 성장 제어 및 배열은 나노선 기반 소자의 신뢰성에 가장 중요한 요소이나 현재까지 산화주석 나노선의 성장거동에 대한 명확한 연구는 부족하다. 본 연구에서는 금속 촉매를 사용하는 열증착 방법을 통해 나노선을 합성하였으며, 산화주석 나노선의 경우, r-cut 사파이어 기판 상에서 산화주석의

결정구조에 기인된 특정 성장 특성이 발현됨을 확인하였다. 특히 금속 나노 촉매의 거리를 변화함으로써 수직 및 수평 성장의 두 가지 성장 거동을 제어할 수 있음을 제시하고, 이때 나타나는 나노선과 기판과의 에피텍셜 관계를 규명하였다. 특히 수평 성장된 나노선의 경우, 기판과의 에피텍셜 관계를 따라 일방향으로 배향되는 것이 확인되었다. 또한 산화주석 나노선의 수평 성장 시에는 성장되는 금속 촉매 및 나노선 간의 물리적 간섭이 사라지게 되어, 나노 촉매의 크기 변화에 따른 나노선의 크기 제어가 정확히 이루어질 수 있었다.

실리콘계 음극물질은 큰 이론용량 ( $\text{Li}_{15}\text{Si}_4$  :  $3600 \text{ mAh g}^{-1}$ )과 낮은 작동 전압 (약  $0.1 \text{ V vs. Li/Li}^+$ )을 가지고 있어 탄소계 전극물질을 대체할 후보로써 많은 연구가 진행되고 있다. 하지만 충전과 방전 과정 시 수반되는 음극 물질의 큰 부피 변화가 전극의 파괴현상을 일으키고 이는 전기화학특성에 악영향을 미치게 된다. 이와 같은 문제를 나노구조의 실리콘을 형성함으로써 해결하고자 하는 연구가 현재까지도 활발히 진행되고 있다. 하지만 현재까지 제시되고 있는 실리콘 나노구조의 합성 방법은 주로 화학 기상 증착 (CVD) 방법을 통해 이루어지고 있으나, 이와 같은 공정은 독성있는 전구체를 사용하거나 높은 공정단가의

기술이기 때문에 사용의 문제점이 있다. 이를 극복하고자 마그네슘 환원 반응을 이용한 실리콘 나노구조의 합성 방법이 제시되어 현재 활발한 연구가 진행 중에 있다. 본 방법은 나노 구조의  $\text{SiO}_2$ 로부터 구조를 유지한 채 실리콘으로 환원할 수 있으며, 기존의 환원 공정에 비해 낮은 공정온도 (약 650도) 및 짧은 공정 시간을 필요하기 때문에 다른 기술에 비해 상용화의 가능성이 높다. 본 연구에서는 마그네슘 환원 방법을 이용한 박막 형태의 이차원 실리콘 나노구조의 합성 및 전기화학특성 평가를 수행하였다. 특히, 실리콘의 원재료인 모래를 합성의 전구체 및 모형틀로 사용하여 연구가 진행되었다. 현재까지 알려진 반응 기구에 따른 환원된 실리콘 나노구조의 입자의 경우 수 나노의 크기를 갖는 것에 반해, 본 연구에서 합성된 실리콘 나노구조체는 수십 나노크기의 입자로 구성되어 있다. 합성된 실리콘 나노구조체의 경우 상용 실리콘 나노 분말에 비해 향상된 전기화학 특성을 나타내었으며, 전기화학특성의 향상을 위해 그래핀을 코팅한 결과 가역 용량의 향상 및 우수한 순환성이 확인되었다. 보다 정확한 환원 기구를 살펴보기 위하여,  $\text{SiO}_2$  나노 분말을 사용하여 환원 반응 기구에 대한 연구를 진행하였다. 이를 통해, 환원과정의 초기 단계에서  $\text{Mg}_2\text{Si}$  상이 중간상으로 형성되고, 실질

적인 환원 공정은 마그네슘으로부터 이루어지는 것이 아니라,  $Mg_2Si$ 로부터 이루어지는 것이 확인되었다. 또한 혼합 분말의 형태가 아닌 분말 성형체 (pellet)를 형성하여 열처리를 한 결과, 역오팔 (inverse opal) 구조의 실리콘 나노구조체가 합성됨을 확인하였다.

주요어 : 나노 구조, 중공구조, 이중구조, 졸-겔법, 코팅, 나노 튜브,  
원자층 증착법, 나노선, 열증착, 마그네슘환원법, 리튬이차전지,  
음극, 산화주석, 코발트 산화물, 실리콘

학 번 : 2006-20831

## Research Activities

---

### Thesis

1. Won-Sik Kim, Fabrication and Characterization of Tin Oxide and Silicon Based Nanostructures for Gas Sensor and Li-ion Battery, Ph.D. Thesis, Seoul National University, (2013).

### International Article (SCI Journal)

1. Won-Taek Moon, Youn-Ki Jun, Hyun-Su Kim, Won-Sik Kim and Seong-Hyeon Hong, "CO gas sensing properties in Pd-added ZnO Sensor" J. Electroceram 10.1007 / s10832-007-9377-y.
2. Won-Sik Kim, Youn-Ki Jun, Kee Hoon Kim, Seong-Hyeon Hong, " Enhanced magnetization in Co and Ta-substituted BiFeO<sub>3</sub> ceramics" Journal of Magnetism and Magnetic Materials 321 (2009) 3262-3265.
3. B. Venkata Manoj Kumara, Won-Sik Kim, Seong-Hyeon Hong, Hung-Tak Bae, Dae-Soon Lim, " Effect of grain size on wear behavior in Y-TZP ceramics" Materials Science and Engineering A 527 (2010) 474-479.
4. Myung Yang, Dai-Hong Kim, Won-Sik Kim, Tae June kang, Byung Yang Lee,

Seunghun Hong, Yong Hyup Kim, Seunghun Hong, "H<sub>2</sub> sensing characteristics of SnO<sub>2</sub> coated single wall carbon nanotube network sensors" *Nanotechnology* 21 (2010) 215501.

5. Won-Sik kim, Hong-chan Kim, Seong-hyeon Hong, "Gas sensing properties of MoO<sub>3</sub> nanoparticles synthesized by solvothermal method" *Journal of Nanoparticle Research* 12 (2010)1289-1896.
6. Won-Sik Kim, byoung-Sun Lee, Dai-Hong Kim, Hong-Chan Kim, Woong-Ryeol Yu, Seong-Hyeon Hong, "SnO<sub>2</sub> nanotubes fabricated using electrospinning and atomic layer deposition and their gas sensing performance" *Nanotechnology* 21 (2010) 245605.
7. Dai Hong Kim, Won-Sik Kim, Sung Bo Lee, Seong-Hyeon Hong , "Gas sensing properties in epitaxial SnO<sub>2</sub> films grown on TiO<sub>2</sub> single crystals with various orientations" *Sensors and actuators B* 147 (2010) 653-659.
8. Won-Sik Kim, Daihong Kim, Kyoung Jin Choi, Jae-Gwan Park, and Seong-Hyeon Hong, "Epitaxial Directional Growth of Tin Oxide (101) Nanowires on Titania (101) Substrate", *Crystal Growth & Design* 10 (11) (2010) 4746-4751.
9. Yun-Guk Jang, Won-Sik Kim, Dai-Hong Kim, and Seong-Hyeon Hong, "Fabrication of Ga<sub>2</sub>O<sub>3</sub>/SnO<sub>2</sub> core-shell nanowires and their ethanol gas sensing properties", *Journal of Materials Research* 26 (17) (2011) 2322-2327.

10. Byoung-Sun Lee, Won-Sik Kim, Dai-Hong Kim, Hong-Chan Kim, Seong-Hyeon Hong and Woong-Ryeol Yu, "Fabrication of SnO<sub>2</sub> nanotube microyarn and its gas sensing behavior", Smart Mater. Struct. 20 (2011) 105019.
11. Won-Sik Kim, Dai-Hong Kim, Yun-Guk Jang and Seong-Hyeon Hong, "Synthesis of well-aligned SnO<sub>2</sub> nanowires with branches on r-cut sapphire substrate", CrystEngComm 14 (2012) 1545-1549.
12. Yoon Hwa, Won-Sik Kim, Seong-Hyeon Hong, Hun-Joon Son "High capacity and rate capacity of core-shell structured nano-Si/C anode for Li-ion batteries", Electrochimica Acta, 71 (2012) 201-205.
13. Won-Sik Kim, Yun-Guk Jang, Dai-Hong Kim, Hong-Chan Kim and Seong-Hyeon Hong, "Hetero-epitaxial growth of vertically-aligned TiO<sub>2</sub> nanorods on an m-cut sapphire substrate with an (001) SnO<sub>2</sub> buffer layer", CrystEngComm 14 (2012) 4963-4966.
14. Won-Sik Kim, Yoon Hwa, Hun-Soon Sohn and Seong-Hyun Hong, "Robust Synthesis of Nano-sized SnO<sub>2</sub> Hollow Spheres and Size Effect for lithium ion battery anode application", J. Power Sources, 235 (2012) 108-112.

## **International Conference Presentations**

1. "Fabrication and Characterization of Magnetoelectric Multiferroics BiFeO<sub>3</sub> with Metal Ion Substitution", 5th Asian Meeting on Electroceramics, Thailand (2006).
2. "Wear Properties in Nanocrystalline Y-TZP Ceramics", International conference on multifunctional materials and structures, Hong Kong (2008).
3. "Synthesis and characterization of SnO<sub>2</sub> nanowires by thermal evaporation", MRS spring meeting, USA (2009)
4. "Fabrication of SnO<sub>2</sub> Nanotubes by Eletrospinning and Atomic Layer Deposition and Their Gas Sensing Performance Toward Ethanol", MRS spring meeting, USA (2010)
5. "Lateral Growth of SnO<sub>2</sub> Nanowires on R-cut Sapphire Substrate", ICMAT 2011, Singapore (2011)
6. " Synthesis of Co<sub>3</sub>O<sub>4</sub>-SnO<sub>2</sub> Multi-Layered Hollow Sphere and Their High Reversible Capacity for Anode of Li-Ion Battery", The 222<sup>nd</sup> Electrochemical Society Meeting, USA (2012).